



Ricardo Jorge Neves Eleutério

Licenciatura em Ciências de Engenharia Biomédica

Microwave Imaging of the Axilla to Aid Breast Cancer Diagnosis

Dissertação para obtenção do Grau de Mestre em
Engenharia Biomédica

Orientadora : Raquel Cruz da Conceição, Doutora,
Instituto de Biofísica e Engenharia Biomédica,
Faculdade de Ciências da Universidade de Lisboa

Júri:

Presidente: Prof. Doutora Carla Quintão Pereira

Arguente: Prof. Doutor Pedro Manuel Vieira

Vogal: Doutora Raquel Cruz da Conceição



FACULDADE DE
CIÊNCIAS E TECNOLOGIA
UNIVERSIDADE NOVA DE LISBOA

Agosto, 2014

Microwave Imaging of the Axilla to Aid Breast Cancer Diagnosis

Copyright © Ricardo Jorge Neves Eleutério, Faculdade de Ciências e Tecnologia, Universidade Nova de Lisboa

A Faculdade de Ciências e Tecnologia e a Universidade Nova de Lisboa têm o direito, perpétuo e sem limites geográficos, de arquivar e publicar esta dissertação através de exemplares impressos reproduzidos em papel ou de forma digital, ou por qualquer outro meio conhecido ou que venha a ser inventado, e de a divulgar através de repositórios científicos e de admitir a sua cópia e distribuição com objectivos educacionais ou de investigação, não comerciais, desde que seja dado crédito ao autor e editor.

Acknowledgements

First and foremost, I would like to thank God for His many blessings, wisdom and perseverance during this research project.

I would also like to express my sincere gratitude to my supervisor, Dr. Raquel Conceição, for introducing me to the topic, for her guidance, useful comments, remarks, unconditional support and encouragement throughout the learning process of this dissertation. I cannot imagine having a better mentor and advisor. I am also thankful to Alexandre Medina for being part of this project.

I would like to thank all the professors at FCT-UNL, particularly Prof. Dr. Mário Forjaz Secca, for his wise advice and his dedication to Biomedical Engineering. I would also like to show my appreciation for Prof. Dr. Pedro Almeida, for the opportunity to work at the Instituto de Biofísica e Engenharia Biomédica, IBEB (Institute of Biophysics and Biomedical Engineering).

I wish to thank my colleagues and friends who have accompanied me during these last 5 years, mainly Ana Carolina Pádua, Vanessa Cunha, Guilherme Coutinho and Filipa Ferreira, for all the moments we have had together. A special thanks to Pedro Ferreira for his support, humour, friendship, for the sleepless nights we spent together writing our dissertations, and for his valuable suggestions throughout this work. I would also like to thank to all my friends in my hometown, particularly Marisa Moisés, Andreia Siquenique, Alberto Ferreira and Beatriz Ferro, who have always been there for me.

Finally, I am immeasurably indebted to my family, in particular my parents. Their example and advice have proven to be invaluable. I am also grateful to my brother and my sister-in-law, for being a source of inspiration, and my nephew and my niece for their ability to make me smile, which helped me overcome each hurdle I have encountered.

This dissertation has been developed in the framework of the COST Action TD1301, MiMed.

Abstract

Breast cancer is the most common type of cancer among women all over the world. An important issue that is not commonly addressed in breast cancer imaging literature is the importance of imaging the underarm region — where up to 80% of breast cancer cells can metastasise to. The first axillary lymph nodes to receive drainage from the primary tumour in the breast are called Sentinel Node. If cancer cells are found in the Sentinel Node, there is an increased risk of metastatic breast cancer which makes this evaluation crucial to decide what follow-up exams and therapy to follow. However, non-invasive detection of cancer cells in the lymph nodes is often inconclusive, leading to the surgical removal of too many nodes which causes adverse side-effects for patients.

Microwave Imaging is one of the most promising non-invasive imaging modalities for breast cancer early screening and monitoring. This novel study tests the feasibility of imaging the axilla region by means of the simulation of an Ultra-Wideband Microwave Imaging system. Simulations of such system are completed in several 2D underarm models that mimic the axilla. Initial imaging results are obtained by means of processing the simulated backscattered signals by eliminating artefacts caused by the skin and beam-forming the processed signals in order to time-align all the signals recorded at each antenna. In this dissertation several image formation algorithms are implemented and compared by visual inspection of the resulting images and through a range of performance metrics, such as Signal-to-Clutter Ratio and Full Width Half Maximum calculations.

The results in this study showed that Microwave Imaging is a promising technique that might allow to identify the presence and location of metastasised cancer cells in axillary lymph nodes, enabling the non-invasive evaluation of breast cancer staging.

Keywords: Microwave Imaging; Breast Cancer Detection; Axilla Imaging; Ultra-Wideband; Lymph Nodes; Sentinel Node

Resumo

O cancro da mama é o tipo de cancro mais comum em todo o mundo entre as mulheres. Um assunto que não é muito abordado na literatura é a importância da imagiologia da região da axila — onde até cerca de 80% das células cancerígenas da mama podem metastisar-se. Os primeiros gânglios linfáticos da axila a receber drenagem do tumor primário da mama chamam-se Gânglios Sentinela. Se forem encontradas células cancerígenas no Gânglio Sentinela, existe um risco maior de metastisação, o que torna esta avaliação num passo importante para decidir que exames e tratamentos seguir. No entanto, frequentemente, a detecção de células cancerígenas nos gânglios linfáticos de forma não-invasiva não é conclusiva, sendo necessária a remoção de demasiados gânglios, o que causa efeitos secundários adversos para os pacientes.

Imagiologia por Micro-ondas é uma técnica promissora para detecção e monitorização precoce do cancro da mama de forma não-invasiva. Este estudo pioneiro testa a viabilidade da imagiologia da região axilar através de simulação de um sistema de imagem por microondas baseado num pulso de sinal com banda ultra-larga. As simulações do sistema são feitas em vários modelos 2D que imitam a axila. As imagens são obtidas através do processamento dos sinais reflectidos obtidos em simulação, eliminando artefactos causados pela pele e, depois, alinhando os vários sinais gravados em cada antena no tempo. Nesta dissertação, vários algoritmos de formação de imagem são implementados e comparados através de uma análise visual das imagens obtidas e através de algumas métricas tais como o Rácio Sinal-Ruído e a Largura a Meia Altura.

Os resultados deste estudo mostraram que Imagiologia por Micro-ondas é uma técnica promissora que poderá permitir identificar a presença e localização de metástases nos gânglios linfáticos da axila, permitindo a avaliação do estadió do cancro da mama de forma não-invasiva.

Palavras-chave: Imagiologia por Micro-ondas; Detecção de Cancro da Mama; Imagiologia da Axila; Sinal com Banda Ultra-Larga; Gânglios Linfáticos; Gânglio Sentinela

Contents

Acronyms	xix
1 Introduction	1
1.1 Motivation and Background	1
1.1.1 Breast Imaging	3
1.1.1.1 Conventional Techniques	3
1.1.1.2 Microwave Imaging	4
1.1.2 Axilla Imaging	6
1.2 Objectives	8
1.3 Dissertation Overview	8
2 Background	11
2.1 Anatomical and Physiological Background	11
2.1.1 Lymphatic System of the Underarm	11
2.1.2 Tumour Formation and Cancer Staging	13
2.1.3 Breast Cancer Metastasises	14
2.2 Axilla modelling	15
2.2.1 Dielectric Properties	15
2.2.1.1 Dielectric Properties of Lymph nodes	16
2.2.2 Finite-Difference Time-Domain Method	18
2.3 Ultra-Wideband Radar Microwave Imaging	19
2.3.1 Artefact Removal Algorithms	20
2.3.1.1 Average Subtraction	20
2.3.1.2 Rotation Subtraction	20
2.3.1.3 Adaptive Filtering	20
2.3.1.4 Entropy Based Time Window	21
2.3.1.5 Frequency Domain Pole Splitting	21
2.3.1.6 Hybrid Artefact Removal Algorithm	22
2.3.2 Beamforming Algorithms	22

2.3.2.1	Data-Independent Beamforming	22
	Delay-And-Sum	22
	Improved Delay-And-Sum	23
	Delay-Multiply-And-Sum	24
	Channel-Ranked Delay-And-Sum	24
	Microwave Imaging via Space-Time	24
	Time-Difference-of-Arrival	25
2.3.2.2	Data-Adaptive Beamforming	25
2.3.3	Discussion and Conclusion	26
3	Methods and Materials	29
3.1	Materials	29
3.2	Methods	31
3.2.1	FDTD Simulation Procedure	31
3.2.2	Artefact Removal Algorithms	32
3.2.3	Beamforming Algorithms	33
3.2.4	Performance Metrics	34
4	Results and Discussion	37
4.1	Computational Electromagnetic Simulation for Data Acquisition	37
4.2	Simple Heterogeneous FDTD Models	39
4.2.1	Effects of Natural Variations in Dielectric Properties	40
4.2.2	Effects of Increasing Tumour Depth	41
4.2.3	Effects of Increasing Tumour Size	44
4.3	Heterogeneous FDTD Model	45
4.3.1	Resolution of the System	46
4.4	Heterogeneous FDTD Model With Muscle	47
4.5	Other Heterogeneous FDTD Models	49
5	Conclusion	51
5.1	Main Conclusions	51
5.2	Limitations and Future Work	52
5.3	Contributions	54
A	LN VISUALISER's Quick Guide	69
B	Poster	79
C	Abstract	81

List of Figures

1.1	Statistical information on breast cancer in women. (a) Estimated incidence and mortality for women in Portugal in 2012; age-standardised rate (Europe) [3]. (b) Time-trend of mortality from breast cancer for women in some developed countries; age-standardised rate (World) [4].	2
1.2	Estimated age-standardised incidence rate from breast cancer per 100,000 women around the world in 2012 [1].	3
1.3	Sentinel lymph node biopsy [62].	6
2.1	Axillary lymph nodes. (a) Illustration of the anatomical classification of the axillary lymph nodes [95]. (b) Illustration of the surgical classification (used in axillary dissection) of the axillary lymph nodes [71].	12
2.2	The variation of the relative permittivity and conductivity between 0.5 and 30 GHz of pure cancer tissues and metastasised lymph nodes in comparison to normal lymph nodes as reported by Choi <i>et al.</i> [84]. The solid line is the real part of the permittivity and the dotted line the imaginary part of the permittivity (ϵ), which is considered to be $\epsilon'' = \sigma/\omega$. Black represents the cancer mass, blue the metastasised node, and red the normal node. . .	16
2.3	The variation of the (a) relative permittivity and (b) conductivity between 1 and 20 GHz, measured in the external and cross-sectional surfaces of healthy lymph nodes for samples from 2 patients as reported by Cameron <i>et al.</i> [61]. The measurements in the external surface of the node correspond to 40% and 47% fat beneath the probe whereas the cross-sectional measurements show 20% and 10% fat content under the measurement site. . .	17
2.4	The variation of the (a) relative permittivity and (b) conductivity between 1 and 20 GHz, measured in the external and cross-sectional surfaces of lymph nodes containing tumour cells, as reported by Cameron <i>et al.</i> [61]. .	17
2.5	Generic diagram illustrating the proposed UWB radar Microwave Imaging system of the axilla.	19

3.1	Representation of a heterogeneous model with muscle.	30
3.2	Representation of the UWB input signal. (a) Time-domain of the pulse. (b) Magnitude spectra of the pulse.	32
3.3	Diagram of the monostatic DAS beamforming algorithm with $M = 4$ antennas. All other beamformers (DMAS, Channel-Ranked DAS and Channel-Ranked DMAS) are derived from this one.	34
4.1	Computed FDTD backscattered signals (note the different scales in the Signal Magnitude axes between plots). (a) Signals before and after applying the Adaptive Filtering artefact removal. (b) Late-time responses after applying the Adaptive Filtering artefact removal at 4 different channels. (c) Artefact-free signal at channel 9 before and after time-shifting.	38
4.2	Image formation using Adaptive Filtering and DMAS. (a) FDTD model of the underarm with a 20 mm metastasised lymph node at 2 cm from skin. (b) Resulting image of backscattered energy.	39
4.3	Effects of dielectric heterogeneity for lymph nodes at two different depths: 2.0 cm and 4.9 cm. The metrics (a) SCR and (b) SMR correspond to the use of the Adaptive Filtering artefact removal and the DMAS beamformer. . .	41
4.4	Images of backscattered energy using the Adaptive Filtering artefact removal and the DMAS beamformer for a tumour located at a depth of 4.9 cm, with (a) 0%, (b) $\pm 20\%$ and (c) $\pm 50\%$ of dielectric variation of the tissue surrounding the lymph node, respectively.	42
4.5	Image formation using the Adaptive Filtering artefact removal and the DMAS beamformer for a lymph node located at different depths. (a), (c), (e) FDTD models of the underarm with a lymph node at 2.0 cm, 4.9 cm and 8.2 cm, respectively. (b), (d), (f) Resulting images of backscattered energy.	43
4.6	Variation of (a) L_{error} and (b) SMR with tumour size for all beamformers using the Adaptive Filtering artefact removal.	44
4.7	Image formation using Adaptive Filtering and Channel-Ranked DMAS. (a) Numerical phantom with two lymph nodes (15 mm long) and (b) resulting image of backscattered energy. (c) Numerical phantom with one healthy lymph node (15 mm long) and a metastasised lymph node (22 mm long) and (d) resulting image of backscattered energy.	46
4.8	Image formation using Adaptive Filtering and Channel-Ranked DMAS for two adjacent lymph nodes in several levels, according to their position to the muscle. (a), (c), (e) FDTD models of the underarm with metastasised lymph nodes at level I, level II in the surface of the muscle and level II inside the muscle, respectively. (b), (d), (f) Resulting images of backscattered energy.	48

4.9	Image formation using Adaptive Filtering and Channel-Ranked DMAS for several heterogeneous FDTD models with two lymph nodes. (a), (c), (e) FDTD models of the underarm representing several phantoms. (b), (d), (f) Resulting images of backscattered energy.	50
5.1	Illustration of a possible antenna configuration to be used in an examination of the underarm to image axillary lymph nodes.	53

List of Tables

2.1	Breast cancer staging. Adapted from [97].	14
3.1	Parameters of the Debye Formulation for the various tissues in the under-arm that are represented in the FDTD models.	31
4.1	Performance metric results of the selected artefact removals ("Ideal", Average Subtraction and Adaptive Filtering) and beamformers (DAS, DMAS, Channel-Ranked DAS and Channel-Ranked DMAS) for a simple heterogeneous FDTD model of the axilla with one lymph node at location (-2.0, 5.0) cm.	40
4.2	Metric results for a metastasised lymph node located at different depths using the Adaptive Filtering artefact removal and the DMAS beamformer.	42
4.3	Performance metric results of the selected artefact removals and beamformers for heterogeneous FDTD models of the axilla with two lymph nodes (a healthy and a metastasised one). It compares two scenarios: one with lymph nodes of the same size, and another one with the metastasised lymph node larger than the healthy lymph node.	45
4.4	Relevant performance metric results of the selected artefact removals and beamformers for heterogeneous FDTD models of the axilla with muscle and two lymph nodes (a healthy and a metastasised one). It compares lymph nodes in two different levels: level I and level II.	47

Acronyms

MRI	Magnetic Resonance Imaging
PEM	Positron Emission Mammography
UWB	Ultra-WideBand
PET	Positron Emission Tomography
CT	Computed Tomography
FDTD	Finite-Difference Time-Domain
DAS	Delay-And-Sum
IDAS	Improved Delay-And-Sum
DMAS	Delay-Multiply-And-Sum
MIST	Microwave Imaging via Space-Time
TDOA	Time-Difference-Of-Arrival
RCB	Robust Capon Beamformer
MAMI	Multistatic Adaptive Microwave Imaging
FWHM	Full Width Half Maximum
SCR	Signal-to-Clutter Ratio
SMR	Signal-to-Mean Ratio
MMR	Max-to-Max Ratio
L_{error}	Localisation Error



Introduction

1.1 Motivation and Background

Breast cancer is the second most common cancer in the world with 1.67 million new diagnosed cases in 2012. It is, by far, the most frequent cancer among women accounting for 25% of all cancers and ranking as the second cause of cancer death in more developed countries after lung cancer [1]. In Portugal, in 2012, female breast cancer was not only the leading type of cancer (6,090 new cases, 29.4% of all cancers) but also the main cause of death from cancer in women (1,570 deaths) [2], as shown in Figure 1.1 (a). Note that cancer rates (both the number of new cases and the number of deaths per 100,000 persons per year) are usually age-standardised. Standardization adjusts rates to take into account how many old or young people are in the considered population. An age-standardised rate is, therefore, the rate that a population would have if it had a standard age structure. Standardization is important when comparing several populations with different age average, since age has a significant influence on the risk of cancer [1].

Worldwide, the incidence of breast cancer has increased annually [5]. Most breast cancer occurs because of a combination of risk factors [6, 7] such as:

- **Age.** Older women are more prone to develop breast cancer [8].
- **Lifestyle.** Alcohol [9], obesity and low amount of exercise [10] increase the chance of developing breast cancer. Moreover, diets rich in well-done meats [11] or fat [12] are associated with increased risk for breast cancer, while a high intake of fruit and vegetables decreases that risk [13].
- **Reproductive events.** Late first pregnancy and no pregnancy at all increase cancer

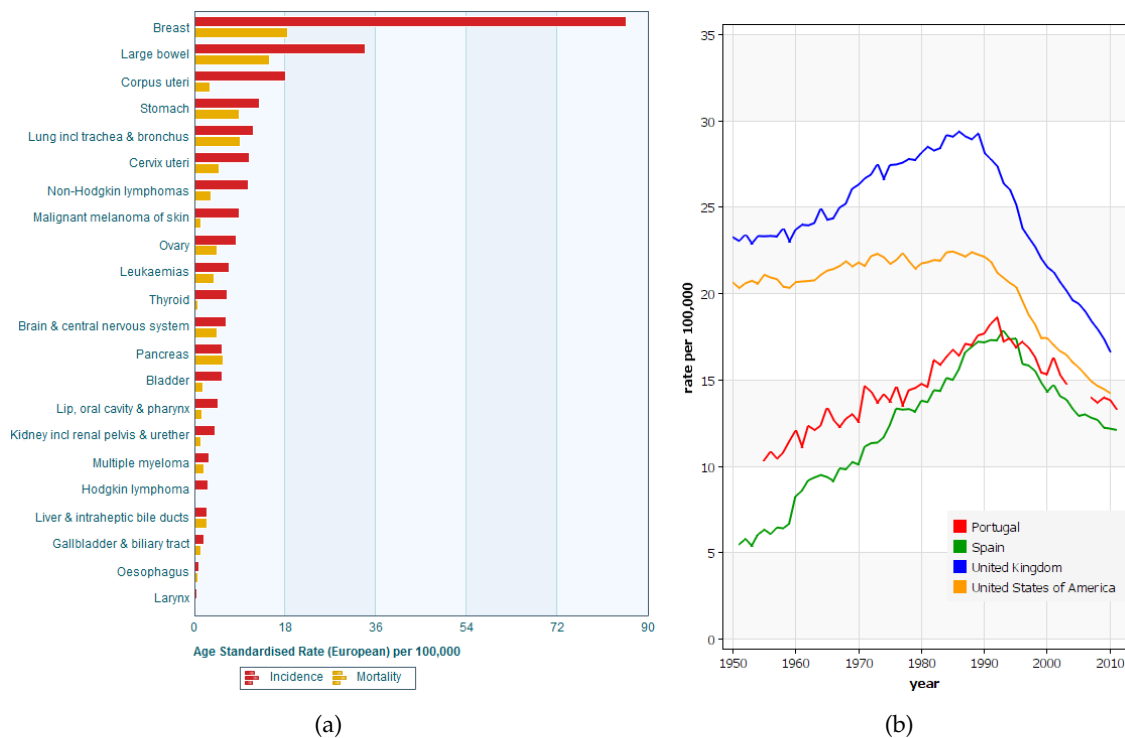


Figure 1.1: Statistical information on breast cancer in women. (a) Estimated incidence and mortality for women in Portugal in 2012; age-standardised rate (Europe) [3]. (b) Time-trend of mortality from breast cancer for women in some developed countries; age-standardised rate (World) [4].

rates whereas breast-feeding decreases this rates [7, 14].

- **Family history.** Family history of breast cancer increases a woman's risk of developing this disease [15].
- **Ionizing radiation.** Exposure of the mammary gland to high-dose of ionizing radiation has been demonstrated to increase the risk of breast carcinoma [16].
- **Geographic location and socioeconomic status.** There are more breast cancer cases in North America and Europe than in Asian countries, South America and Africa (Figure 1.2). This difference may be due to genetic and lifestyle differences among populations, including diet and environmental exposures.

Mortality due to breast cancer is on decline in industrialized countries since the 1990s (Figure 1.1 (b)). This decline can be attributed to improvements in treatment and increasingly earlier detection, due to new or improved breast cancer screening and increasing awareness [17]. This highlights the importance to reliably detect cancerous masses, with any imaging system, at the earliest possible stage of development, when intervention is most effective.

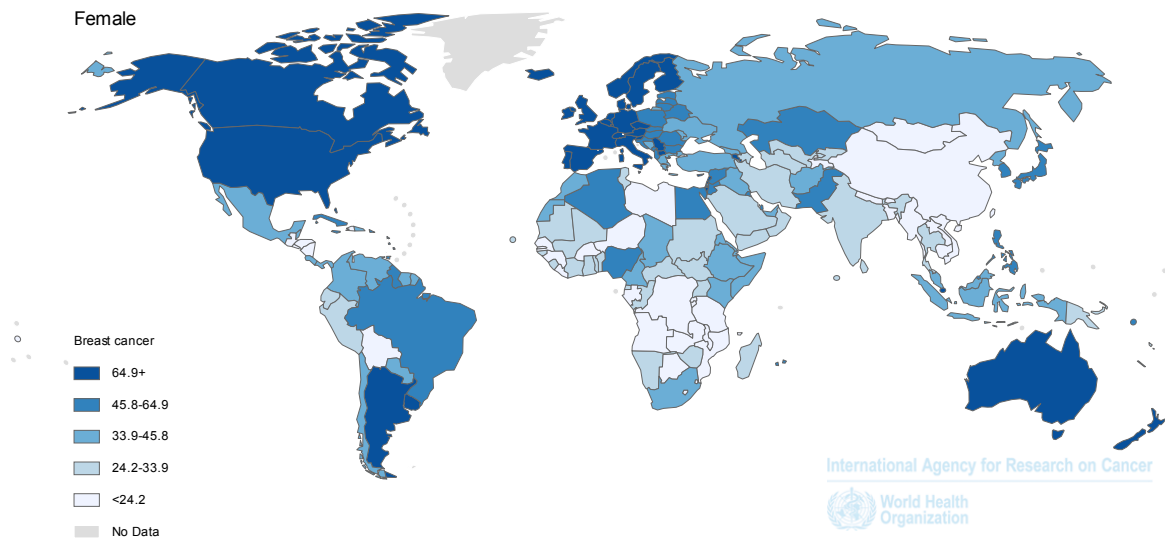


Figure 1.2: Estimated age-standardised incidence rate from breast cancer per 100,000 women around the world in 2012 [1].

1.1.1 Breast Imaging

Two criteria to evaluate the effectiveness of breast cancer imaging methods are sensitivity and specificity. Sensitivity represents the patients correctly identified as having breast cancer. Conversely, specificity portrays the healthy patients correctly diagnosed as not having the disease. Ideally, an imaging technology should meet these criteria and be inexpensive, non-invasive, involve minimum discomfort and be harmless to the patient and detect cancer at the earliest stage possible [5].

1.1.1.1 Conventional Techniques

X-ray mammography is currently the most common and effective breast screening method for detecting non-palpable early breast tumours, being a widespread low-cost technique. However, despite significant progress in improving mammographic techniques, X-ray mammography uses ionising radiation, requires an uncomfortable and painful breast compression, and has well-documented limitations related to sensitivity and specificity. This technique presents a high false-negative rate (up to 34%) [18], particularly in patients with radiographically dense breast tissue [19] which is especially common amongst younger women. The false-negative results can significantly delay treatment, often to the point where it is no longer effective. The false-positive rate associated with X-ray mammography can be as high as 70% [20]. These well-recognised limitations of X-ray mammography prompt the development of supplementary imaging modalities, specially for high-risk women [21].

Ultrasound and Magnetic Resonance Imaging (MRI) are established diagnostic techniques for breast cancer detection which do not expose the patient to ionizing radiation. Ultrasound techniques emit ultrasound waves that are reflected due to different acoustic

properties between tissues in the breast. It is considered to be appropriate for follow-up examinations once a suspicious region or abnormality is identified in an X-ray mammography, and also for examination of women with denser breasts [22]. Limitations of ultrasound include the high false negative rate [23], when compared to mammography, and the large amount of time required to carry out the examination. MRI is based on static magnetic fields acting on the hydrogen atoms of the different tissues of the body. MRI offers high contrast and spatial resolution and has been shown to be effective in detecting small tumours and imaging dense breast tissue [24]. MRI is currently unsuitable for widespread screening due to the highly variable reported values of sensitivity and specificity [24], the long examination time associated with acquiring and reading images and the associated high cost.

Other imaging modalities include Positron Emission Mammography (PEM) [25] and optical imaging [26], but currently there is still insufficient evidence to support their use for widespread breast cancer screening [21]. Particularly, the former technique is not indicated for common screening in its present form since it offers significantly higher radiation dose than an X-ray mammography [27]. Another alternative method, still in an early stage of research, is Microwave Imaging.

1.1.1.2 Microwave Imaging

Microwave Imaging techniques are based on dielectric differences between normal and tumour tissues of the breast at microwave frequencies (300 MHz – 300 GHz) [28, 29]. Malignant tumours present higher values for conductivity and relative permittivity due to a significantly high water-content, which is mainly caused by abnormal vascularisation and altered cell surface properties [30, 31]. Recently, it was found that dielectric contrast between malignant and normal fatty (or adipose) tissues in the breast can be as high as 10:1, whereas the contrast between healthy and malignant fibroglandular tissues in the breast is at most 10% [32]. This presents a challenging imaging scenario as most breast tumours develop in the fibroglandular tissues [33].

Compared to other conventional imaging modalities, in particular X-ray mammography, Microwave Imaging is attractive in several important aspects. Namely, it uses non-ionizing radiation, it offers good resolution, it avoids the compression of the breast and it is relatively low-cost [34]. Furthermore, although there is a significant signal attenuation in biological tissue [35], microwaves are considered promising in applications where penetration of up to 10 cm would suffice — which is the case in breast cancer scanning [33]. Finally, the amount of energy deposited within the breast is low [36] which potentially marks the modality as suitable for regular screening. In this context, Microwave Imaging should be considered as a complementary screening technique to X-ray mammography, for follow-up diagnosis and monitoring, or even as an alternative technique in case of the imaging of very dense breasts.

Several Microwave Imaging approaches have been proposed for breast cancer detection. The focus of this dissertation is on the Ultra-Wideband (UWB) radar imaging method, which involves illuminating the breast with a UWB pulse emitted by antennas, and recording the resulting backscattered signals. Subsequently, reflected waves are focused synthetically using a beamformer to create an energy profile of the breast to identify the presence and location of significant dielectric scatterers [37, 38]. High-energy regions potentially indicate the presence of tumours.

However, beyond the scope of this dissertation, there are other Microwave Imaging approaches that are worthwhile mentioning due to their great potential:

- **Microwave Tomography.** The goal of Microwave Tomography [39–41] is the reconstruction of the dielectric profile of the breast. In this context, the data are acquired in a plane by an array of sensors originating a 2D image. A stack of 2D images (slices) is then obtained to represent the 3D object [33]. The reconstruction of the dielectric profile is carried out slice by slice (each slice being processed independently) and involves the solution of a forward and inverse scattering problem which seeks to minimise the difference between measured and calculated electric fields. Despite promising experimental results [42–44], the downsides of Microwave Tomography are limited resolution and the fact that the reconstruction algorithms are computationally intensive [45]. Moreover, tomographic techniques generally require a large amount of *a priori* information [45] and a large number of antennas around the breast, which makes the imaging more complex.
- **Holography.** Holographic approaches [46–50] rely on the measurement of both magnitude and phase information. The interference pattern of a reference wave with the wave scattered from the target forms an intensity pattern at the acquisition aperture (called hologram). The reference wave illuminates the hologram to reconstruct the target’s reflectivity as a function of position in an inversion process. Holography, as well as UWB, simultaneously processes all measured data to produce the whole 3D image in a single reconstruction step [33].
- **Time-Reversal Finite Difference Time Domain (FDTD) methods.** The Time-Reversal FDTD method [51–53] involves a back-propagation technique where the received signal data is applied to time reversed FDTD equations. The wave converges back to a point source scatterer at the time corresponding to the maximum of the initial excitation.
- **Hybrid modalities.** There are mainly two hybrid approaches: Microwave-Induced Thermoacoustic Imaging and Microwave Elastography.
 - i) Microwave-Induced Thermoacoustic Imaging [54–57] uses both microwave and ultrasound imaging to achieve excellent microwave absorption contrast and ultrasound spatial resolution. It employs powerful microwave pulses to heat the tissue. Tissues of higher conductivity, such as malignant lesions, tend to heat more rapidly

than the surrounding healthy tissue. The tissue thermo-elastic expansion, resulting from the microwave-induced heating and the subsequent cooling, induces acoustic signals which are acquired at an ultrasound transducer. Since malignant tissue absorbs more energy, it emanates stronger thermoacoustic waves and thus, the most intense sources may indicate the presence and location of tumors.

ii) The underlying principle of Microwave Elastography [58] is that tumours in the breast are stiffer compared to the healthy tissues [59]. For example, large sized lesions can be felt as a lump during a palpation test. Therefore, when breast is compressed, the resulting strain in the internal tissues is different between normal and malignant tissues. In this approach, two UWB pulses measure the contrast in the stiffness of the healthy and malignant tissues before and after compression.

1.1.2 Axilla Imaging

In about 80% of detected breast cancer cases, cancer cells metastasise into the axillary lymph nodes, making their analysis an essential part of breast cancer staging [60, 61]. Thus, the evaluation of whether the cancer has spread beyond the breast is crucial to decide what follow-up exams and therapy to follow.

The state-of-the-art procedure to evaluate axillary metastasis is a Sentinel Node Biopsy (Figure 1.3) [63–66]. In this method, a radioactive tracer and/or a dye is injected in the breast to determine which lymph nodes are the first to receive drainage from the breast. These local lymph nodes are called the sentinel nodes [67]. The nodes are then surgically excised and their histopathological analysis is performed. If cancer cells are found in the nodes, this indicates the higher risk of metastatic breast cancer and an axillary dissection is performed [66, 68, 69]; otherwise it is assumed that the cancer has not spread. The

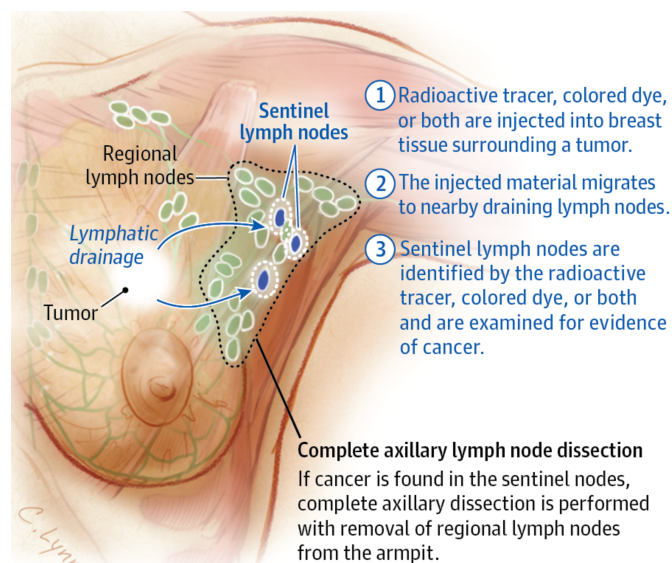


Figure 1.3: Sentinel lymph node biopsy [62].

Sentinel Node Biopsy is a highly accurate method of identifying the extent of cancer but it is still a time-consuming surgical procedure associated with some drawbacks such as long recovery, pain, and a significant risk of infection and lymphedema (build-up of fluid and swelling of the area where lymph nodes have been removed) [64, 70]. The removal of too many lymph nodes means that patients will not be able to drain lymph into the lymphatic system normally, and thus, patients will need to be closely monitored, hence preventing breast cancer patients from leading a normal life.

Preoperative non-invasive alternatives to assess the axillary staging could reduce the incidence of adverse events. Such techniques would need to demonstrate reliable sensitivity and specificity. Note that X-ray mammography in evaluating axillary lymph nodes offers limited visualization of the axilla because of positioning of the arm and therefore it is not typically used [71]. The best non-surgical alternatives currently under clinical study are Ultrasound-Guided Biopsy, MRI, Positron Emission Tomography (PET) and Computed Tomography (CT) [71].

Ultrasound-Guided Biopsy [72–75] is a minimally invasive technique that uses high-frequency sound waves to identify possible large metastatic axillary lymph nodes. For this method, an Ultrasound exam is performed to locate the abnormality and is then used to guide a needle into the lesion. Factors such as size and shape have been used to discriminate between malignant and benign lymph nodes [71, 73]. A sample tissue of the abnormality is then removed and assessed. This technique allows to avoid a sentinel lymph node biopsy in 20% of the cases with reported sensitivities of around 80% [74, 75]. However, it was recently argued that the standard performance of an axillary ultrasound is questionable and of limited value [76].

MRI [70, 77, 78] provides information about the size and morphology of lymph nodes. Additional information is achieved following the interstitial injection of a contrast agent (usually gadolinium) to generate high spatial resolution images of lymphatic vessels and lymph nodes (the technique is called Magnetic Resonance Lymphangiography) [77]. An advanced MRI technique that has also been used to differentiate healthy from malignant lymph nodes is Diffusion-Weighted Imaging [78, 79], which measures the ability of water molecules to freely diffuse in tissue. Moreover, a different modality called MRI Spectroscopy [80] can provide information regarding the concentrations of metabolites within the imaged tissue, which may be relevant to detect the presence of malignancy. Overall, MRI showed sensitivity and specificity in detecting malignant lymph nodes of above 80% and 70%, respectively.

PET is a nuclear medicine technique that relies on the use of a radiotracer to observe the increased metabolic activity of tumours compared to normal tissue. It is usually performed with CT which provides morphologic detail. The combination of CT with PET has yielded some interest for axillary lymph node staging [81–83]. Although it has been reported that PET/CT can be more accurate when compared to Ultrasound, due to low sensitivity in detecting axillary lymph node metastases (54%), high costs and radiation exposure, it cannot act as a substitute for Sentinel Node Biopsy [83].

Despite the presented alternatives, no imaging modality has yet shown satisfactory sensitivity or specificity for axillary lymph node detection and assessment. Another potential non-invasive approach to early detection of metastasis in lymph nodes is microwave imaging in which healthy and diseased lymph nodes can be identified due to different dielectric properties [28, 61, 84]. To the best of the author's knowledge, this section of work has never been attempted.

1.2 Objectives

Microwave Imaging has been extensively used to exploit the differences in dielectric properties between healthy and malignant tissues in the breast. Imaging of other parts of the human body has also been attempted, for example the brain [85, 86], the heel bone [87] or the knee [88]. However, imaging of the underarm region has never been attempted with a microwave UWB radar approach. The main objective of this dissertation is to create images of the axilla by adapting existing breast-related radar imaging algorithms. For that, the axilla needs to be modelled according to its anatomical structures and respective dielectric properties, which can be found in several studies [28, 61, 84].

UWB involves illuminating the underarm with a UWB pulse and recording resulting backscattered signals. Afterwards, the artefact removal has to be re-designed to compensate for the resulting high-backscattering in the air-skin region. Likewise, the beam-former, which will ultimately time-align all the reflected waves recorded at each antenna, will have to be adapted since the underarm model has significantly different tissues and consequently different dielectric properties, when compared to those of the breast. Another issue that has to be accounted for is the fact that tumours in the lymph nodes will be located at a more superficial position than breast tumours. Therefore, antennas will most likely record backscattered signals for a shorter period of time and/or may operate at higher frequencies. The planar UWB radar antenna configuration will also have to be designed in order to contemplate the imaging of the underarm.

With this system, it will be possible to identify the presence and location of significant dielectric scatterers within the axilla — potential sites where cancer cells metastasised to. This evaluation will be fundamental in the decision of what follow-up exams and therapy to follow in breast cancer patients, avoiding removing healthy lymph nodes and thus, reducing the risk of infection and other complications.

1.3 Dissertation Overview

The remainder of this dissertation is organised as described in this section.

Chapter 2 reviews the background literature related to the work developed in this dissertation. In particular, it provides an overview of the physiological background related to the axilla and metastasis of breast cancer, examines studies of dielectric properties of

healthy and diseased lymph nodes and briefly discusses the methodology and algorithms behind UWB Microwave Imaging.

Chapter 3 details the relevant materials for this study and explains the methodology followed in this project.

Chapter 4 summarizes the key results that show the effectiveness of selected image formation algorithms.

Chapter 5 provides the overall conclusions and suggestions for future work.

2

Background

In this Chapter the background information for understanding the results of this work is provided. The Chapter opens with an overview of the anatomy and physiology of the lymphatic system of the underarm in order to better understand the importance of this region in breast cancer diagnosis. The Chapter goes on, presenting studies on dielectric properties of the axillary tissue and addressing the Finite-Difference Time-Domain (FDTD) electromagnetic modelling method in Section 2.2. Section 2.3 concludes the chapter with the presentation of the algorithms for artefact removal and beamforming used in UWB radar Microwave Imaging.

2.1 Anatomical and Physiological Background

2.1.1 Lymphatic System of the Underarm

The lymphatic system, which is part of the immune system, includes a network of lymphatic vessels and lymph nodes running throughout the body. The main functions of this system is to maintain fluid balance, to absorb fats and other substances from the gastrointestinal tract and to participate in the defense from microorganisms and other foreign substances [89].

Fluids tend to move out of blood capillaries into the interstitium (spaces between tissue cells). The majority of this interstitial fluid moves back into the blood capillaries, but the excess enters the lymphatic capillaries to become lymph. If this excess of fluid was to remain in the interstitial fluid, tissue damage and eventual death would result [89]. In addition to water, lymph contains solutes such as ions, nutrients, gases, hormones, waste products and bacteria [90]. Lymph flow is unidirectional because of the

lymphatic valves [91] and is generated through contraction of lymphatic vessels, contraction of skeletal muscles or thoracic pressure changes [89]. Ultimately, the fluid is emptied into thoracic veins.

Lymphatic capillaries join to form larger lymphatic vessels, which in turn drain into a lymph node. Lymph nodes are round, oval, or bean-shaped bodies and are fixed in areas throughout the lymphatic vessels, ranging in size from 1 to 25 mm long [89]. Lymph nodes are mostly located near or on blood vessels and are categorized as superficial, if located in the hypodermis beneath the skin, or deep, if located elsewhere [89]. The depth of the axillary lymph nodes can range from 1.4 to 8.0 cm [92]. Lymph nodes store white blood cells (e.g., lymphocytes and macrophages) and are the only structures to filter lymph, removing damaged cells, microorganisms, tumour cells and foreign substances. The unfiltered lymph is delivered to the lymph nodes by several afferent vessels. However, only one or two efferent vessels exist, which means that the lymph in the nodes is somewhat stagnated giving time to the lymphocytes and macrophages to carry out their protective functions. The lymph nodes are connected together in series so that lymph leaving one lymph node is carried to another lymph node. A swollen lymph node may identify the location of a problem such as an injury, infection, or tumour in or near the lymph node. Lymph nodes in the underarm are called the axillary nodes.

Axillary lymph nodes form a chain of about 30 lymph nodes [89] from the underarm to the collarbone. Surgeons divide them into 3 levels, according to their relationship to the pectoral muscle on the chest (Figure 2.1) [71, 93, 94]:

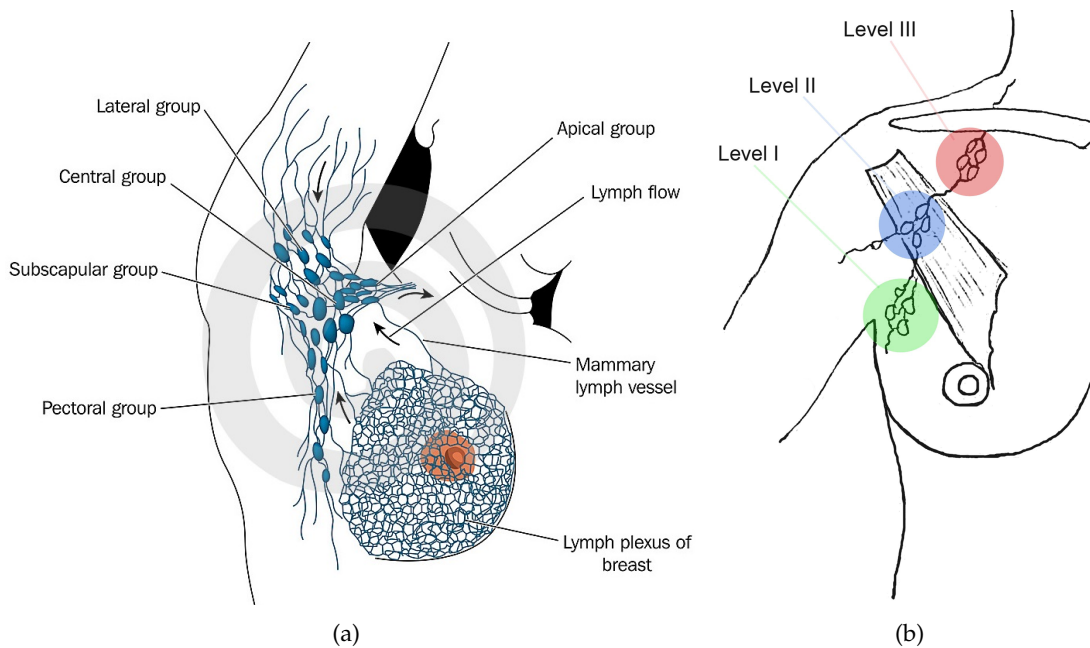


Figure 2.1: Axillary lymph nodes. (a) Illustration of the anatomical classification of the axillary lymph nodes [95]. (b) Illustration of the surgical classification (used in axillary dissection) of the axillary lymph nodes [71].

Level I: Consists of the nodes located in the lower part of the underarm, along the lateral border of the pectoral muscle. This level receives most of the lymph from the breast and includes the pectoral, subscapular and lateral nodes.

Level II: Consists of the nodes located in the middle part of the axilla, posterior to the pectoralis muscle. This level receives the fluid from Level I and some fluid from the breast and chest wall. It includes the central axillary nodes and some apical nodes.

Level III: Consists of the nodes located above the breast and below the centre of the collarbone, along the inside border of the pectoral muscle. This level receives fluid from Levels I and II and from the upper part of the breast and chest wall. It includes the remaining apical nodes.

2.1.2 Tumour Formation and Cancer Staging

Tumours are defined as an abnormal growth or division of undifferentiated cells. Generally, there are two possible origins for tumour cells: the existence of oncogenes, which are genes responsible for the proliferation of cells, and/or the repression of the genes that usually control cell proliferation. Tumours can be benign or malignant, depending if the growth is controlled or uncontrolled, respectively. Malignant tumours are a synonym of cancer [96].

Cancer cells can separate from the primary (original) tumour and spread (metastasise) to other parts of the body by entering lymphatic vessels. These cells eventually reach the blood, which in turn carries them to other parts of the body. We can therefore classify the cancer in 4 different stages, based on the size of the primary tumour and whether the cancer has spread in the body:

Stage 0: This stage is also called carcinoma *in situ* and describes cancers that are still located in the position where they started and have not invaded nearby tissues. This stage of cancer is often highly curable, usually by removing the entire tumour with surgery.

Stage I: This stage reflects a small cancer or tumour that has not grown deeply into nearby tissues, only with small clusters of cancer cells (not larger than 2 millimetres) in the lymph nodes. It is often called early-stage cancer.

Stage II and III: These stages indicate cancers or tumours that are larger in size, have grown into nearby tissue, and have spread to lymph nodes, but not to other parts of the body.

Stage IV: This stage means that the cancer has spread to other organs or parts of the body, most often the bones, lungs, liver, or brain.

Staging describes the severity of a person's cancer and therefore it is important for planning the appropriate treatment. More detailed information about the stages of breast cancer can be found in Table 2.1.

Table 2.1: Breast cancer staging. Adapted from [97].

Stage 0	Carcinoma <i>in situ</i> .	
Stage I	A	Tumour is 2 centimetres or smaller.
	B	Small clusters of breast cancer cells (between 0.2 and 2 millimetres) in the lymph nodes and either no tumour is found in the breast or the tumour is 2 centimetres or smaller.
Stage II	A	No tumour in the breast and cancer cells in 1 to 3 lymph nodes OR tumour is 2 centimetres or smaller and cancer cells in 1 to 3 lymph nodes OR tumour between 2 and 5 centimetres without cancer cells in the lymph nodes.
	B	Tumour between 2 and 5 centimetres and small clusters of cancer cells (between 0.2 and 2 millimetres) in the lymph nodes OR tumour between 2 and 5 centimetres and cancer cells in 1 to 3 lymph nodes OR tumour larger than 5 centimetres without cancer cells in the lymph nodes.
Stage III	A	No tumour or any size tumour in the breast and cancer cells in 4 to 9 axillary lymph nodes OR tumour larger than 5 centimetres and small clusters of cancer cells (between 0.2 and 2 millimetres) in the lymph nodes OR tumour larger than 5 centimetres and cancer cells in 1 to 3 lymph nodes.
	B	Any size tumour and cancer cells in the chest wall and/or in the skin of the breast (causing swelling or an ulcer). Cancer may spread to up to 9 lymph nodes.
	C	No tumour nor any size tumour in the breast and cancer cells in 10 or more axillary lymph nodes and/or in the chest wall and/or in the skin of the breast (causing swelling or an ulcer) OR cancer cells in lymph nodes above or below the collarbone OR cancer cells in axillary lymph nodes and lymph nodes near the breastbone.
Stage IV	Cancer cells in other parts of the body, most often the bones, lungs, liver, or brain.	

2.1.3 Breast Cancer Metastases

In the case of breast cancer, the examination of the axillary nodes to assess if they contain cancer cells is crucial to determine the stage of the cancer and the likelihood that breast cancer has metastasised to other parts of the body.

More than 75% of the lymph of the breast is drained by the axillary lymph nodes. Most of the remainder of the lymph passes to parasternal nodes [91, 94]. Furthermore, when breast cancer metastasise, it usually spreads to the level I nodes first [93], following anatomic order. The first regional lymph node to receive lymphatic fluid from a malignant tumour is called sentinel node [67]. The presence of metastasis in level III nodes, for example, without disease in levels I and II nodes is uncommon [71]. However, tumour cells are not always harboured in the first lymph node to which the lymph flows because lymphatic vessels and lymph nodes can relate in two different ways — lymphatic vessels

can either run through the lymph node and discharge its contents in that node or it can run over the surface of the lymph node without discharging its contents [91].

The detection of breast cancer metastasis in the axillary lymph nodes enables the evaluation of cancer staging [97]. This evaluation is necessary in order to decide what exams and therapy to follow. Since an early detection can increase the success of cancer treatment, it is of extreme importance to develop non-invasive approaches that accomplish this goal. One such technique is Microwave Imaging.

2.2 Axilla modelling

2.2.1 Dielectric Properties

UWB Microwave Imaging operates on the basis that electromagnetic scatterings are generated by the contrast that exists between tissues with different dielectric properties, particularly between normal and malignant tissue. Tumour cells have altered membrane composition and permeability which results in the movement of potassium, magnesium and calcium out of the cell and the accumulation of sodium and water into the cell [31]. The increase of water and sodium within cancerous tissue directly affect its dielectric properties. The dielectric contrast between tissues with different water content is responsible for high scattering in Microwave Imaging.

The relevant dielectric properties are relative permittivity and conductivity [98, 99]. As most human body tissues are non-magnetic, the magnetic permeability (μ) is very close to the permeability of free space and therefore is not considered [99]. In a general case, permittivity, ε , is a complex number measured in Farad per Metre (F/m) that consists of a real part (ε') and an imaginary part (ε''). The complex permittivity, ε , divided by the permittivity of free space, $\varepsilon_0 = 8.854 \times 10^{-12}$ F/m, is called relative permittivity, ε_r , which is dimensionless:

$$\varepsilon_r = \frac{\varepsilon}{\varepsilon_0} = \frac{\varepsilon' - j\varepsilon''}{\varepsilon_0} \quad (2.1)$$

Permittivity describes the interaction of a material with the electric field applied on it. The real part of the permittivity (ε') is a measure of how much energy from an external electric field is stored in the material. The imaginary part (ε'') is related to the dissipation of energy, which occurs when the electromagnetic energy is absorbed by the material [98, 99]. The imaginary part of permittivity (ε'') is always greater than zero and is usually much smaller than the real part (ε') [99]. The measured loss in the material (ε'') is related to both pure dielectric loss, ε_d'' , (e.g., dipolar and electronic polarization) and to another parameter called conductivity, σ , which is given in Siemens per Metre (S/m) [98]:

$$\varepsilon'' = \varepsilon_d'' + \frac{\sigma}{\omega} \quad (2.2)$$

where $\omega = 2\pi f$ is the angular frequency.

2.2.1.1 Dielectric Properties of Lymph nodes

Whereas there is a significant number of studies focusing on dielectric properties of tissues from breast and other organs/tissues within the human body [32, 100], information about lymph tissues is very sparse and there are only initial studies currently available. The following paragraphs examine the limited number of studies reporting lymph node dielectric properties.

In 1994, Joines *et al.* [28] performed in 1994, for the first time, 6 measurements of the conductivity and relative permittivity of malignant lymph nodes at frequencies between 50 and 900 MHz, a typical frequency range used for Microwave-Induced Hyperthermia. However, this study not only examined a limited number of lymph nodes but also did not include any healthy lymph nodes.

Later, Choi *et al.* [84] examined the electromagnetic properties of breast cancer cells, specially metastasised cancer cells in the lymph nodes, by employing broadband high-frequency microwaves ranging between 0.5 and 30 GHz. The study included 27 lymph nodes and 7 pure cancer tissues and showed that both cancer tissues and lymph nodes containing cancer cells differ significantly from normal lymph nodes. Figure 2.2 clearly shows that cancer tissues and metastasised lymph nodes exhibited higher values of permittivity compared to the normal nodes at low frequencies and higher values of conductivity at high frequencies. Although this suggested that it is possible to distinguish

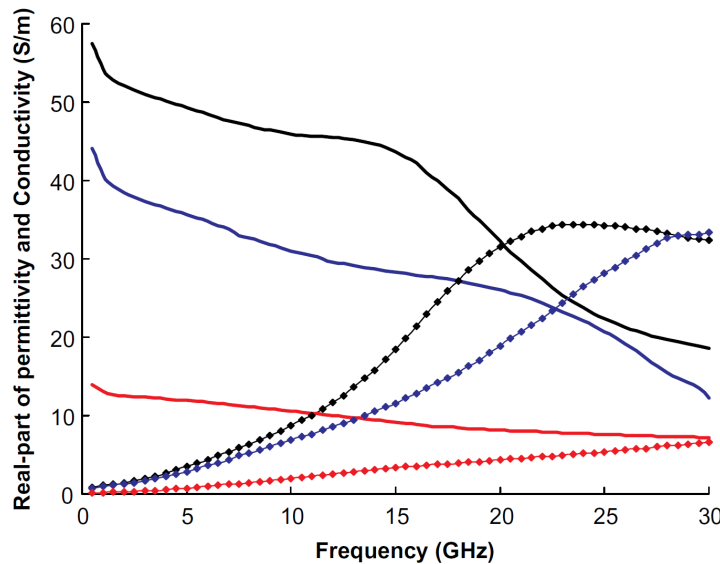


Figure 2.2: The variation of the relative permittivity and conductivity between 0.5 and 30 GHz of pure cancer tissues and metastasised lymph nodes in comparison to normal lymph nodes as reported by Choi *et al.* [84]. The solid line is the real part of the permittivity and the dotted line the imaginary part of the permittivity (ϵ''), which is considered to be $\epsilon'' = \sigma/\omega$. Black represents the cancer mass, blue the metastasised node, and red the normal node.

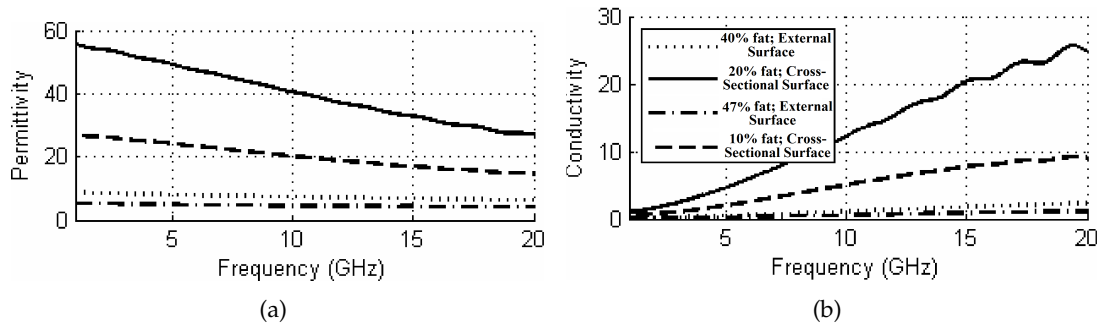


Figure 2.3: The variation of the (a) relative permittivity and (b) conductivity between 1 and 20 GHz, measured in the external and cross-sectional surfaces of healthy lymph nodes for samples from 2 patients as reported by Cameron *et al.* [61]. The measurements in the external surface of the node correspond to 40% and 47% fat beneath the probe whereas the cross-sectional measurements show 20% and 10% fat content under the measurement site.

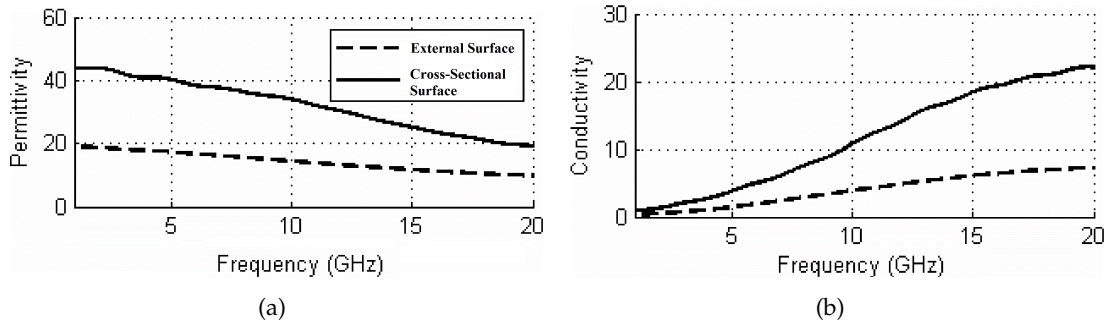


Figure 2.4: The variation of the (a) relative permittivity and (b) conductivity between 1 and 20 GHz, measured in the external and cross-sectional surfaces of lymph nodes containing tumour cells, as reported by Cameron *et al.* [61].

metastatic lymph nodes with high sensitivity using microwaves, various important aspects of the study (such as the sensing volume of the probe) are not detailed and thus, insight into the accuracy of the measurements is not available.

More recently, Cameron *et al.* [61] conducted a preliminary study of the electrical properties of healthy and malignant lymph nodes. They measured the dielectric properties in both the external and cross-sectional surfaces (after cutting the tissue sample) of the nodes, reporting higher permittivity and conductivity in the latter case (Figure 2.3) where the water content is higher. The study also revealed that lymph nodes contain more fat than originally expected and that fatty tissue dominates the measurements when the probe is placed in the exterior of the node. Nodes containing tumour cells were also included in the study, showing that the dielectric properties are higher in the cross-sectional surface due to higher tumour content, when compared to the external surface (Figure 2.4). The measurement results are encouraging but not conclusive, especially due to the limited number of samples. The authors plan to continue measurements in order to further understand the electrical properties of diseased and healthy lymph nodes and

thus, assess the impact of Microwave Imaging to aid breast cancer diagnosis.

2.2.2 Finite-Difference Time-Domain Method

A FDTD model is a numerical method commonly used to simulate the propagation of electromagnetic waves in a specified material, such as biological tissue [101, 102]. FDTD is based on a discrete solution of Maxwell's time-dependent equations:

$$\frac{\partial \mathbf{E}}{\partial t} = \frac{1}{\varepsilon_0} \nabla \times \mathbf{H} \quad (2.3)$$

$$\frac{\partial \mathbf{H}}{\partial t} = \frac{1}{\mu_0} \nabla \times \mathbf{E} \quad (2.4)$$

where \mathbf{E} is the electric field vector, \mathbf{H} is the magnetic field vector, ε_0 is the permittivity of free space, and μ_0 is the permeability of free space. In the FDTD approach, both space and time are divided into discrete segments. The calculation of the electromagnetic field values progresses at discrete steps in time using a leapfrog scheme [103] where, at each step, first the electric fields and then the magnetic fields are computed. FDTD methods are based on the approximation of partial derivatives by finite-differences. For the discretisation of the Maxwell's equations, the space and time and space resolutions, dx and dt respectively, need to be defined. Firstly, dx is chosen and finally the time step dt is determined using [104]:

$$dt = \frac{dx}{2c_0} \quad (2.5)$$

where c_0 is the speed of light.

The frequency-dependency of the dielectric properties of biological tissue is implemented in the FDTD model by the following Debye formulation [45]:

$$\varepsilon_r(\omega) = \varepsilon_\infty + \frac{\sigma_s}{j\omega\varepsilon_0} + \frac{\varepsilon_s - \varepsilon_\infty}{1 + j\omega\tau} \quad (2.6)$$

where ε_∞ is the permittivity at $\omega = \infty$, ε_s and σ_s are respectively the static permittivity and conductivity at $\omega = 0$, and τ is the relaxation time constant, which is the time required for the displaced system aligned in an electric field to return to $1/e$ of its random equilibrium value [99].

The FDTD method has been extensively used in several studies regarding Microwave Imaging of the breast [37, 45, 105, 106]. The method is employed because it is intuitive, highly accurate and efficient, does not use linear algebra which allows an infinite number of electromagnetic unknowns, it is simple to program and easily adapted to deal with a variety of problems [107, 108].

For the purpose of this dissertation, a FDTD model will be designed to simulate the electromagnetic behaviour of the underarm region when illuminated by an UWB radar system. The model needs to represent the lymph nodes, skin, muscle and bone in the upper arm. Each type of anatomical structure will be given its appropriate dielectric

properties as described in the literature [28, 61, 84, 100, 109–111].

2.3 Ultra-Wideband Radar Microwave Imaging

Ultra-wideband radar microwave imaging involves illuminating the axilla with an ultra-short UWB pulse (around 150 picoseconds), emitted by antennas at different locations surrounding the underarm, and recording the backscattered signals. In a monostatic system, each element of an antenna array sequentially transmits the UWB pulse and receives the reflected signals [38]. Instead of an array of antennas, a single antenna can also be used to scan the tissue at the various locations [37]. In a multistatic system, for each transmitting antenna, all antennas in the system are simultaneously receivers. An artefact removal algorithm is then applied to the recorded signals to subtract the high-backscattering responses caused by skin. Finally, a beamforming algorithm spatially focuses the backscattered signals in order to create an energy profile of the axilla to identify the presence and location of significant dielectric scatterers. High-energy regions may indicate the presence of metastasis in the lymph nodes. A block diagram of a monostatic UWB system for axilla Microwave Imaging is shown in Figure 2.5.

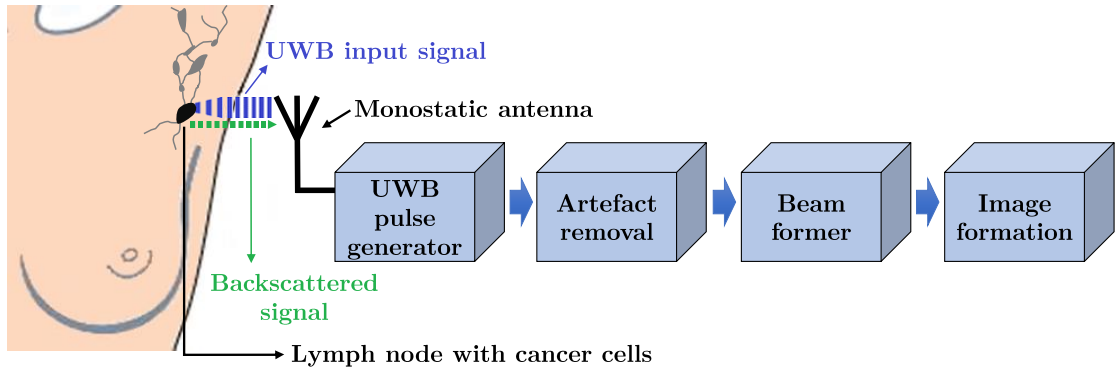


Figure 2.5: Generic diagram illustrating the proposed UWB radar Microwave Imaging system of the axilla.

Two different antenna configurations have been examined for breast imaging. In the planar configuration, first used by Hagness *et al.* [112], the patient is in the supine position with a planar antenna array placed across the naturally flattened breast. Conversely, in the cylindrical configuration, developed by Fear *et al.* [113], the patient lies in the prone position with a cylindrical array of antennas surrounding the breast, which is naturally extending through an opening in the examination table. For the purpose of this dissertation, a planar configuration and a monostatic system will be adopted.

In the following Section, a variety of artefact removal and beamforming algorithms are discussed.

2.3.1 Artefact Removal Algorithms

The stored backscattered signals include not only the tumour response, but also reflections from the skin. These reflections appear early in the time domain signal and are typically several orders of magnitude greater than the response from all other scatterers and therefore, if not removed, these could easily mask the tumour response [114]. This makes the artefact removal a critical component of any radar-based imaging system which needs to be applied before applying the focusing algorithm to form the image. A range of existing artefact removal algorithms are presented in the following paragraphs.

2.3.1.1 Average Subtraction

The simplest method was described by Li *et al.* [38] and consists in creating a reference waveform by averaging all the stored waveforms and then subtracting this reference from each of the original backscattered signals:

$$B_m = b_m - \frac{1}{M} \sum_{m=1}^M b_m \quad (2.7)$$

where M is the number of antennas, b_m is the original backscattered signal recorded at antenna m and B_m is the artefact-free signal. Since the artefact is dominant in the reference waveform and the tumour and clutter signals (due to heterogeneous tissue) are reduced to negligible levels, after the subtraction the result will essentially contain only the tumour response and clutter signals. This method, however, assumes that the artefact is identical for all antennas which in practice does not occur. This approach was adapted for the 3D case by Lim *et al.* in [115].

2.3.1.2 Rotation Subtraction

The Rotation Subtraction method was proposed by Klemm *et al.* [116] and requires two sets of measured data. The first set is recorded with a circular antenna array in one position and a second set of signals is recorded after the antenna array has been rotated around the vertical axis. In order to reduce the skin reflection, the second measurement is subtracted from the first one.

2.3.1.3 Adaptive Filtering

The artefact in the different antennas is similar but not identical due to local variations in skin thickness and tissue heterogeneity, as opposed to what is assumed by the simple Average Subtraction and Rotation Subtraction algorithms. In order to compensate for this variation, Bond *et al.* [117] proposed a method based on the Wiener Filter algorithm in which the artefact in each channel is estimated as a filtered combination of the signal in all other channels:

$$B_m = b_m - q^T b_c \quad (2.8)$$

where b_c is vector calculated from all other antennas except m , and q is the vector of filter weights. The filter weights are chosen to minimize the residual signal mean-squared error over the initial portion of the stored signal, which is dominated by the artefact. O'Halloran *et al.* [118] modified this algorithm to allow for the multistatic case. Here, the artefact removal algorithm first divides the signals into groups with similar artefacts, and then removes the artefact from each signal within the group. Maklad *et al.* [119] also modified the algorithm by selecting a physically and characteristically relevant neighbourhood of antennas to estimate each portion of skin response. The basic assumption of these algorithms is that, although the artefact will not be identical in each channel, it is recorded at approximately the same time, while any tumour response will appear at different positions in time due to the distance between the antennas.

Sill *et al.* [120] proposed a different adaptive filtering algorithm, based on the recursive least squares algorithm, in which the weight vectors are updated recursively after each time step. In contrast, the previous method [117] has a constant weight vector, which is shifted through the selected window.

2.3.1.4 Entropy Based Time Window

Adaptive filtering algorithms usually bring some distortion to the tumour reflection and are computationally complicated. In order to overcome these issues, Zhi and Chi [121] developed the Entropy Based Time Window artefact removal algorithm, based on the assumption that the artefacts have high similarity between the recorded data at different antennas and appear earlier in time, while the tumour response is delayed and attenuated differently in each channel. This method applies a time window function to the received signals, which is designed according to the entropy of the antenna signals at each time instant. Entropy is a measure of the variation of the signal and in this approach, a large entropy value, as a measure of high similarity, gives values of zero to the time window function, eliminating the artefact. This algorithm was shown to completely remove the part of signal estimated to contain the artefact but often failed to accurately estimate the exact portion of the signal containing the artefact [114].

2.3.1.5 Frequency Domain Pole Splitting

Firstly described by Maskooki *et al.* [122], this method employs a frequency domain model for the backscattered signal, representing each signal as a sum of complex exponentials, where each complex exponential represents a pole of the system and each pole corresponds to a specific scatterer. The information related with skin reflection can then be removed by removing the poles over a stated threshold, which correspond to the strongest scatterers. The reconstructed signal, which only contains the tumour and clutter response, is then converted into the time domain. As this method processes each signal individually, it adds no clutter from other channels. However, it tends to introduce considerable distortion in the tumour response [114].

2.3.1.6 Hybrid Artefact Removal Algorithm

Recently, Elahi *et al.* [123] proposed a novel artefact removal algorithm that combines the best attributes of the Entropy Based Time Window algorithm [121] and the adaptive Wiener Filter algorithm [117]. The first step of the proposed algorithm is to use an improved Entropy Based Time Window algorithm to estimate the part of the signal containing the artefact, based on entropy values. Once the artefact window has been defined, the Wiener Filter algorithm is applied over this window to estimate the artefact as a filtered combination of the signals in all other channels according to equation 2.8. This algorithm was shown to perform better in terms of signal and image quality when compared to the Entropy Based Time Window algorithm, for both homogeneous and heterogeneous scenarios [123].

2.3.2 Beamforming Algorithms

After artefact removal, beamforming is used to focus the backscattered signals to each pixel in the output image which correspond to specific focal points within the tissue. An effective beamforming algorithm must identify the presence and location of a tumour and provide high resolution while suppressing clutter due to the normal heterogeneity of biological tissue. Currently there are two main categories of beamformers, namely data-independent and data-adaptive. This section describes many different image reconstruction algorithms that have been proposed for the UWB microwave imaging technique.

2.3.2.1 Data-Independent Beamforming

Data-independent beamformers assume that the input signal propagates through a medium with known dielectric properties, and thus with known wave velocity. This information is then used to establish the delay and attenuation effects encountered by a radar signal. A number of data-independent beamformers used in the UWB breast imaging are described in the following paragraphs.

Delay-And-Sum

In 1998, Hagness *et al.* [105] implemented a 2D monostatic system based on the Delay And Sum (DAS) beamformer. The DAS beamformer involves time-shifting (delaying) and summing the backscattered signals to produce a synthetic focal point, which corresponds to each pixel in the image. First, time delays are calculated based on the distances from the focal point to each antenna in order to identify the contribution of each processed signal. Following the time-shifting of the signals according to the computed time delay, all contributions are added. If a tumour exists at a specific focal point, the returns from the tumour site will add coherently. Returns from clutter, due to natural heterogeneous tissue, will add incoherently and will be suppressed. In this way, tumour signals

are enhanced whereas clutter signals are minimized. The intensity of a pixel (I) in the reconstructed image is the square of the coherently summed values for a specific synthetic focal point at $\vec{r} = (x, y)$:

$$I(\vec{r}) = \int_0^{T_{\text{win}}} \left[\sum_{m=1}^M B_m(t - \tau_m(\vec{r})) \right]^2 dt \quad (2.9)$$

where M is the number of antennas, B_m is the m^{th} backscattered signal and $\tau_m(\vec{r})$ is the discrete time delay described as $\tau_m(\vec{r}) = 2d_m/(v_{\text{Tissue}}T_s)$, with $d_m = |\vec{r} - \vec{r}_m|$ being the distance between the m^{th} transmitting antenna at \vec{r}_m and the focal point (\vec{r}), v_{Tissue} the average velocity of signal propagation in breast tissue ($v_{\text{Tissue}} = c_0/\sqrt{\varepsilon_r}$, c_0 is the speed of light), T_s the sampling interval between data points and T_{win} the window length. The energy profile of the breast is created by varying the position of the synthetic focus from point to point (*i.e.* for each pixel) within the region of interest. High energy regions will likely indicate the presence of malignant tissue and low energy regions represent normal tissue.

In 2001, Li *et al.* [38] introduced the weights w_m in the DAS algorithm in order to compensate for attenuation due to 2D radial spreading of each UWB cylindrical pulse as it propagates outward from the transmitting antenna:

$$I(\vec{r}) = \int_0^{T_{\text{win}}} \left[\sum_{m=1}^M w_m B_m(t - \tau_m(\vec{r})) \right]^2 dt \quad (2.10)$$

Here, B_m represents the backscattered waveform after some processing, including an artefact removal. The radial spreading compensation was adapted to a 3D system by Fear *et al.* [37].

Nilavalan *et al.* [124] developed in 2003 the first multistatic DAS beamformer, where all M antennas record each backscatter signal. In such system, M^2 signals are recorded, but due to reciprocity, only $M(M - 1)/2$ signals need to be processed.

The main advantage of the DAS algorithm is its simplicity and short computation time.

Improved Delay-And-Sum

In 2008, Klemm *et al.* [116] evaluated, for a 3D multistatic system, a modified DAS beamforming using an additional weighting factor, QF (Quality Factor), to represent the quality of the coherent focusing algorithm. This factor is calculated in three steps. Firstly, for each focal point, \vec{r} , the energy is collected, cumulatively summed and plotted against the number of channels. Next, this curve is normalised by multiplying $1/(1 + \sigma_e)$, where σ_e is the standard deviation of energy for all radar signals used in the summation. Finally, a second order polynomial ($y = ax^2 + bx + c$) is fitted to the normalized energy collection and it is assumed that $\text{QF} = a$. This algorithm improves the signal-to-clutter ratio and its

characteristic equation is:

$$I(\vec{r}) = QF(\vec{r}) \cdot \int_0^{T_{\text{win}}} \left[\sum_{m=1}^{M(M-1)/2} w_m B_m(t - \tau_m(\vec{r})) \right]^2 dt \quad (2.11)$$

Delay-Multiply-And-Sum

In 2008, Lim *et al.* [115] proposed the Delay-Multiply -And-Sum (DMAS) algorithm, a similar approach to the DAS algorithm but with an additional pairing multiplication procedure after time shifting and before the time-shifted signals are summed and squared. The DMAS algorithm is based on the fact that by increasing sample size, additional clutter rejection is achieved. For example, considering 5 antennas in a monostatic system ($M = 5$), the clutter and noise rejection in DAS is achieved by summation of 5 (M) signals, whereas for DMAS, 10 (MC_2) signals are summed.

Channel-Ranked Delay-And-Sum

The previous algorithms assume that the tissue is dielectrically homogeneous. However, in case of heterogeneity, detection of tumours is much more challenging as signals with a longer propagation distance are more likely to encounter different dielectric properties, which reduce the quality of the microwave image due to incoherent addition. To compensate for that, O'Halloran *et al.* [125] developed an algorithm which gives extra weighting to signals with shorter propagation distances. Each multistatic signal is assigned a rank from 1 to M (M is the number of multistatic signals) according to its round-trip distance from the focal point, with the signal with the shortest propagation distance assigned a rank of 1. A weighting factor, w , is then calculated based on this ranking:

$$w = \frac{M - \text{rank}}{M(M - 1)/2} \quad (2.12)$$

This algorithm not only gives greater weighting to signals with shorter propagation distances, but also requires that the sum of the weights is always equal to 1, ensuring that weighting does not inhibit the imaging of cancerous tissue at significant distances.

Microwave Imaging via Space-Time

Bond *et al.* [117] and Davis *et al.* [126] developed the monostatic Microwave Imaging via Space-Time (MIST) beamforming. The main goal is to more effectively compensate for frequency-dependent propagation effects, such as path dependent dispersion and attenuation effects. The MIST beamformer firstly time-aligns the backscattered signals. Then, these signals pass through a bank of Finite-Impulse Response (FIR) filters, one in each antenna, and are summed to produce the beamformer output. The result is time-gated, and the energy for the point of interest is calculated. The filters solve a least-squares problem such that reflection from a possible tumour are passed with approximately unit gain

while the clutter and noise gain is reduced. O'Halloran *et al.* [118] adapted the MIST algorithm for the multistatic configuration (multi-MIST) showing that this algorithm significantly outperforms the monostatic MIST beamformer from which it is derived. In [127], the robustness of the multi-MIST algorithm was examined across a range of clinical scenarios including variations in dielectric properties and tumour positions and sizes.

Time-Difference-of-Arrival

The Time-Difference-of-Arrival (TDOA) algorithm, proposed in 2013 by Moll *et al.* [128], considers one transmitting antenna T_i and two receiving antennas R_j and R_k . If there is a tumour located at \vec{r} , the difference in times of arrival Δt_{jk} at the two antenna positions \vec{r}_j and \vec{r}_k is given by:

$$\Delta t_{jk}(\vec{r}) = \frac{1}{v_{\text{Tissue}}} (|\vec{r} - \vec{r}_j| - |\vec{r} - \vec{r}_k|) \quad (2.13)$$

where v_{Tissue} is an assumed constant velocity of signal propagation in breast tissue. Since the distance from the transmitter to the scatterer is the same for both receivers, it does not affect the differences in times of arrival when the wave velocity is constant. Hence, the three-dimensional intensity distribution can be obtained by a superposition of all transmitter-receiver combinations:

$$I(\vec{r}) = \sum_{i=1}^{M_T} \sum_{j=1}^{M_R-1} \sum_{k=j+1}^{M_R} c_{jk}(\Delta t_{jk}(\vec{r})) \quad (2.14)$$

where c_{jk} denotes the cross-correlation function between the receiver signals and M_T and M_R are the number of transmitting and receiving antennas, respectively.

2.3.2.2 Data-Adaptive Beamforming

Data-Adaptive beamforming describes how signals recorded by an antenna array are manipulated in order to achieve unit gain from a desired direction while suppressing signals of the same frequency from unwanted directions. Conversely to the data-independent beamformers, data-adaptive do not need *a-priori* information about the dielectric properties of tissue that in practice will not be available. The signal originating from the desired direction is estimated by varying the weights (or steering vector) applied to the antenna array. One popular Data-Adaptive beamformer is the Robust Capon Beamformer (RCB) implemented by Li *et al.* [129], which involves minimizing the output power of the beamformer while ensuring a unit gain in the direction of interest. Xie *et al.* [130] extended the approach for a Multistatic Adaptive Microwave Imaging (MAMI) algorithm by implementing the RCB in two stages in order to eliminate errors within the steering vector and making the algorithm more robust. Several changes have been introduced to the RCB to improve on the robustness of the algorithm such as Transmitter-Grouping RCB [131] and Double Constrained RCB [132].

In [133], Moll *et al.* extended the data-independent TDOA algorithm in order to not

require the wave velocity information. Here, the times-of-arrivals between two transmitters and one receiver is analysed directly in the time and not the spatial domain. As a result, the tumour was located correctly in moderate heterogeneous breast tissue.

In general, data-adaptive beamforming perform better than data-independent beamformers. In [134], data-adaptive methods outperformed DAS, and MAMI gave the best results in both homogeneous and heterogeneous breasts, while RCB showed a poor performance in the latter case.

2.3.3 Discussion and Conclusion

The success of the imaging procedure depends on many aspects, such as the type of UWB system (monostatic or multistatic) and the used algorithms for the artefact removal and beamforming.

The multistatic approach has been shown to significantly outperform monostatic imaging algorithms primarily because the former approach acquires many more reflections from the dielectric scatterers. Having this in mind, O'Halloran *et al.* [135] proposed a novel imaging technique to further increase the number of multistatic signals by rotating the antenna array around the breast. However, investigation of various antenna configurations and signal acquisition techniques for further improved imaging should be completed.

As stated, the skin artefact present in the received data needs to be removed and is an important step prior to the focusing algorithm and image formation. Elahi *et al.* [114] tested several artefact removal algorithms and observed that, although both Rotation Subtraction and Average Subtraction algorithms are computationally simple, they usually fail to remove the artefact due to local variations in the thickness of the skin and differences in the distance of each antenna to the skin. Conversely, Adaptive Filtering and the Frequency Domain Pole Splitting algorithms perform well but tend to introduce significant distortion in the tumour response. The Entropy Based Time Window algorithm completely removes the portion of the signal estimated to contain the artefact but sometimes fails to estimate that portion of the signal. The Hybrid Artefact Removal Algorithm combines the best attributes of the Entropy Based Time Window algorithm and the adaptive Wiener Filter algorithm performing better than each one individually. However, this still needs to be adapted to the multistatic case.

In order to create an energy profile, a beamforming algorithm is applied. O'Halloran *et al.* [136] tested the DAS, DMAS and IDAS with three realistic breast FDTD models. The authors observed that, although both IDAS and DMAS significantly outperformed DAS, breasts with higher content of fibroglandular tissue significantly caused reduced performance of IDAS and DMAS. In fact, in [137] it was shown that all of the tested beamforming algorithms (IDAS, Channel Ranked DAS and TDOA) allow for the correct localization of the tumour in an homogeneous breast tissue, but once the level of dielectric heterogeneity increased, the focusing algorithms failed in the tumour localization. The

main reason for that is the unknown wave velocity within the healthy tissues of the breast which is needed for the beamforming reconstruction methods. This prompts the development of more sophisticated beamformers that work independently of the wave velocity information and the degree of tissue dielectric heterogeneity. Data-adaptive imaging techniques attempt to overcome the shortcomings of data-independent algorithms by calculating a set of filter weights based only on the received signal data. Although they clearly improve the data-independent algorithms, false negative or false positive diagnosis may still occur as a result of multiple high energy regions within the energy profile. Additional imaging techniques need to be investigated in order to further reduce the effects of heterogeneous tissue and to clearly identify a tumour. As an example, contrast agents that modify the relative permittivity and conductivity of tissue (such as microbubbles and single-walled carbon nanotubes) are being investigated [138] to identify cancerous tissue within dielectrically heterogeneous breasts. These agents make the tumour a stronger scatterer due to an increased dielectric contrast between normal and malignant tissue.



Methods and Materials

In this Chapter a clear explanation of how this study was conducted is presented. The chapter starts by describing the relevant materials that were the bases of this dissertation and finishes by detailing the methods. Firstly, the procedure to simulate the propagation of electromagnetic waves in a numerical model of the axilla; secondly, the algorithms that were used to form images of the axilla from microwave signals; and finally the metrics that were used to evaluate the performance of each reconstruction algorithm. The simulation and all the algorithms were developed and tested in MATLAB^{®1} R2014a (version 8.3).

3.1 Materials

In order to accomplish the objectives of this dissertation and to examine the performance of each image formation algorithm, it was necessary to develop completely new 2D FDTD models that mimic the underarm region. The development of these numerical phantoms was completed by another researcher in the research group although I actively contributed to their development. In the FDTD models, each type of tissue is a new layer. Each model contains a 0.2 cm layer of skin and adipose tissue, which results in an overall axilla region thickness of 10 cm. A specific location within the FDTD model is given by: (*depth*, *span*) cm. In order to adequately evaluate the image formation algorithms, three models of the underarm with different tissue composition were considered, all of them accounting for the heterogeneity of the adipose tissue:

- **Simple heterogeneous model.** Comprises a single lymph node.

¹MATLAB is a registered trademark of The MathWorks, Inc.

- **Heterogeneous model.** Comprises two linked lymph nodes near the skin surface (healthy and metastasised).
- **Heterogeneous model with muscle.** Comprises two linked lymph nodes (in the anatomical levels I and/or II) and contains a 2.5 cm muscle layer which is 3.7 cm deep.

An example of a heterogeneous model with muscle is shown in Figure 3.1.

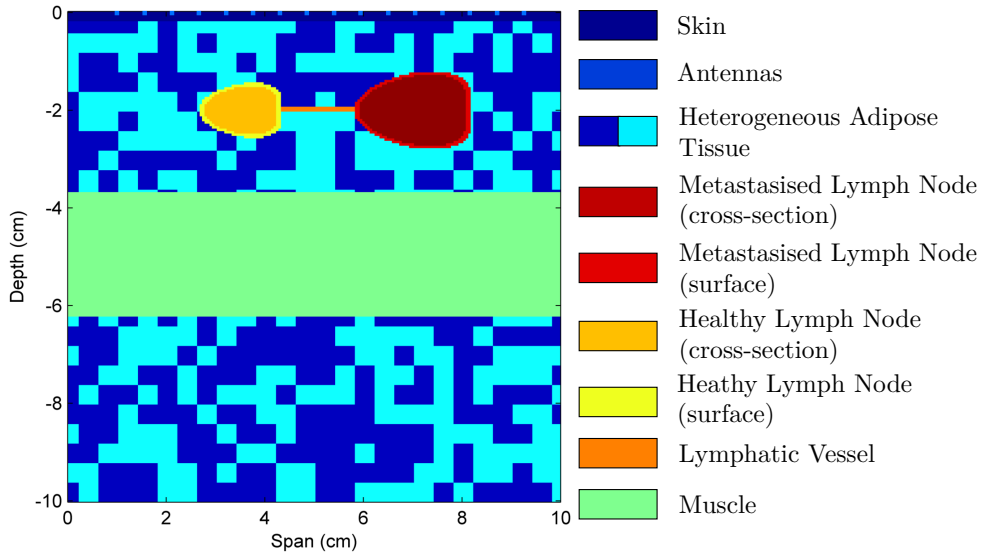


Figure 3.1: Representation of a heterogeneous model with muscle.

The lymph nodes are modelled with a bean-shaped curve [139] and can have different dimensions. Particularly, metastasised lymph nodes are usually bigger than healthy lymph nodes because lymph nodes swell when a tumour develops in or near them. In this dissertation, the size of a lymph node will always be referred to its larger axis, including the surface. The classification of the lymph nodes in the models is done according to their relationship to the muscle layer: level I lymph nodes are located above the muscle (2.0 cm deep) and level II lymph nodes are located at the muscle surface or inside the muscle. Level III lymph nodes are not modelled because, as it will be discussed later in Chapter 4, they are too deep in the axilla and they are not clearly visible with the tested image formation algorithms.

As noted in Chapter 2, the dispersive frequency-dependency of the dielectric properties of various tissues is implemented using a Debye model, given by Equation 2.6. The literature review concerning the dielectric properties was not intended for this dissertation, but it will be briefly exposed here for completeness. The Debye parameters for each type of tissue are shown in Table 3.1. Skin Debye parameters are obtained to fit published data by Zastrow *et al.* [109], healthy and malignant lymph nodes are modelled according to the dielectric properties found in studies by Cameron *et al.* [61], the dielectric properties for adipose tissue are based on the results described by Lazebnik *et al.* [110] and the

muscle properties are those described by Eleiwa *et al.* [111]. In order to account for the dielectric differences within adipose tissue, a dielectric variation of 10% with respect to the nominal property is randomly incorporated.

Table 3.1: Parameters of the Debye Formulation for the various tissues in the underarm that are represented in the FDTD models.

Tissues		Permittivity (ϵ_∞)	Conductivity (σ_s) [S/m]	$\epsilon_\infty - \epsilon_0$	Relaxation Time (τ) [ps]
Skin		15.93	0.831	23.83	13
Adipose Tissue		3.14	0.036	1.61	14.11
Muscle		47.8	5.58	25.4	6.79
Healthy	surface	8	2	3	9.24
Lymph Nodes	cross-section	47	6	27	9.4
Metastasised	surface	17	4	10	10.47
Lymph Nodes	cross-section	55	9	31	11
Lymphatic Vessel		8	2	3	9.24

3.2 Methods

3.2.1 FDTD Simulation Procedure

FDTD modelling, as briefly addressed in Section 2.2.2, is a numerical method commonly used for modelling the propagation of electromagnetic signals in biological tissues. The method is detailed in [104], which presents an implementation of the method in C programming language. This implementation was adapted to MATLAB environment to simulate a microwave radar system using the developed axilla numerical phantoms. With this method, representative backscatter signals are computed allowing the evaluation of the image formation algorithms presented in Sections 3.2.2 and 3.2.3. In total, 42 FDTD simulations in different imaging scenarios were carried out.

The FDTD grid resolution, dx , is 0.5 mm and the time step, dt , is calculated by means of Equation 2.5 as 0.833 ps. A Perfectly Matched Layer [140] is used as an absorbing boundary condition so that the reflections of propagating electromagnetic fields from the edges of the FDTD mesh are minimized. The antenna array is composed of 17 elements placed on the skin, equally spaced and spread over a distance of 80 mm. The number of antennas is 17 because this was found to be the optimized number that offered the best compromise of performance versus efficiency for a Microwave Imaging system in a planar configuration with the same antenna span [34]. During a scan, each antenna sequentially illuminates the phantom with a UWB pulse and the backscattered signal

is recorded at the same antenna. Prior to further processing, all the FDTD signals are downsampled from the sampling frequency of the FDTD simulation, from 1200 GHz to 50 GHz.

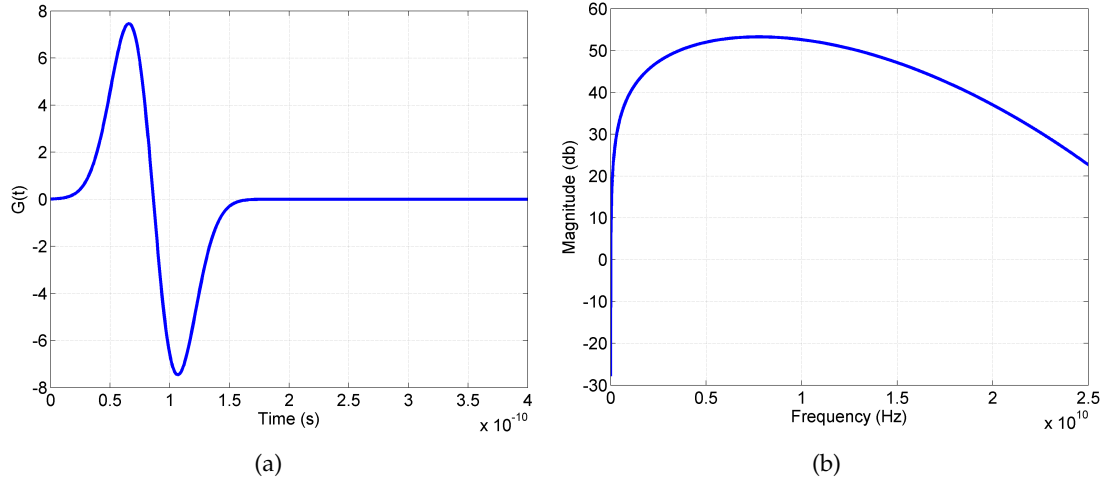


Figure 3.2: Representation of the UWB input signal. (a) Time-domain of the pulse. (b) Magnitude spectra of the pulse.

The input pulse, $G(t)$, is a 150 ps differentiated Gaussian pulse with a centre frequency of 7.5 GHz and a -3 dB bandwidth of 9 GHz, defined as:

$$G(t) = a \times (t - b) \times e^{-\frac{(t-b)^2}{\tau^2}} \quad (3.1)$$

where $a = -0.25$, $\tau = 35$ and $b = 3 \times \tau$. The time-domain and magnitude spectra of this pulse are represented in Figure 3.2.

3.2.2 Artefact Removal Algorithms

An overview of several artefact removal algorithms found in the literature was provided in Chapter 2. In this dissertation, the following artefact removal algorithms are investigated:

"Ideal": As previously applied by Conceição *et al.* [34], this artefact removal is implemented by subtracting the backscattered signals from a homogeneous FDTD model with no lymph nodes nor muscle from the backscattered signals obtained with the heterogeneous FDTD model containing lymph nodes (and possibly muscle), allowing for the isolated skin backscatter to be removed. The “ideal” artefact removal is introduced in this chapter as it potentially removes the artefact more efficiently and can be used to clearly examine the performance of the beamformers.

Average Subtraction: This artefact removal is implemented by subtracting the average of all the stored waveforms from each of the original backscattered signals.

Adaptive Filtering: In this algorithm developed by Bond *et al.* [117], the artefact in each channel is estimated as a filtered combination of the signal in all other channels. For this algorithm, the filter weights are chosen to minimize the residual signal mean-squared error over the portion of the signal dominated by the artefact. Without loss of generality, suppose we want to remove the artefact from channel 1, the artefact at the n^{th} sample of the first antenna is estimated from successive samples centred on that sample. The $(2J + 1) \times 1$ vector of time samples in the m^{th} channel is defined as:

$$b_m(n) = [b_m(n - J), \dots, b_m(n), \dots, b_m(n + J)]^T, 2 \leq m \leq M \quad (3.2)$$

where J is the number of samples on either side of the n^{th} time sample. The samples of $b_m(n)$ for the channels 2 to M are concatenated into a vector $b_{2M}(n) = [b_2^T(n), \dots, b_M^T(n)]^T$. The filter weight vector q is then chosen according to:

$$q = \underset{q}{\operatorname{argmin}} \sum_{n=n_0}^{n_0+m-1} b_1(n) - q^T b_{2M}(n)^2 \quad (3.3)$$

where the time interval $n = n_0$ to $n_0 + m - 1$ represents the initial portion of the recorded data that contains the artefact and no backscattered signals from lesions. The solution to this minimization problem can be described as:

$$q = \sum_{i=1}^p \frac{1}{\lambda_i} u_i u_i^T \times \frac{1}{m} \sum_{n=n_0}^{n_0+m-1} b_{2M}(n) b_1(n) \quad (3.4)$$

where λ_i , $1 \leq i \leq p$ are the p significant eigenvalues and u_i the corresponding eigenvectors. For the purpose of this work, this algorithm was implemented with a window length from $n = 6$ to 40, $J = 3$ and $p = 5$. These values were empirically found to be the values that give the best quality images of the axilla (the image quality is described by several performance metrics which are discussed in Section 3.2.4).

3.2.3 Beamforming Algorithms

Several beamforming algorithms were described in Chapter 2. This study attempts to examine the performance of the following beamformers for the formation of an image of the axilla:

DAS: The implemented DAS algorithm was presented by Hagness *et al.* [105], in which the signals are first time shifted and then summed. In Figure 3.3, a diagram of this beamformer is presented.

DMAS: The DMAS algorithm, proposed by Lim *et al.* [115], is similar to the DAS algorithm but additional pairing multiplication procedure after time shifting is applied.

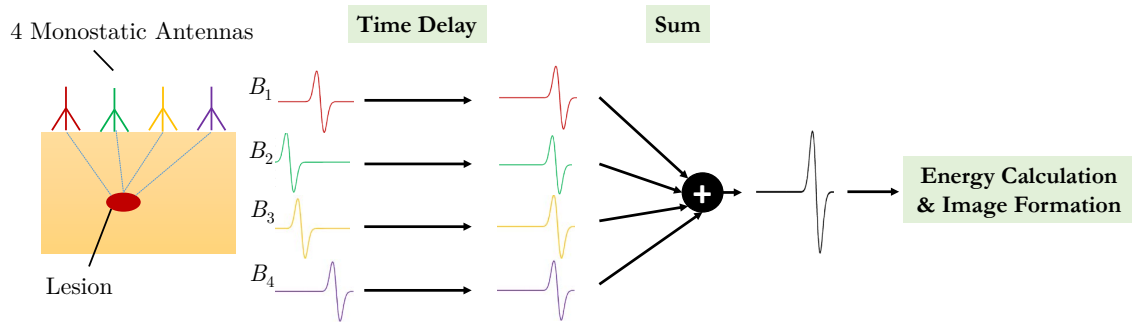


Figure 3.3: Diagram of the monostatic DAS beamforming algorithm with $M = 4$ antennas. All other beamformers (DMAS, Channel-Ranked DAS and Channel-Ranked DMAS) are derived from this one.

Channel-Ranked DAS: This algorithm was developed by O'Halloran *et al.* [125] and, comparing to the DAS algorithm, gives extra weighting to signals with shorter propagation distances. This means that, for example, in Figure 3.3, the DMAS algorithm will attribute higher weight to the signal B_2 when compared to the signal B_4 .

Channel-Ranked DMAS: This is a novel algorithm that was developed during this dissertation. It applies the Channel-Ranked DAS to the DMAS algorithm taking into consideration not only the propagation distances of each signal (as Channel-Ranked DAS) but also a higher number of signals due to the additional pairing multiplication procedure (as DMAS).

For each beamformer, the focal point energy is calculated across a window. For this work, a time window of 6 samples was found to be the optimum value and remained constant throughout the experiment. However, as noted by Bond *et al.* [117], the duration of the backscattered response is proportional to tumour size, and so a larger window would be more appropriate if the tumour is expected to be larger.

3.2.4 Performance Metrics

A range of different metrics are used in order to evaluate the performance and robustness of each image formation algorithm. Particularly, these metrics are used to measure the ability of the imaging system to highlight cancerous lymph nodes in the presence of clutter, to distinguish between diseased and healthy lymph nodes and to accurately localize the centre of the metastasis. The following performance metrics were used:

- **Full Width Half Maximum (FWHM).** Measures the distance between the peak response of the detected metastasised lymph node and the point at which the energy of this response drops to half. It expresses the physical extent of the metastasis response [34, 37].

- **Signal-to-Clutter Ratio (SCR).** Compares the maximum metastasis response to the maximum clutter response. The maximum clutter response is the maximum pixel value of the image in the area that excludes the response from any lymph node up to twice the extent of the FWHM value [34, 37].
- **Signal-to-Mean Ratio (SMR).** Describes the ratio of the maximum metastasis response to the average energy response of all the tissues within the axilla, excluding the response from any lymph node up to twice the extent of the FWHM value [34, 115].
- **Max-to-Max Ratio (MMR).** Compares the maximum metastasised lymph node response to the maximum response from healthy lymph nodes.
- **Localisation Error (L_{error}).** Calculates the difference between the location of the metastasis peak response and the actual location of the metastasised lymph node. This metric, as well as FWHM, determines the effectiveness of the system in localising the tumour within the axilla [34, 118].

4

Results and Discussion

The purpose of this chapter is to summarize the key results that show the efficiency of the image formation algorithms presented in Chapter 3. For that, the algorithms are applied to simulated backscattered signals recorded at an array of antennas, after illuminating a numerical phantom of the axilla with a UWB pulse. In this Chapter, the computation of a set of backscattered signals is first discussed and then, the results of applying the image formation algorithms to the backscattered signals using a variety of numerical phantoms of the axilla are presented. The relevant performance metrics are also presented and analysed for each simulation.

4.1 Computational Electromagnetic Simulation for Data Acquisition

The backscattered signals calculated using the FDTD method are an approximation to the signals that would be acquired from a real clinical setting. Figure 4.1 (a) (solid blue curve) illustrates the recorded backscattered signal in the first antenna (of an array of 17 antennas) using a simple 2D model of the axilla, consisting in a layer of skin and in heterogeneous tissue surrounding a metastasised lymph node placed 2.0 cm deep. After recording, these signals are processed to remove their artefact caused by skin. The performance of this process is illustrated in the figure, where it is clearly seen that prior to applying an artefact removal algorithm (solid blue curve), the early-time response is dominated by the incident pulse and the skin response. After applying the artefact removal (dotted red curve), the results demonstrate that the early-time response is almost

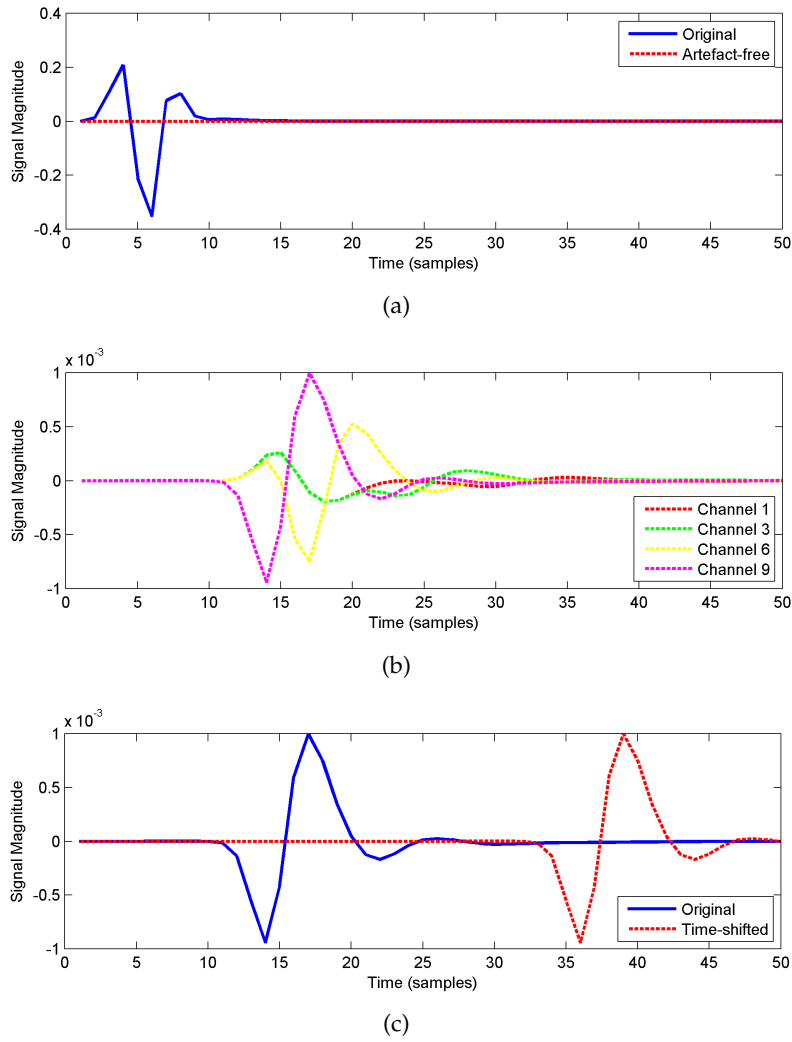


Figure 4.1: Computed FDTD backscattered signals (note the different scales in the Signal Magnitude axes between plots). (a) Signals before and after applying the Adaptive Filtering artefact removal. (b) Late-time responses after applying the Adaptive Filtering artefact removal at 4 different channels. (c) Artefact-free signal at channel 9 before and after time-shifting.

completely eliminated while, as shown in Figure 4.1 (b), the late-time response is preserved. This figure shows that the late-time response at four different antennas contains the tumour response and clutter due to the heterogeneity of the underarm. The tumour response appears, as expected, earlier in channel 9 because it is closer to the metastasised lymph node, and later in channel 1 since this is the furthest antenna. After removing the artefact, a beamforming algorithm is applied to focus the backscattered signals. A common step to all beamformers is the time-shifting which is calculated based on the distances from the focal point to each antenna in order to identify the contribution of each processed signal. Figure 4.1 (c) illustrates the processed signal in channel 9, where a time delay of 23 samples is successfully applied.

4.2 Simple Heterogeneous FDTD Models

After established in Section 4.1 that the FDTD simulation is working correctly, the first experiment consists in applying each algorithm to a simple numerical phantom (Figure 4.2 (a)) that includes a single metastasised lymph node of 22 mm located at (-2.0, 5.0) cm. This phantom accounts for heterogeneity of the adipose tissue by including a random dielectric variation of 10% with respect to the nominal property. Table 4.1 illustrates the overall performance of each artefact removal and beamforming algorithm in terms of SCR, SMR, FWHM and L_{error} . MMR is not calculated as it compares the response of metastasised lymph nodes to the response from healthy lymph nodes, and in this scenario the phantom only contains a single lymph node.

The performance of the selected beamforming algorithms (DAS, DMAS, Channel-Ranked DAS and Channel-Ranked DMAS) is compared based on the "Ideal" artefact removal results. It is possible to conclude that the SCR results are similar for every beamformer, but both DMAS and Channel-Ranked DMAS significantly outperform the DAS and Channel-Ranked DAS beamformers, as the former two beamformers have average SMR results of 27.43 dB compared to 23.02 dB for the latter two beamformers. Furthermore, the response of the metastasised lymph node is better focused when using DMAS and Channel-Ranked DMAS as represented by the lowest values of FWHM. Among the selected beamformers, DAS can be considered the weakest algorithm and, although DMAS and Channel-Ranked DMAS perform similarly, DMAS can be considered the strongest beamformer for this situation due to slightly higher SMR and lower FWHM.

Examining the overall performance of the selected artefact removal algorithms, the

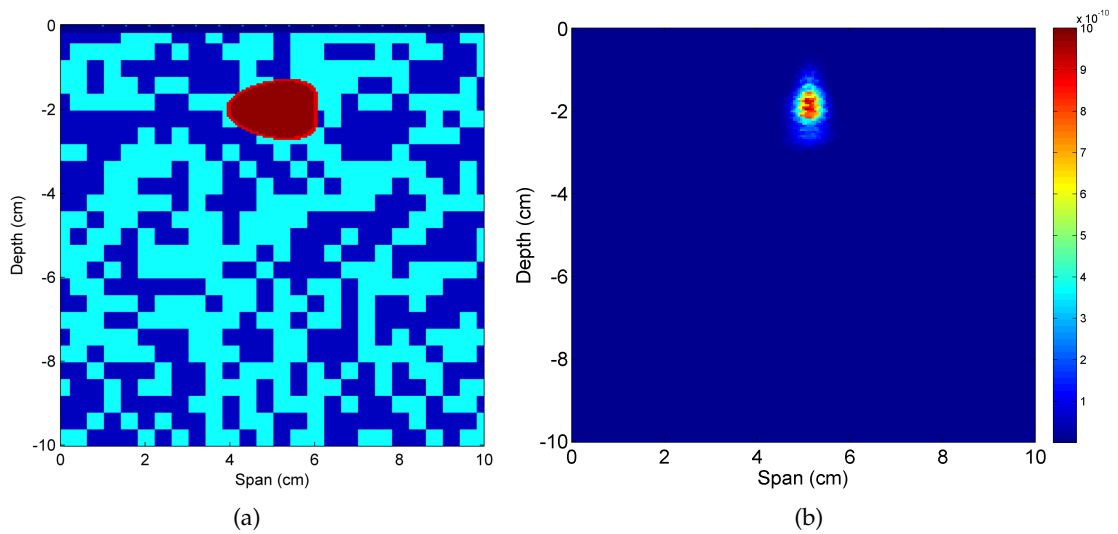


Figure 4.2: Image formation using Adaptive Filtering and DMAS. (a) FDTD model of the underarm with a 20 mm metastasised lymph node at 2 cm from skin. (b) Resulting image of backscattered energy.

Table 4.1: Performance metric results of the selected artefact removals ("Ideal", Average Subtraction and Adaptive Filtering) and beamformers (DAS, DMAS, Channel-Ranked DAS and Channel-Ranked DMAS) for a simple heterogeneous FDTD model of the axilla with one lymph node at location (-2.0, 5.0) cm.

		DAS	DMAS	Channel-Ranked DAS	Channel-Ranked DMAS
"Ideal"	SCR (dB)	3.02	3.03	3.03	3.04
	SMR (dB)	23.27	27.52	22.77	27.34
	FWHM (mm)	7.25	5.00	9.25	6.00
	Error (mm)	16.07	16.07	16.07	16.07
Average Subtraction	SCR (dB)	3.02	3.03	3.02	3.07
	SMR (dB)	22.85	28.78	21.80	28.24
	FWHM (mm)	8.75	4.75	9.00	5.75
	Error (mm)	17.01	17.01	17.18	17.18
Adaptive Filtering	SCR (dB)	3.02	3.03	3.01	3.05
	SMR (dB)	23.07	28.80	22.93	28.41
	FWHM (mm)	8.25	4.75	8.75	5.75
	Error (mm)	17.01	17.01	17.18	17.18

Adaptive Filtering offers higher SCR and SMR and lower FWHM values when compared to Average Subtraction, for all the beamforming algorithms. These results are consistent with the findings in [114] regarding breast tumour detection, which concluded that Adaptive Filtering not only removes almost all the skin artefact, but it also preserves the tumour response in contrast to Average Subtraction that frequently fails to effectively remove the artefact. The resulting image of backscattered energy using the Adaptive Filtering and DMAS algorithms is shown in Figure 4.2 (b).

The analysis presented in this Section can be replicated to evaluate the performance of the algorithms in the remaining FDTD models. Therefore, in the interest of brevity, in some subsequent results only the algorithms that yielded the best results are presented. In most scenarios, applying Adaptive Filtering and DMAS yielded the best results.

4.2.1 Effects of Natural Variations in Dielectric Properties

The dielectric properties of the underarm tissue may vary significantly between patients. Therefore, in order to examine the performance of the image formation algorithms to this variation, simulations were run for different percentages of variation of the relative permittivity of the tissue surrounding the lymph node, ranging from 0% (homogeneous FDTD model) to 50% in steps of 10%. The simulations were also carried out for two different tumour depths, 2.0 cm and 4.9 cm. The SCR and SMR metrics results using Adaptive Filtering with DMAS are plotted in Figure 4.3. The L_{error} and FWHM metrics are not plotted as they do not vary significantly with the varying dielectric properties compared to

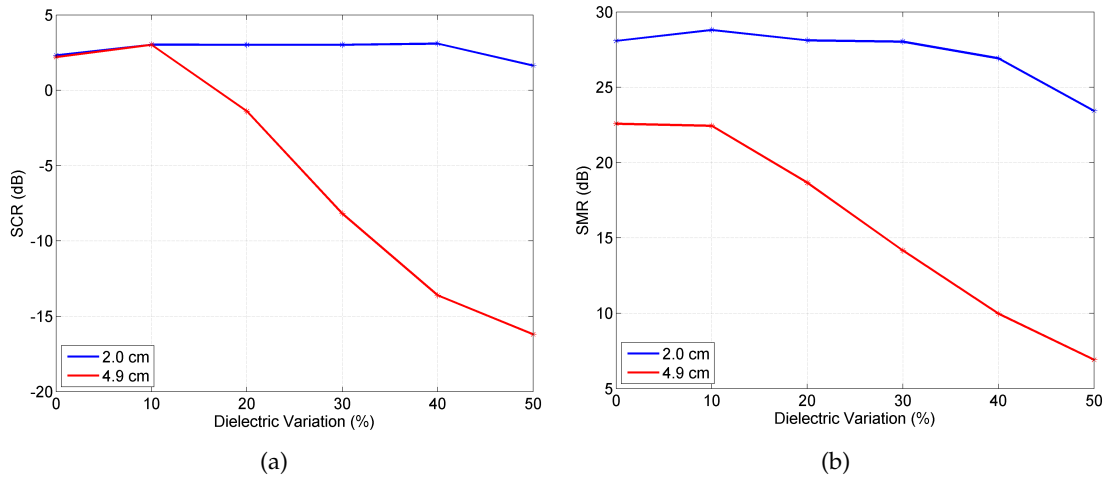


Figure 4.3: Effects of dielectric heterogeneity for lymph nodes at two different depths: 2.0 cm and 4.9 cm. The metrics (a) SCR and (b) SMR correspond to the use of the Adaptive Filtering artefact removal and the DMAS beamformer.

SCR and SMR. The behaviour of all the other combinations of artefact removal and beamforming algorithms is very similar (but with poorer performance metric values compared to Adaptive Filtering with DMAS) and therefore, due to space constraints, these will not be shown.

Overall, both the SCR and SMR decrease significantly with increasing dielectric variation of the axilla, demonstrating that the peak energy response of the metastasised lymph node is better distinguishable in the presence of low tissue heterogeneity. These metric results are particularly worse for a deeper tumour because the extension of heterogeneous tissue encountered by the signals is higher, which makes the imaging problem more difficult. Conversely, for a superficial lymph node, the performance of the combination of Adaptive filtering with DMAS beamformer remains approximately constant with increasing dielectric variation. By visual inspection of the energy profile of the axilla for a tumour located at a depth of 4.9 cm (Figure 4.4), the tumour is still visible for the highest level of heterogeneity ($\pm 50\%$), but there are also significant non-cancerous high energy regions. The reason behind this is that all the implemented beamformers are data-independent, which means that they assume that the input signal propagates through a homogeneous medium with known dielectric properties, and thus with known wave velocity. However, dielectric heterogeneity means that the signals propagate through tissue with different dielectric properties. The significant difference between the assumed homogeneous model and the actual heterogeneous model causes a much more erratic behaviour in the constructive addition of backscattered signals.

4.2.2 Effects of Increasing Tumour Depth

The depth of the axillary lymph nodes can show large variability (from 1.4 to 8.0 cm [92]). As a result, the proposed microwave imaging system was tested with a tumour located

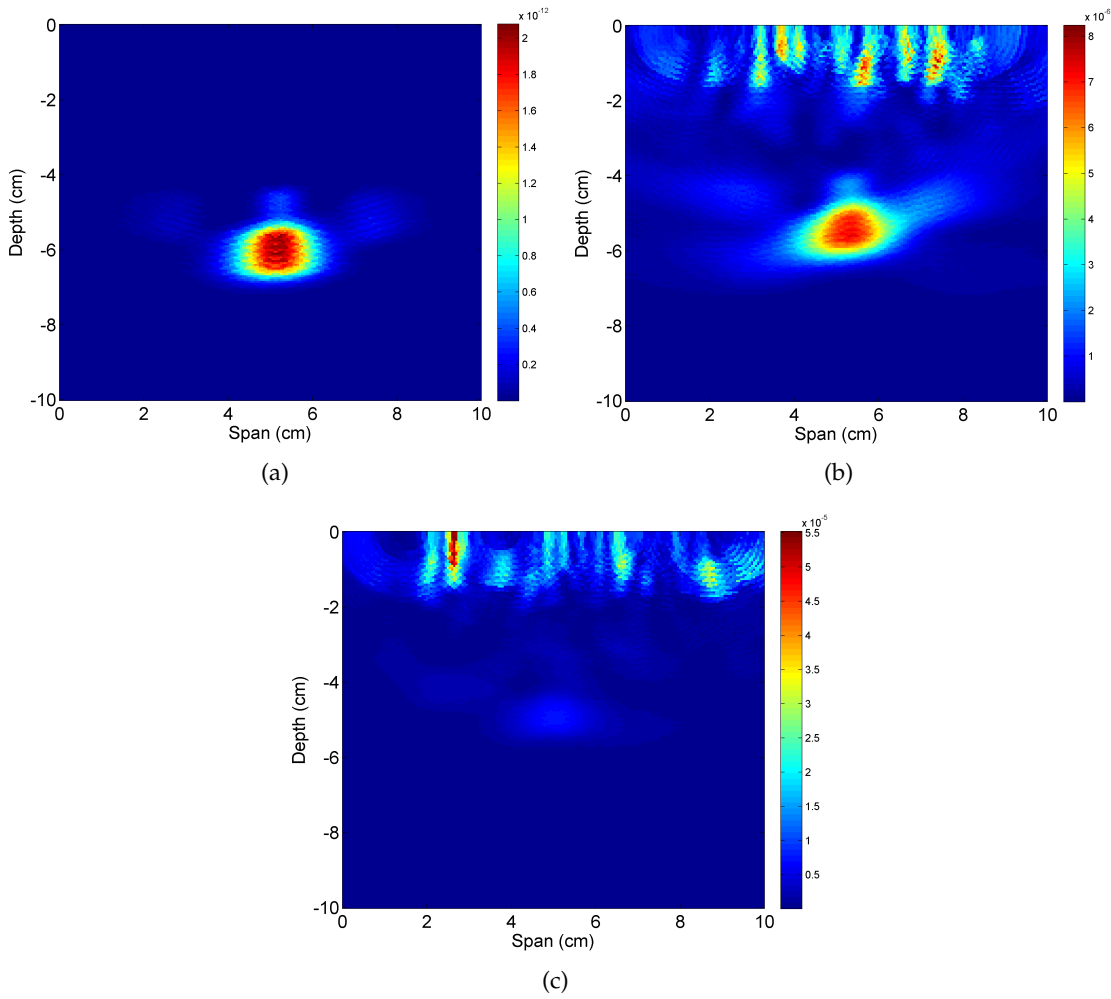


Figure 4.4: Images of backscattered energy using the Adaptive Filtering artefact removal and the DMAS beamformer for a tumour located at a depth of 4.9 cm, with (a) 0%, (b) $\pm 20\%$ and (c) $\pm 50\%$ of dielectric variation of the tissue surrounding the lymph node, respectively.

at three different depths, namely at: 2.0 cm, 4.9 cm and 8.2 cm. The numerical phantoms and the resulting simulated backscattered images using Adaptive Filtering with DMAS are shown in Figure 4.5 and the corresponding performance metrics are presented in Table 4.2. As clearly noted, the performance of the system tends to worsen when the

Table 4.2: Metric results for a metastasised lymph node located at different depths using the Adaptive Filtering artefact removal and the DMAS beamformer.

Depth	SCR (dB)	SMR (dB)	FWHM (mm)	L_{error} (mm)
2.0 cm	3.03	28.80	5.75	17.01
4.9 cm	3.02	22.44	13.75	41.84
8.2 cm	-9.42	11.93	26.5	79.83

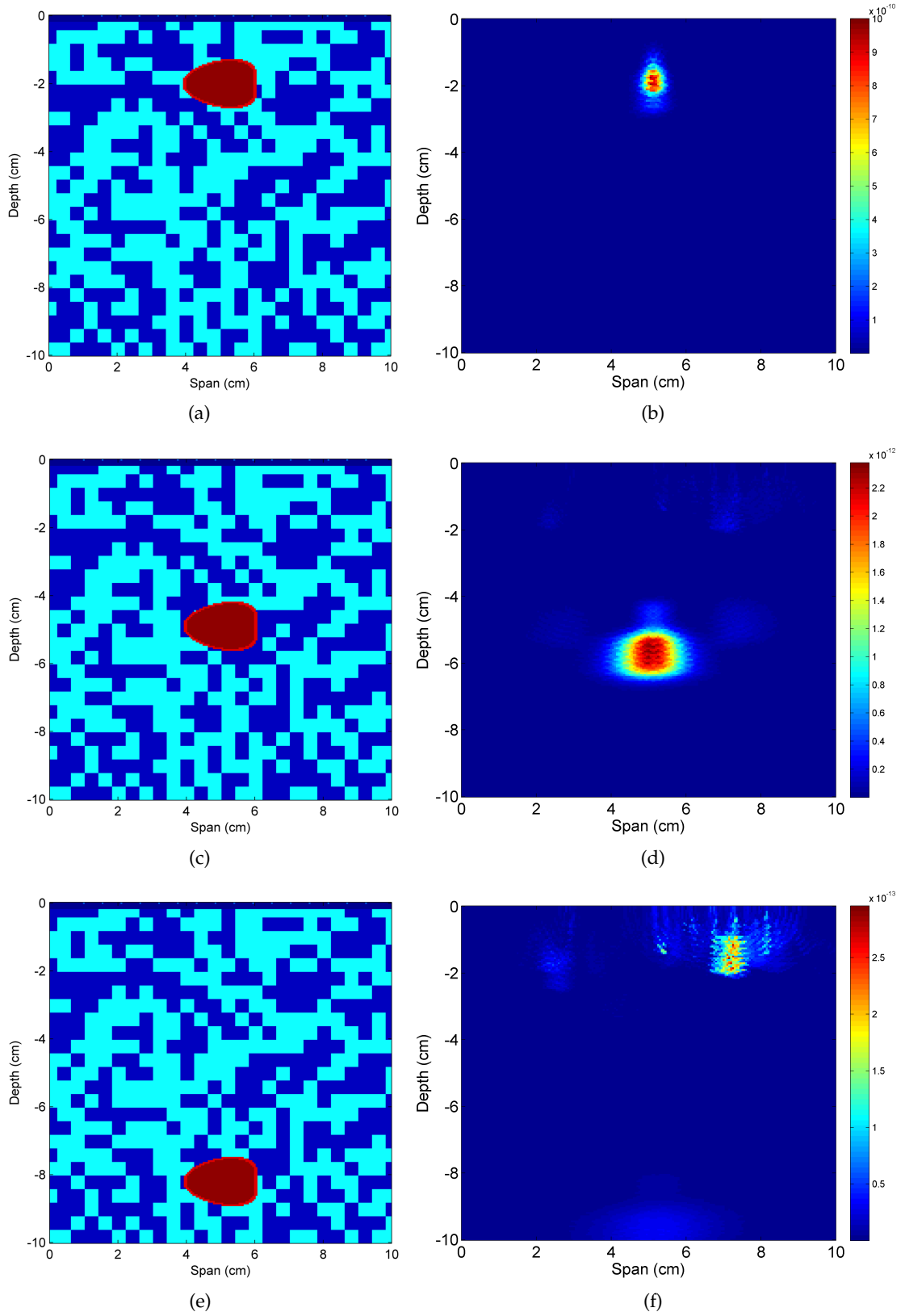


Figure 4.5: Image formation using the Adaptive Filtering artefact removal and the DMAS beamformer for a lymph node located at different depths. (a), (c), (e) FDTD models of the underarm with a lymph node at 2.0 cm, 4.9 cm and 8.2 cm, respectively. (b), (d), (f) Resulting images of backscattered energy.

distance of the tumour from the skin increases. In fact, as the depth increases, the values for FWHM and the L_{error} also increase (showing poorer localisation performance), whereas SCR and SMR noticeably decrease (demonstrating lower contrast between the lymph node response and the background clutter). The reason for this behaviour is that when the average propagation distance between tumour position and the antennas increases, the attenuation encountered by the microwave signals also increases, resulting in attenuated reflections from the metastasised lymph node. The strong reflections near the skin in Figures 4.5 (d) and (f) result from the higher heterogeneity the signals encounter when the lymph node is deeper (note the different scales between the backscattered images). The remaining selected beamforming algorithms (DAS, Channel-Ranked DAS and Channel-Ranked DMAS) yielded the same trends in terms of these metrics for both artefact removals, but revealed poorer performance.

4.2.3 Effects of Increasing Tumour Size

As noted in Chapter 2, lymph nodes can range in size from 1 to 25 mm long. Therefore, this section considers five different test scenarios where a metastasised lymph node positioned at (-2.0, 5.0) cm varied in size from 5 to 25 mm, in steps of 5 mm. The recorded L_{error} and SMR for all the beamformers using Adaptive Filtering are shown in Figure 4.6.

Both the SMR and SCR increase with increasing tumour size. Even for the smallest tumour size (5 mm), there still exists a significant contrast between the tumour and the background clutter, with a SMR as high as 25.43 dB. Again, the different metrics plotted in Figure 4.6 indicate that the DMAS and Channel-Ranked DMAS beamformers significantly outperform the DAS and Channel-Ranked DAS beamformers for all tumour sizes, as observed by higher values for SMR, and lower values for L_{error} . However, it should be noted that for smaller tumours, the Channel-Ranked DAS outperform DAS and the

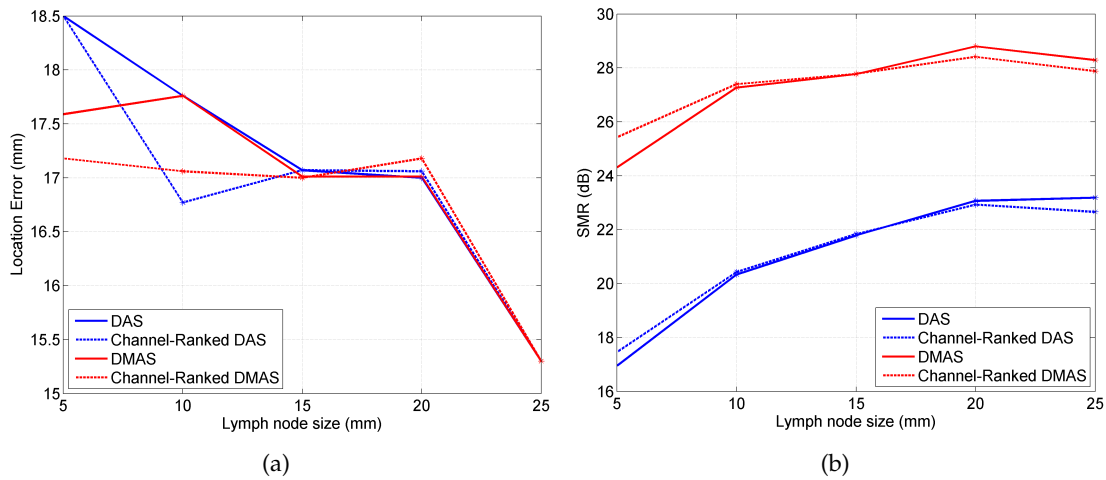


Figure 4.6: Variation of (a) L_{error} and (b) SMR with tumour size for all beamformers using the Adaptive Filtering artefact removal.

Channel-Ranked DMAS outperform DMAS. This is due to the fact that for the smaller tumour the dielectric heterogeneity masks the tumour response, which provides a much more difficult imaging scenario. As Channel-Ranked beamformers reward the channels with shorter propagation distance, which typically encounter a lower extent of dielectric heterogeneous tissue, they tend to add the signals more coherently at the tumour site, providing an improved image of smaller tumours.

4.3 Heterogeneous FDTD Model

In this Section, the FDTD model of the underarm region not only accounts for 10% variance of the dielectric properties of the tissue surrounding lymph nodes, but also contains a healthy and a metastasised lymph node, both located 2.0 cm under the skin. Two different scenarios are considered: firstly, both metastasised and healthy lymph nodes have the same size (15 mm), and secondly the diseased lymph node is bigger than the healthy lymph node (22 mm and 15 mm, respectively). Table 4.3 comprises the metric results and the resulting backscattered images are displayed in Figure 4.7. By visual inspection, it is possible to distinguish the two lymph nodes 18 mm apart (measured from their surfaces) in both scenarios. However, their classification into healthy or diseased can only be conclusive if they differ in size. This is indicated by the metric MMR which is negative if the size of the lymph nodes is the same and positive if different. This is due to the fact that the two categories of lymph nodes do not differ sufficiently in their dielectric properties. This would not be a problem in a real exam since a lymph node tends to swell when it is infiltrated with metastases brought by the lymph from the primary cancer in the breast. By examining the other metric results, it is observed that the most effective beamformer is the Channel-Ranked DMAS as it offers improvements in SMR, MMR and FWHM metrics compared to the other tested beamformers.

Table 4.3: Performance metric results of the selected artefact removals and beamformers for heterogeneous FDTD models of the axilla with two lymph nodes (a healthy and a metastasised one). It compares two scenarios: one with lymph nodes of the same size, and another one with the metastasised lymph node larger than the healthy lymph node.

		DAS	DMAS	Channel-Ranked DAS	Channel-Ranked DMAS
Same Size	SCR (dB)	3.01	1.83	3.04	2.30
	SMR (dB)	19.17	25.45	18.57	24.89
	MMR (dB)	-0.39	-1.08	-0.30	-0.96
	FWHM (mm)	8.50	5.50	8.50	6.25
Different Size	SCR (dB)	3.01	3.02	3.01	3.01
	SMR (dB)	21.60	26.87	21.53	27.17
	MMR (dB)	2.92	5.01	3.87	6.88
	FWHM (mm)	8.75	5.00	8.50	5.00

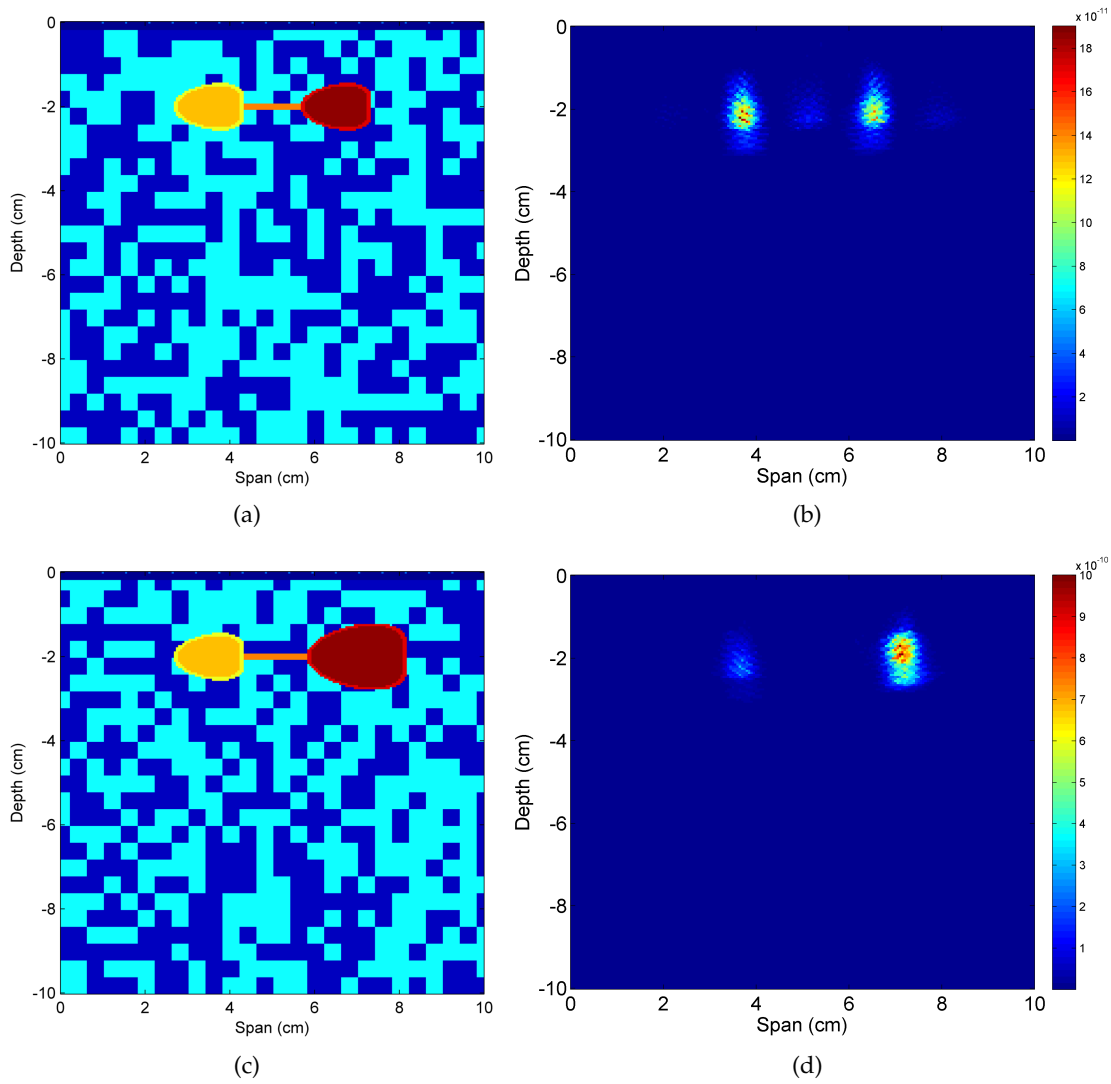


Figure 4.7: Image formation using Adaptive Filtering and Channel-Ranked DMAS. (a) Numerical phantom with two lymph nodes (15 mm long) and (b) resulting image of backscattered energy. (c) Numerical phantom with one healthy lymph node (15 mm long) and a metastasised lymph node (22 mm long) and (d) resulting image of backscattered energy.

4.3.1 Resolution of the System

The resolution of the system, defined as the ability to differentiate between two adjacent scatterers within the axilla, was also tested in a scenario with two lymph nodes with the size of 15 mm. The resolution revealed to be higher when using the Adaptive Filtering artefact removal and the Channel-Ranked DMAS beamformer, the system was able to distinguish between two lymph nodes up to 3 mm apart (minimum distance between their surface) with an energy contrast of 1.46 dB. For these algorithms, the distance between the two peaks of backscattered image is estimated at 2.2 cm while the actual distance between the centre of the lymph nodes is 2.0 cm (presenting an error of 9%). As

for the remaining selected beamformers, they also allowed distinguishing between the lymph nodes with similar localisation error, but with lower contrast in the energy of the peaks.

4.4 Heterogeneous FDTD Model With Muscle

A 2.5 cm muscle layer, which is 3.7 cm deep, is added to the heterogeneous model (with $\pm 10\%$ variance), parallel to the skin. Level I lymph nodes are represented by the lymph nodes located at a depth of 2.0 cm, and level II lymph nodes at 3.7 cm (at the surface of the muscle), or 4.9 cm (inside the muscle). Level III lymph nodes, which would be located further under the muscle layer, are not considered. As shown in Section 4.2, deep tumours cannot be easily detected and, in this scenario, tissues that are located under the muscle are not detected with the algorithms implemented in this dissertation. In a real scenario this is not a significant issue since breast cancer metastasise usually spreads to level I nodes first, following anatomic order, being uncommon the presence of metastasis in level III nodes unless nodes of levels I and II nodes have already been affected. For all these tests, the metrics were again recorded and the most relevant ones are displayed in Table 4.4. The backscattered images using Adaptive Filtering and Channel-Ranked DMAS are shown in Figure 4.8.

The introduction of the muscle layer does not change the MMR, but influences both the SCR and SMR as the contrast between the metastasised lymph node and the surrounding tissue is lower. This is even more significant for the DAS algorithm which yielded 21.60 in terms of SMR in the phantom without muscle (Table 4.3), and 20.86 in the phantom with muscle (Table 4.4), which represents a decay of 0.74 dB in SMR. As for the ability to precisely locate the tumour, the L_{error} is exactly the same in both scenarios (4.61 mm).

Table 4.4: Relevant performance metric results of the selected artefact removals and beamformers for heterogeneous FDTD models of the axilla with muscle and two lymph nodes (a healthy and a metastasised one). It compares lymph nodes in two different levels: level I and level II.

		DAS	DMAS	Channel-Ranked DAS	Channel-Ranked DMAS
Level I	SCR (dB)	3.00	3.02	3.04	3.02
	SMR (dB)	20.86	26.58	21.10	27.11
	MMR (dB)	2.90	4.96	3.90	6.89
	FWHM (mm)	8.75	4.50	9.00	5.50
Level II	SCR (dB)	3.01	3.02	3.01	3.01
	SMR (dB)	16.93	23.87	16.23	23.37
	MMR (dB)	1.92	4.11	2.52	5.37
	FWHM (mm)	11.50	9.00	12.00	8.50

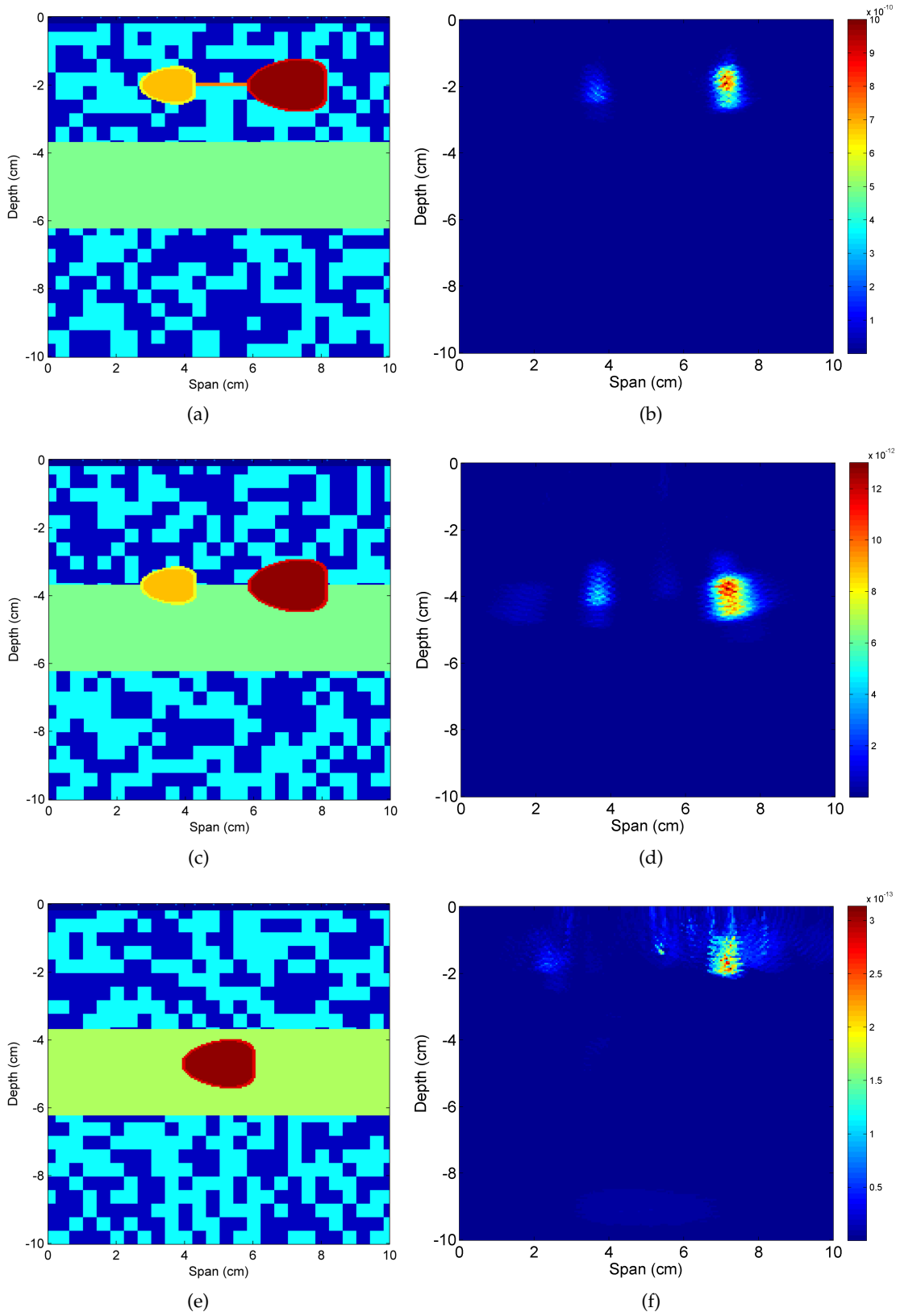


Figure 4.8: Image formation using Adaptive Filtering and Channel-Ranked DMAS for two adjacent lymph nodes in several levels, according to their position to the muscle. (a), (c), (e) FDTD models of the underarm with metastasised lymph nodes at level I, level II in the surface of the muscle and level II inside the muscle, respectively. (b), (d), (f) Resulting images of backscattered energy.

Level II lymph nodes are also distinguishable when located at the surface of the muscle (Figure 4.8 (d)), although in this case lower values of SCR, SMR and MMR are observed for all the beamformers, when comparing to the values obtained for the phantom with only level I lymph nodes. If level II lymph nodes are inside the muscle (Figure 4.8 (f)), it is not possible to distinguish a clear energy peak of the lymph node using any of the implemented beamformers. This is due to the fact that the dielectric properties of metastasised lymph nodes do not differ significantly from those of the muscle, as presented in Table 3.1.

4.5 Other Heterogeneous FDTD Models

Besides the imaging scenarios presented in the above paragraphs, the selected artefact removal and beamforming algorithms were tested in several other FDTD models of the axilla. Some of the most significant findings are given in Figure 4.9, which presents the backscattered images created by using the Adaptive Filtering artefact removal and the DMAS beamformer — the combination of algorithms that yielded better results in the previous Sections.

Figure 4.9 (b), shows that when two lymph nodes are not centred around the antennas (as in Figure 4.8 (b)) the lymph node closest to the centre has the strongest peak response (in Figure 4.8 (b) the responses are identical in both lymph nodes). The reason for that is the higher number of antennas that record the response of that lymph node, when compared with the rightmost lymph node. This means that, when the beamformer adds the backscattered signals, the response from the lymph node closest to the centre will be higher due to the higher number of signals with a stronger response. This could be overcome by increasing the span of the array of antennas so that the number of antennas near each node is similar.

Figure 4.9 (d) shows that, if two lymph nodes are in different levels, the response of the lymph node closer to the skin is higher than the response from the deeper lymph node (in the scenario illustrated in this figure, the contrast between the two energy peaks is 46.73 dB). This is because, as explained in Section 4.2, the deeper the tumour, the more attenuated is the response.

Finally, Figure 4.9 (f) shows that, if one lymph node is on top of another one, only the lymph node closer to the skin can be detected. Its response almost completely masks the response from the deeper lymph node. This is a side-effect caused by the use of the planar configuration.

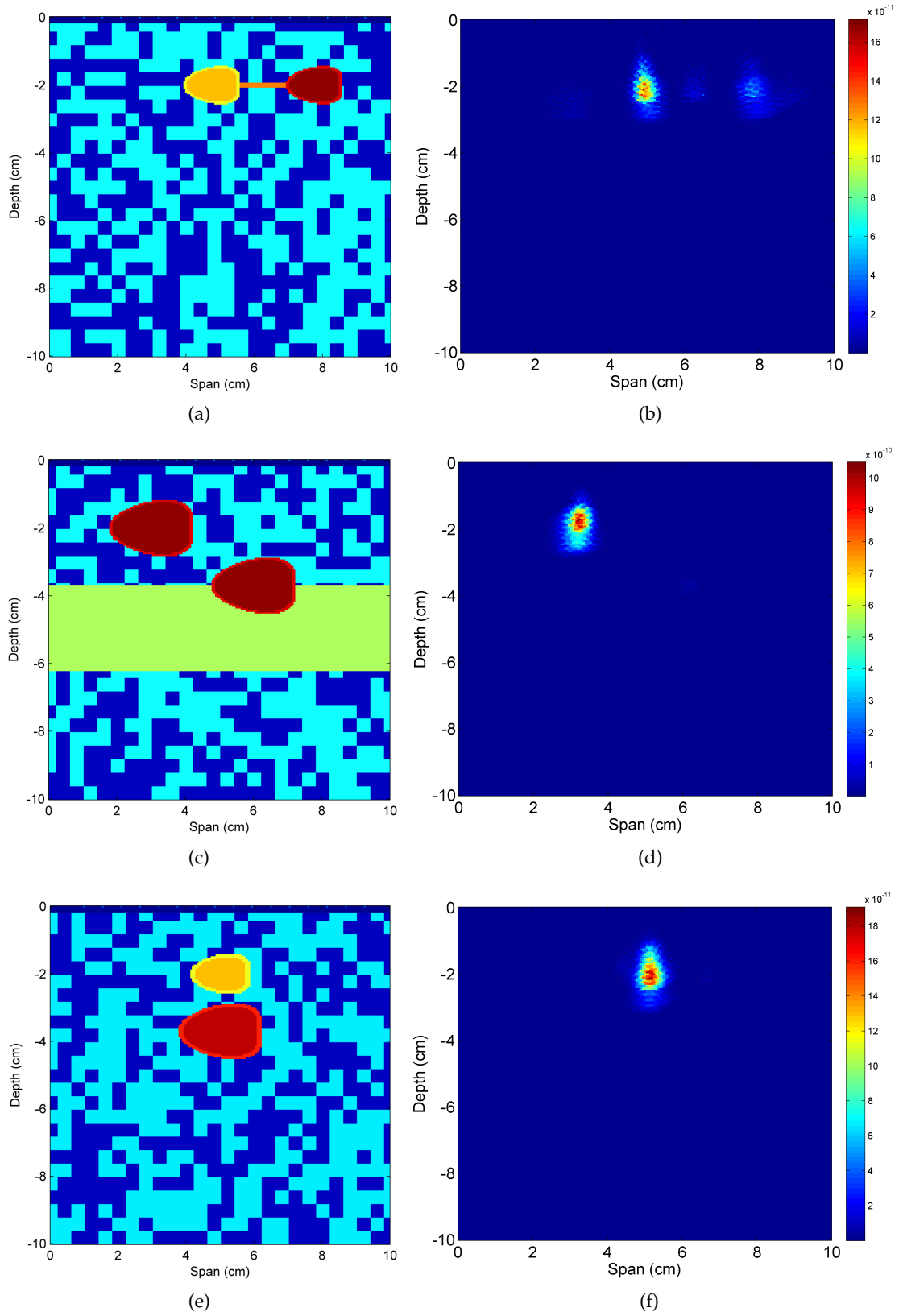


Figure 4.9: Image formation using Adaptive Filtering and Channel-Ranked DMAS for several heterogeneous FDTD models with two lymph nodes. (a), (c), (e) FDTD models of the underarm representing several phantoms. (b), (d), (f) Resulting images of backscattered energy.



Conclusion

5.1 Main Conclusions

This dissertation examined a number of microwave signal processing techniques to image and determine the presence of metastasised lymph nodes within the axillary region in order to aid the detection and staging of breast cancer. This was essentially motivated by the fact that in about 80% of detected breast cancer cases, cancer cells metastasise into the axillary lymph nodes and the existing imaging techniques for axillary lymph node detection and evaluation have not yet yielded satisfactory sensitivity or specificity.

Several 2D heterogeneous models of the axilla were developed to comprehensively evaluate the performance of each image formation algorithm. The phantoms were created with different levels of heterogeneity and with tumours of different sizes and at various locations (including different anatomical levels). Two artefact removal algorithms and four data independent beamforming algorithms were implemented and then compared through five metrics: SCR, SMR, MMR, FWHM and L_{error} . Among the tested beamformer algorithms, three were already described in the literature (DAS, DMAS and Channel-Ranked DAS), but a new approach was proposed in this dissertation for imaging of dielectrically heterogeneous tissues. This approach is called Channel-Ranked DMAS and includes a pairing multiplication procedure after time shifting which gives extra weighting to channels with shorter propagation distances.

Each one of the tested algorithms effectively imaged metastasised lymph nodes when the axilla was composed of dielectrically heterogeneous adipose tissue. Overall, it was observed that Adaptive Filtering is the artefact removal algorithm that better reduced the early-time response of the skin from the backscattered signals. Moreover, the DMAS and

the proposed Channel-Ranked DMAS were found to outperform the selected beamformers across the range of metrics in every tested scenario — different phantoms.

With the different underarm model scenarios, this study demonstrated that the quantitative metrics and visual quality of the resultant UWB axilla profiles worsened with:

- **Increasing the depth of lymph nodes.** As the depth increased, the attenuation encountered by the microwave signals also increased.
- **Increasing dielectric variability within tissue surrounding lymph nodes.** The implemented data-independent beamformers assumed a homogeneous model (or with little variability), so the variant wave velocity in the actual heterogeneous model degraded metric values.
- **Decreasing the size of lymph nodes.** Although a tumour as small as 5 mm was successfully imaged, multiple high energy regions were visible in the resultant backscattered images. For smaller tumours, the proposed Channel-Ranked DMAS performed better than the other beamformers, because when imaging smaller tumours, the dielectric heterogeneity is more noticeable and this beamformer rewards the channels that typically encounter a lower extent of dielectric heterogeneous tissue.

Additionally, it was also observed that it was possible to distinguish between a healthy and a metastasised lymph node when they had different sizes (metastasised lymph nodes tend to grow larger than healthy lymph nodes), as they may not significantly differ in their dielectric properties. When a metastasised lymph node was bigger when compared to a healthy lymph node, they were better differentiated when using the newly proposed Channel-Ranked DMAS. It was also observed that level II lymph nodes are only detected when located at the surface of the muscle since the muscle has dielectric properties similar to those of the lymph nodes.

5.2 Limitations and Future Work

Despite the superior performance of the DMAS and the Channel-Ranked DMAS algorithms, multiple high energy regions (that do not represent the lymph nodes) are present within resultant backscattered images, which can lead to a false negative or false positive diagnosis (if they mask the metastasised lymph node response or if they have a similar response to the metastasised lymph nodes, respectively). This is mainly because, as previously stated, all data-independent beamformers assume that signals are propagating through a homogeneous medium. The inaccuracies between this assumption and the actual heterogeneous medium affect the performance of the beamformers. This prompts the development of novel and more sophisticated imaging algorithms that are able to compensate for the unknown dielectric heterogeneous tissue composition of the

underarm. Data adaptive beamformers may be a solution to compensate for inhomogeneities as they attenuate the effects of clutter by minimizing the overall signal power while maintaining the response from a desired direction. Another solution is to incorporate methods into future beamformers, as those developed by Winters *et al.* [141] for breast, which estimate the average dielectric properties of the patient's underarm tissue. Multistatic imaging algorithms may also be used as they have previously been shown to outperform those used for monostatic systems due to the extra recorded signals and spatial diversity which might improve the localisation of tumours. The artefact removal algorithms could also be improved, for instance, using the Hybrid Artefact Removal algorithm proposed by Elahi *et al.* [123] as it combines the best attributes of the Adaptive Filtering with the Entropy Based Time Window.

The lack of information related to the dielectric properties of the lymph nodes is another important current limitation. Extensive studies regarding this matter must be completed and these should include a high number of tissue samples in order to further understand the differences in electrical properties of diseased and healthy lymph nodes and thus, further study the impact of microwave imaging to aid breast cancer diagnose. If the dielectric differences between healthy and diseased lymph nodes prove to be insufficiently high to clearly distinguish these two categories of lymph nodes, the incorporation of contrast agents that enhance the dielectric contrast in the regions of interest could be studied so that tumours can be identified more easily.

Future work should also involve the development of FDTD underarm models with a semi-curved tissue distribution, which should also include other tissues such as rib cage and lung. The extension of numerical phantoms to three dimensions should also be studied, as well as the investigation of classification methods to differentiate between normal and malignant tissue.

As soon as more realistic simulations are validated, and prior to the application of any beamforming algorithms in a clinical environment, the algorithms must be tested with experimental UWB signals acquired from anatomically realistic anthropomorphic phantoms of the underarm region. A prototype for lymph node examination should then be built having into consideration several aspects, such as the choice of a coupling

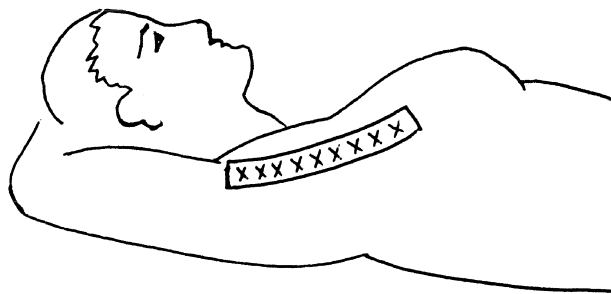


Figure 5.1: Illustration of a possible antenna configuration to be used in an examination of the underarm to image axillary lymph nodes.

medium for the gap between axilla and the antennas and the development and design of a suitable UWB antenna for imaging the underarm. The antenna configuration also has to be accounted for and a possible solution, represented in Figure 5.1, is to have the patient with her arm placed along her head, and place a flexible array of antennas directly on the skin.

To conclude, the results presented in this dissertation are promising and show the feasibility of this novel approach to image the underarm region. Microwaves still have to hardly compete with already well-established imaging modalities, such as Ultrasound and MRI, but certainly Microwave Imaging can provide significant advantages compared to these existing modalities as it offers good resolution, non-ionizing radiation and is potentially low-cost.

5.3 Contributions

The contributions of this dissertation are briefly summarised in this Section:

- Development of a Graphic User Interface in MATLAB, called LN VISUALISER, to assist in applying the image formation algorithms to the computed backscattered signals and in calculating the performance metrics for each image. The Quick Guide for this interface can be found in Appendix A.
- Presentation at the 1st meeting of the COST Action TD1301 (Accelerating the Technological, Clinical and Commercialisation Progress in the Area of Medical Microwave Imaging), held in Lisbon from the 31st March 2014 until the 1st April 2014.
- Poster presentation in the 6th Workshop on Biomedical Engineering, held in Lisbon on the 5th April 2014. The presented poster can be found in Appendix B.
- Oral presentation at a special session in the 2014 IEEE International Symposium on Antennas and Propagation and USNC-URSI Radio Science Meeting, held from the 6th to 12th July 2014, in Memphis, Tennessee, USA. The abstract submitted and approved for oral presentation can be found in Appendix C.
- Participation in the 5th edition of the Fraunhofer Portugal Challenge 2014 (results pending).
- Participation in the prize ANACOM - URSI Portugal (results pending).
- The work presented in this dissertation will be submitted in a high impact factor journal, possibly an IEEE journal or Medical Physics.

Bibliography

- [1] J. Ferlay, I. Soerjomataram, M. Ervik, R. Dikshit, S. Eser, C. Mathers, M. Rebelo, D. Parkin, D. Forman, and F. Bray. *GLOBOCAN 2012 v1.0, Cancer Incidence and Mortality Worldwide: IARC CancerBase No. 11 [Internet]*. Available from [http : // globocan . iarc . fr](http://globocan.iarc.fr) [accessed on 06/01/2014]. Lyon, France: International Agency for Research on Cancer, 2013.
- [2] J. Ferlay, E. Steliarova-Foucher, J. Lortet-Tieulent, S. Rosso, J. Coebergh, H. Comber, D. Forman, and F. Bray. "Cancer Incidence and Mortality Patterns in Europe: Estimates for 40 Countries in 2012". In: *European Journal of Cancer* 49.6 (2013), pp. 1374–1403.
- [3] E. Steliarova-Foucher, M. O’Callaghan, J. Ferlay, E. Masuyer, D. Forman, H. Comber, and F. Bray. *European Cancer Observatory: Cancer Incidence, Mortality, Prevalence and Survival in Europe. Version 1.0*. Available from [http : // eco . iarc . fr](http://eco.iarc.fr) [accessed on 07/01/2014]. European Network of Cancer Registries, International Agency for Research on Cancer, 2012.
- [4] *Mortality database*. Available from [http : // www - dep . iarc . fr / WHObd / WHObd . htm](http://www-dep.iarc.fr/WHObd/WHObd.htm) [accessed on 07/01/2014]. World Health Organization, International Agency for Research on Cancer, 2012.
- [5] S. J. Nass, I. C. Henderson, and J. C. Lashof. *Mammography and Beyond: Developing Technologies for the Early Detection of Breast Cancer*. Ed. by D. o. E. National Cancer Policy Board Institute of Medicine and N. R. C. Life Studies. The National Academies Press, 2001.
- [6] R. G. Dumitrescu and I. Cotarla. "Understanding Breast Cancer Risk - Where Do We Stand in 2005?" In: *Journal of Cellular and Molecular Medicine* 9.1 (2005), pp. 208–221.
- [7] E. Steliarova-Foucher, M. O’Callaghan, J. Ferlay, E. Masuyer, D. Forman, H. Comber, and F. Bray. *What Are the Risk Factors for Breast Cancer?* Available from [http :](http)

- [// cancer . org / index](http://cancer.org/index) [accessed on 08/01/2014]. American Cancer Society, 2013.
- [8] B. S. Hulka and P. G. Moorman. "Breast Cancer: Hormones and Other Risk Factors". In: *Maturitas* 38.1 (2001), pp. 103–113.
- [9] K. Singletary and S. Gapstur. "Alcohol and Breast Cancer: Review of Epidemiologic and Experimental Evidence and Potential Mechanisms". In: *JAMA* 286.17 (2001), pp. 2143–2151.
- [10] P. H. Lahmann et al. "Body Size and Breast Cancer Risk: Findings from the European Prospective Investigation into Cancer and Nutrition (EPIC)". In: *International Journal of Cancer* 111.5 (2004), pp. 762–771.
- [11] W. Zheng, D. R. Gustafson, D. Moore, C.-P. Hong, K. E. Anderson, L. H. Kushi, T. A. Sellers, A. R. Folsom, R. Sinha, and J. R. Cerhan. "Well-Done Meat Intake and the Risk of Breast Cancer". In: *Journal of the National Cancer Institute* 90.22 (1998), pp. 1724–1729.
- [12] E. Velie, M. Kulldorff, C. Schairer, G. Block, D. Albanes, and A. Schatzkin. "Dietary Fat, Fat Subtypes, and Breast Cancer in Postmenopausal Women: a Prospective Cohort Study". In: *Journal of the National Cancer Institute* 92.10 (2000), pp. 833–839.
- [13] M. A. V. Duyn and E. Pivonka. "Overview of the Health Benefits of Fruit and Vegetable Consumption for the Dietetics Professional: Selected Literature". In: *Journal of the American Dietetic Association* 100.12 (2000), pp. 1511–1521.
- [14] J. L. Kelsey, M. D. Gammon, and E. M. John. "Reproductive Factors and Breast Cancer". In: *Epidemiologic Reviews* 15.1 (1993), pp. 36–47.
- [15] "Familial Breast Cancer: Collaborative Reanalysis of Individual Data from 52 Epidemiological Studies Including 58209 Women with Breast Cancer and 101986 Women Without the Disease". In: *The Lancet* 358.9291 (2001), pp. 1389–1399.
- [16] N. Biglia, E. Defabiani, R. Ponzzone, L. Mariani, D. Marengo, and P. Sismondi. "Management of Risk of Breast Carcinoma in Postmenopausal Women." In: *Endocrine-related cancer* 11.1 (2004), pp. 69–83.
- [17] C. Héry, J. Ferlay, M. Boniol, and P. Autier. "Quantification of Changes in Breast Cancer Incidence and Mortality since 1990 in 35 Countries with Caucasian-Majority Populations". In: *Annals of Oncology* 19.6 (2008), pp. 1187–1194.
- [18] P. Huynh, A. Jarolimek, and S. Daye. "The false-negative mammogram." In: *RadioGraphics* 18.5 (1998), pp. 1137–1154.
- [19] V. Jackson, R. Hendrick, S. Feig, and D. Kopans. "Imaging of the Radiographically Dense Breast." In: *Radiology* 188.2 (1993), pp. 297–301.
- [20] J. G. Elmore, M. B. Barton, V. M. Moceris, S. Polk, P. J. Arena, and S. W. Fletcher. "Ten-Year Risk of False Positive Screening Mammograms and Clinical Breast Examinations". In: *New England Journal of Medicine* 338.16 (1998), pp. 1089–1096.

- [21] M. B. Mainiero, A. Lourenco, M. C. Mahoney, M. S. Newell, L. Bailey, L. D. Barke, C. D'Orsi, J. A. Harvey, M. K. Hayes, P. T. Huynh, P. M. Jokich, S.-J. Lee, C. D. Lehman, D. A. Mankoff, J. A. Nepute, S. B. Patel, H. E. Reynolds, M. L. Sutherland, and B. G. Haffty. "{ACR} Appropriateness Criteria Breast Cancer Screening". In: *Journal of the American College of Radiology* 10.1 (2013), pp. 11–14.
- [22] *ACR Practice Guideline for the Performance of a Breast Ultrasound Examination*. The American College of Radiology, 2011.
- [23] C. K. Kuhl, S. Schrading, C. C. Leutner, N. Morakkabati-Spitz, E. Wardelmann, R. Fimmers, W. Kuhn, and H. H. Schild. "Mammography, Breast Ultrasound, and Magnetic Resonance Imaging for Surveillance of Women at High Familial Risk for Breast Cancer". In: *Journal of Clinical Oncology* 23.33 (2005), pp. 8469–8476.
- [24] M. Walters and L. Nadalo. "MRI Breast Clinical Indications: A Comprehensive Review". In: *Journal of the American Osteopathic College of Radiology* 2.1 (2013), pp. 2–17.
- [25] S. B. Glass and Z. A. Shah. "Clinical Utility of Positron Emission Mammography". In: *Proceedings (Baylor University Medical Center)* 26.3 (2013), p. 314.
- [26] B. Ebert and D. Grosenick. "Optical Imaging of Breast Tumors and of Gastrointestinal Cancer by Laser-Induced Fluorescence". In: *Molecular Imaging in Oncology*. Ed. by O. Schober and B. Riemann. Vol. 187. Recent Results in Cancer Research. Springer Berlin Heidelberg, 2013, pp. 331–350.
- [27] R. E. Hendrick. "Radiation Doses and Cancer Risks from Breast Imaging Studies". In: *Radiology* 257.1 (2010), pp. 246–253.
- [28] W. T. Joines, Y. Zhang, C. Li, and R. L. Jirtle. "The Measured Electrical Properties of Normal and Malignant Human Tissues from 50 to 900 MHz". In: *Medical Physics* 21.4 (1994), pp. 547–550.
- [29] A. Surowiec, S. Stuchly, J. Barr, and A. Swarup. "Dielectric Properties of Breast Carcinoma and the Surrounding Tissues". In: *Biomedical Engineering, IEEE Transactions on* 35.4 (1988), pp. 257–263.
- [30] F. Macdonald, C. Ford, and A. Casson. *Molecular Biology of Cancer*. Advanced Texts. Taylor & Francis, 2004.
- [31] I.-C. Kiricuta and V. Simplăceanu. "Tissue Water Content and Nuclear Magnetic Resonance in Normal and Tumor Tissues". In: *Cancer Research* 35.5 (1975), pp. 1164–1167.
- [32] M. Lazebnik, D. Popovic, L. McCartney, et al. "A Large-Scale Study of the Ultrawideband Microwave Dielectric Properties of Normal, Benign and Malignant Breast Tissues Obtained from Cancer Surgeries". In: *Physics in Medicine and Biology* 52.20 (2007), p. 6093.

- [33] N. Nikolova. "Microwave Imaging for Breast Cancer". In: *Microwave Magazine, IEEE* 12.7 (2011), pp. 78–94.
- [34] R. C. Conceicao, M. O'Halloran, M. Glavin, and E. Jones. "Comparison of Planar and Circular Antenna Configurations for Breast Cancer Detection Using Microwave Imaging". In: *Progress In Electromagnetics Research* 99 (2009), pp. 1–20.
- [35] A. Vander Vorst, A. Rosen, and Y. Kotsuka. *RF/Microwave Interaction with Biological Tissues*. Wiley Series in Microwave and Optical Engineering. Wiley, 2006.
- [36] A. Santorelli, M. Vander Schueren, and M. Popovic. "SAR levels in microwave breast imaging: 3-D safety assessment with plane-wave illumination". In: *Microwave Conference Proceedings (APMC), 2011 Asia-Pacific*. 2011, pp. 481–484.
- [37] E. Fear, X. Li, S. Hagness, and M. Stuchly. "Confocal Microwave Imaging for Breast Cancer Detection: Localization of Tumors in Three Dimensions". In: *Biomedical Engineering, IEEE Transactions on* 49.8 (2002), pp. 812–822.
- [38] X. Li and S. Hagness. "A Confocal Microwave Imaging Algorithm for Breast Cancer Detection". In: *Microwave and Wireless Components Letters, IEEE* 11.3 (2001), pp. 130–132.
- [39] A. Bulyshev, S. Semenov, A. Souvorov, R. Svenson, A. Nazarov, Y. Sizov, and G. Tatsis. "Computational Modeling of Three-Dimensional Microwave Tomography of Breast Cancer". In: *Biomedical Engineering, IEEE Transactions on* 48.9 (2001), pp. 1053–1056.
- [40] K.-C. Kwon, Y.-T. Lim, C.-H. Kim, N. Kim, C. Park, K.-H. Yoo, S.-H. Son, and S.-I. Jeon. "Microwave Tomography Analysis System for Breast Tumor Detection". In: *Journal of Medical Systems* 36.3 (2012), pp. 1757–1767.
- [41] L. Gharsalli, H. Ayasso, B. Duchêne, A. Mohammad-Djafari, et al. "Microwave Tomography for Breast Cancer Detection Within a Variational Bayesian Approach". In: *IEEE European Signal Processing Conference, EUSIPCO*. 2013.
- [42] P. M. Meaney, M. W. Fanning, T. Raynolds, C. J. Fox, Q. Fang, C. A. Kogel, S. P. Poplack, and K. D. Paulsen. "Initial Clinical Experience with Microwave Breast Imaging in Women with Normal Mammography". In: *Academic Radiology* 14.2 (2007), pp. 207–218.
- [43] P. Meaney, M. Fanning, D. Li, S. P. Poplack, and K. Paulsen. "A Clinical Prototype for Active Microwave Imaging of the Breast". In: *Microwave Theory and Techniques, IEEE Transactions on* 48.11 (2000), pp. 1841–1853.
- [44] A. Souvorov, A. Bulyshev, S. Semenov, R. Svenson, and G. Tatsis. "Two-Dimensional Computer Analysis of a Microwave Flat Antenna Array for Breast Cancer Tomography". In: *Microwave Theory and Techniques, IEEE Transactions on* 48.8 (2000), pp. 1413–1415.

- [45] M. O'Halloran, R. C. Conceicao, D. Byrne, M. Glavin, and E. Jones. "FDTD Modeling of the Breast: A Review". In: *Progress In Electromagnetics Research B* 18 (2009), pp. 1–24.
- [46] D. Flores-Tapia, D. Rodriguez Herrera, M. Nepote, A. Maizlish, C. Alabaster, and S. Pistorius. "Holographic Reconstruction of Multistatic Breast Microwave Radar Images: Initial Results on Synthetic Phantoms". In: *Electromagnetics in Advanced Applications (ICEAA), 2013 International Conference on*. 2013, pp. 1103–1106.
- [47] R. K. Amineh, M. Ravan, A. Khalatpour, and N. Nikolova. "Three-Dimensional Near-Field Microwave Holography Using Reflected and Transmitted Signals". In: *Antennas and Propagation, IEEE Transactions on* 59.12 (2011), pp. 4777–4789.
- [48] G. Cheng, Y. Zhu, and J. Grzesik. "Exact Solutions in Microwave Holography Validated by Measurements". In: *Antennas and Propagation (EuCAP), 2013 7th European Conference on*. 2013, pp. 3860–3864.
- [49] M. Ravan, R. K. Amineh, and N. K. Nikolova. "Two-Dimensional Near-Field Microwave Holography". In: *Inverse Problems* 26.5 (2010), p. 055011.
- [50] R. K. Amineh, M. Ravan, A. Khalatpour, and N. Nikolova. "Three-Dimensional Near-Field Microwave Holography Using Reflected and Transmitted Signals". In: *Antennas and Propagation, IEEE Transactions on* 59.12 (2011), pp. 4777–4789.
- [51] Y. Jin, J. Moura, Y. Jiang, M. Wahl, H. Zhu, and Q. He. "Breast Cancer Detection by Time Reversal Imaging". In: *Biomedical Imaging: From Nano to Macro, 2008. ISBI 2008. 5th IEEE International Symposium on*. 2008, pp. 816–819.
- [52] P. Kosmas and C. Rappaport. "Time Reversal with the FDTD Method for Microwave Breast Cancer Detection". In: *Microwave Theory and Techniques, IEEE Transactions on* 53.7 (2005), pp. 2317–2323.
- [53] M. Hossain, A. Mohan, and M. Abedin. "Beamspace Time-Reversal Microwave Imaging for Breast Cancer Detection". In: *Antennas and Wireless Propagation Letters, IEEE* 12 (2013), pp. 241–244.
- [54] X. Zhu, Z. Zhao, J. Wang, J. Song, and Q. H. Liu. "Microwave-Induced Thermal Acoustic Tomography for Breast Tumor Based on Compressive Sensing". In: *Biomedical Engineering, IEEE Transactions on* 60.5 (2013), pp. 1298–1307.
- [55] J. Zhong, F. Yong, and Y. Sihua. "Microwave-Induced Thermoacoustic Imaging for Early Breast Cancer Detection". In: *Journal of Innovative Optical Health Sciences* 06.01 (2013), p. 1350001.
- [56] J. Song, Z. Zhao, J. Wang, X. Zhu, J. Wu, Z.-P. Nie, and Q. H. Liu. "An Integrated Simulation Approach and Experimental Research on Microwave Induced Thermo-Acoustic Tomography System". In: *Progress In Electromagnetics Research* 140 (2013), pp. 385–400.

- [57] Z. Zhao, J. Song, X. Zhu, J. Wang, J. Wu, Y. Liu, Z.-P. Nie, and Q. H. Liu. "System Development of Microwave Induced Thermo-Acoustic Tomography and Experiments on Breast Tumor". In: *Progress In Electromagnetics Research* 134 (2013), pp. 323–336.
- [58] A. Abbosh and S. Crozier. "Strain Imaging of the Breast by Compression Microwave Imaging". In: *Antennas and Wireless Propagation Letters, IEEE* 9 (2010), pp. 1229–1232.
- [59] V. Rajagopal, P. M. F. Nielsen, and M. P. Nash. "Modeling Breast Biomechanics for Multi-Modal Image Analysis—Successes and Challenges". In: *Wiley Interdisciplinary Reviews: Systems Biology and Medicine* 2.3 (2010), pp. 293–304.
- [60] N. Patani, M. Dwek, and M. Douek. "Predictors of Axillary Lymph Node Metastasis in Breast Cancer: A Systematic Review". In: *European Journal of Surgical Oncology (EJSO)* 33.4 (2007), pp. 409–419.
- [61] T. Cameron, M. Okoniewski, E. Fear, D. Mew, B. Banks, and T. Ogilvie. "A Preliminary Study of the Electrical Properties of Healthy and Diseased Lymph Nodes". In: *Antenna Technology and Applied Electromagnetics the American Electromagnetics Conference (ANTEM-AMEREM), 2010 14th International Symposium on*. 2010, pp. 1–3.
- [62] E. Livingston. "Breast Cancer and Axillary Lymph Nodes". In: *JAMA* 310.14 (2013), p. 1518.
- [63] U. Veronesi, G. Paganelli, V. Galimberti, G. Viale, S. Zurrada, M. Bedoni, A. Costa, C. de Cicco, J. G. Geraghty, A. Luini, V. Sacchini, and P. Veronesi. "Sentinel-Node Biopsy to Avoid Axillary Dissection in Breast Cancer with Clinically Negative Lymph-Nodes". In: *The Lancet* 349.9069 (1997), pp. 1864–1867.
- [64] J. Goldberg, L. Wiechmann, E. Riedel, M. Morrow, and K. Van Zee. "Morbidity of Sentinel Node Biopsy in Breast Cancer: The Relationship Between the Number of Excised Lymph Nodes and Lymphedema". In: *Annals of Surgical Oncology* 17.12 (2010), pp. 3278–3286.
- [65] V. M. Moncayo, J. N. Aarsvold, S. F. Grant, S. C. Bartley, and N. P. Alazraki. "Status of Sentinel Lymph Node for Breast Cancer". In: *Seminars in Nuclear Medicine* 43.4 (2013), pp. 281–293.
- [66] C. Delaney. *Netter's Surgical Anatomy and Approaches*. Netter Clinical Science. Elsevier Health Sciences, 2013.
- [67] A. Schauer, W. Becker, and K. Possinger. *The Sentinel Lymph Node Concept*. Springer, 2005.
- [68] C. National Guideline. *Sentinel Lymph Node Biopsy and Axillary Node Dissection in Early Stage Breast Cancer*. Clinical practice guideline; no. BR-004. Rockville MD: Agency for Healthcare Research and Quality (AHRQ), 2012.

- [69] A. E. Giuliano, K. K. Hunt, K. V. Ballman, P. D. Beitsch, P. W. Whitworth, P. W. Blumencranz, A. M. Leitch, S. Saha, L. M. McCall, and M. Morrow. "Axillary Dissection vs No Axillary Dissection in Women With Invasive Breast Cancer and Sentinel Node Metastasis: A Randomized Clinical Trial". In: *JAMA* 305.6 (2011), pp. 569–575.
- [70] S. Harnan, K. Cooper, Y. Meng, S. Ward, P. Fitzgerald, D. Papaioannou, C. Ingram, E. Lorenz, I. Wilkinson, and L. Wyld. "Magnetic Resonance for Assessment of Axillary Lymph Node Status in Early Breast Cancer: A Systematic Review and Meta-Analysis". In: *European Journal of Surgical Oncology (EJSO)* 37.11 (2011), pp. 928–936.
- [71] H. Rahbar, S. C. Partridge, S. H. Javid, and C. D. Lehman. "Imaging Axillary Lymph Nodes in Patients with Newly Diagnosed Breast Cancer". In: *Current Problems in Diagnostic Radiology* 41.5 (2012), pp. 149–158.
- [72] M. B. Mainiero. "Regional Lymph Node Staging in Breast Cancer: The Increasing Role of Imaging and Ultrasound-Guided Axillary Lymph Node Fine Needle Aspiration". In: *Radiologic Clinics of North America* 48.5 (2010), pp. 989–997.
- [73] M. B. Mainiero, C. M. Cinelli, S. L. Koelliker, T. A. Graves, and M. A. Chung. "Axillary Ultrasound and Fine-Needle Aspiration in the Preoperative Evaluation of the Breast Cancer Patient: An Algorithm Based on Tumor Size and Lymph Node Appearance". In: *American Journal of Roentgenology* 195.5 (2010), pp. 1261–1267.
- [74] N. Houssami, S. Ciatto, R. Turner, H. Cody, and P. Macaskill. "Preoperative Ultrasound-Guided Needle Biopsy of Axillary Nodes in Invasive Breast Cancer: Meta-Analysis of Its Accuracy and Utility in Staging the Axilla". In: *Annals of Surgery* 254.2 (2011), pp. 243–251.
- [75] E. Deurloo, P. Tanis, K. Gilhuijs, S. Muller, R. Kröger, J. Peterse, E. Rutgers, R. V. Olmos, and L. S. Kool. "Reduction in the Number of Sentinel Lymph Node Procedures by Preoperative Ultrasonography of the Axilla in Breast Cancer". In: *European Journal of Cancer* 39.8 (2003), pp. 1068–1073.
- [76] R. Schipper, L. van Roozendaal, B. de Vries, R. Pijnappel, R. Beets-Tan, M. Lobbes, and M. Smidt. "Axillary Ultrasound for Preoperative Nodal Staging in Breast Cancer Patients: Is It of Added Value?" In: *The Breast* 22.6 (2013), pp. 1108–1113.
- [77] Q. Lu, J. Hua, M. M. Kassir, Z. Delproposto, Y. Dai, J. Sun, M. Haacke, and J. Hu. "Imaging Lymphatic System in Breast Cancer Patients with Magnetic Resonance Lymphangiography". In: *PloS one* 8.7 (2013), p. 0069701.
- [78] N. Luo, D. Su, G. Jin, L. Liu, X. Zhu, D. Xie, and Y. Liu. "Apparent Diffusion Coefficient Ratio between Axillary Lymph Node with Primary Tumor to Detect Nodal Metastasis in Breast Cancer Patients". In: *Journal of Magnetic Resonance Imaging* (2013).

- [79] T. Kamitani, M. Hatakenaka, H. Yabuuchi, Y. Matsuo, N. Fujita, M. Jinnouchi, M. Nagao, K. Shirahane, E. Tokunaga, and H. Honda. "Detection of Axillary Node Metastasis Using Diffusion-Weighted {MRI} in Breast Cancer". In: *Clinical Imaging* 37.1 (2013), pp. 56–61.
- [80] D. K. W. Yeung, W.-T. Yang, and G. M. K. Tse. "Breast Cancer: In Vivo Proton MR Spectroscopy in the Characterization of Histopathologic Subtypes and Preliminary Observations in Axillary Node Metastases". In: *Radiology* 225.1 (2002), pp. 190–197.
- [81] B. Koolen, R. Valdés Olmos, P. Elkhuisen, W. Vogel, M.-J. Vrancken Peeters, S. Rodenhuis, and E. Rutgers. "Locoregional Lymph Node Involvement on 18F-FDG PET/CT in Breast Cancer Patients Scheduled for Neoadjuvant Chemotherapy". In: *Breast Cancer Research and Treatment* 135.1 (2012), pp. 231–240.
- [82] N. Avril, J. Dose, F. Jänicke, S. Ziegler, W. Römer, W. Weber, M. Herz, W. Nathrath, H. Graeff, and M. Schwaiger. "Assessment of Axillary Lymph Node Involvement in Breast Cancer Patients With Positron Emission Tomography Using Radiolabeled 2-(Fluorine-18)-fluoro-2-deoxy-D-glucose". In: *Journal of the National Cancer Institute* 88.17 (1996), pp. 1204–1209.
- [83] C. Riegger, A. Koeninger, V. Hartung, F. Otterbach, R. Kimmig, M. Forsting, A. Bockisch, G. Antoch, and T. A. Heusner. "Comparison of the Diagnostic Value of FDG-PET/CT and Axillary Ultrasound for the Detection of Lymph Node Metastases in Breast Cancer Patients". In: *Acta Radiologica* 53.10 (2012), pp. 1092–1098.
- [84] J. Choi, J. Cho, Y. Lee, J. Yim, B. Kang, K. Keun Oh, W. Hee Jung, H. Jung Kim, C. Cheon, H.-D. Lee, and Y. Kwon. "Microwave Detection of Metastasized Breast Cancer Cells in the Lymph Node; Potential Application for Sentinel Lymphadenectomy". In: *Breast Cancer Research and Treatment* 86.2 (2004), pp. 107–115.
- [85] A. Fhager, T. McKelvey, and M. Persson. "Stroke Detection Using a Broadband Microwave Antenna System". In: *Antennas and Propagation (EuCAP), 2010 Proceedings of the Fourth European Conference on*. 2010, pp. 1–3.
- [86] R. Scapaticci, L. Di Donato, I. Catapano, and L. Crocco. "A Feasibility Study on Microwave Imaging for Brain Stroke Monitoring". In: *Progress In Electromagnetics Research B* 40 (2012), pp. 305–324.
- [87] P. M. Meaney, D. Goodwin, A. H. Golnabi, T. Zhou, M. Pallone, S. D. Geimer, G. Burke, and K. D. Paulsen. "Clinical Microwave Tomographic Imaging of the Calcaneus: A First-In-Human Case Study of Two Subjects". In: *Biomedical Engineering, IEEE Transactions on* 59.12 (2012), pp. 3304–3313.
- [88] S. M. Salvador, E. C. Fear, M. Okoniewski, and J. R. Matyas. "Exploring Joint Tissues with Microwave Imaging". In: *Microwave Theory and Techniques, IEEE Transactions on* 58.8 (2010), pp. 2307–2313.

- [89] R. Seeley, P. Tate, and T. Stephens. *Anatomy and Physiology*. 8th. McGraw-Hill Higher Education, 2007.
- [90] J. Hall. *Guyton and Hall Textbook of Medical Physiology: Enhanced E-book*. 11th. Guyton Physiology. Elsevier Health Sciences, 2010.
- [91] P. Tanis, O. Nieweg, R. V. Olmos, and B. Kroon. "Anatomy and Physiology of Lymphatic Drainage of the Breast from the Perspective of Sentinel Node Biopsy". In: *Journal of the American College of Surgeons* 192.3 (2001), pp. 399–409.
- [92] G. C. Bentel, L. B. Marks, P. H. Hardenbergh, and L. R. Prosnitz. "Variability of the Depth of Supraclavicular and Axillary Lymph Nodes in Patients with Breast Cancer: Is a Posterior Axillary Boost Field Necessary?" In: *International Journal of Radiation Oncology* Biology* Physics* 47.3 (2000), pp. 755–758.
- [93] S. G. Komen. *Facts for Life: Axillary Lymph Nodes*. 2012.
- [94] D. Winchester and D. Winchester. *Breast Cancer*. 2nd. American Cancer Society atlas of clinical oncology. B.C. Decker, 2006.
- [95] *Axillary lymph nodes*. Available from <http://www.dreamstime.com> [accessed on 06/03/2014]. Dreamstime.
- [96] R. Hesketh. *Introduction to Cancer Biology*. Introduction to Cancer Biology: A Concise Journey from Epidemiology Through Cell and Molecular Biology to Treatment and Prospects. Cambridge University Press, 2012.
- [97] *Breast Cancer Treatment: Stages of Breast Cancer*. Available from <http://www.cancer.gov/cancertopics/pdq/treatment/breast/Patient/page2> [accessed on 16/01/2014]. National Cancer Institute, 2013.
- [98] L. Chen. *Microwave Electronics: Measurement and Materials characterization*. John Wiley, 2004.
- [99] *Agilent Basics of Measuring the Dielectric Properties of Materials - Application Note*. USA: Agilent Technologies, 2013.
- [100] S. Gabriel, R. W. Lau, and C. Gabriel. "The Dielectric Properties of Biological Tissues: II. Measurements in the Frequency Range 10 Hz to 20 GHz". In: *Physics in Medicine and Biology* 41.11 (1996), p. 2251.
- [101] K. Yee. "Numerical Solution of Initial Boundary Value Problems Involving Maxwell's Equations in Isotropic Media". In: *Antennas and Propagation, IEEE Transactions on* 14.3 (1966), pp. 302–307.
- [102] A. Taflove and S. Hagness. *Computational Electrodynamics: The Finite - Difference Time - Domain Method*. 3rd edition. Antennas and Propagation Library. Artech House, 2005.
- [103] Y. Hao and R. Mittra. *FDTD Modeling of Metamaterials: Theory and Applications: Electromagnetics*. Artech House, 2008.

- [104] D. Sullivan. *Electromagnetic Simulation Using the FDTD Method*. 2nd. Wiley, 2013.
- [105] S. Hagness, A. Taflove, and J. Bridges. "Two-Dimensional FDTD Analysis of a Pulsed Microwave Confocal System for Breast Cancer Detection: Fixed-Focus and Antenna-Array Sensors". In: *Biomedical Engineering, IEEE Transactions on* 45.12 (1998), pp. 1470–1479.
- [106] S. Hagness, A. Taflove, and J. Bridges. "Three-Dimensional FDTD Analysis of a Pulsed Microwave Confocal System for Breast Cancer Detection: Design of an Antenna-Array Element". In: *Antennas and Propagation, IEEE Transactions on* 47.5 (1999), pp. 783–791.
- [107] "The Finite-Difference Time-Domain Method". In: *Computational Electromagnetics*. Vol. 51. Texts in Applied Mathematics. Springer New York, 2005, pp. 57–86.
- [108] S. Gedney. *Introduction to the Finite-Difference Time-Domain (FDTD) Method for Electromagnetics*. Synthesis Lectures on Computational Electromagnetics. Morgan & Claypool Publishers, 2011.
- [109] E. Zastrow, S. Davis, M. Lazebnik, F. Kelcz, B. V. Veen, and S. Hagness. *Database of 3D Grid-Based Numerical Breast Phantoms for use in Computational Electromagnetics Simulations*. Department of Electrical and Computer Engineering — University of Wisconsin-Madison, 2012.
- [110] M. Lazebnik, M. Okoniewski, J. Booske, and S. Hagness. "Highly Accurate Debye Models for Normal and Malignant Breast Tissue Dielectric Properties at Microwave Frequencies". In: *Microwave and Wireless Components Letters, IEEE* 17.12 (2007), pp. 822–824.
- [111] M. A. Eleiwa and A. Z. Elsherbeni. "Debye Constants for Biological Tissues from 30 Hz to 20 GHz". In: *ACES Journal* 16.3 (2001), pp. 202–213.
- [112] S. Hagness, A. Taflove, and J. Bridges. "Two-Dimensional FDTD Analysis of a Pulsed Microwave Confocal System for Breast Cancer Detection: Fixed-Focus and Antenna-Array Sensors". In: *Biomedical Engineering, IEEE Transactions on* 45.12 (1998), pp. 1470–1479.
- [113] E. Fear and M. Stuchly. "Microwave Detection of Breast Cancer". In: *Microwave Theory and Techniques, IEEE Transactions on* 48.11 (2000), pp. 1854–1863.
- [114] M. Elahi, M. Glavin, E. Jones, and M. O'Halloran. "Artifact Removal Algorithms for Microwave Imaging of the Breast". In: *Progress In Electromagnetics Research* 141 (2013).
- [115] H. B. Lim, N. T. T. Nhung, E.-P. Li, and N. D. Thang. "Confocal Microwave Imaging for Breast Cancer Detection: Delay-Multiply-and-Sum Image Reconstruction Algorithm". In: *Biomedical Engineering, IEEE Transactions on* 55.6 (2008), pp. 1697–1704.

- [116] M. Klemm, I. Craddock, J. Leendertz, A. Preece, and R. Benjamin. "Improved Delay-And-Sum Beamforming Algorithm for Breast Cancer Detection". In: *International Journal of Antennas and Propagation* 2008 (2008).
- [117] E. J. Bond, X. Li, S. Hagness, and B. Van Veen. "Microwave Imaging Via Space-Time Beamforming for Early Detection of Breast Cancer". In: *Antennas and Propagation, IEEE Transactions on* 51.8 (2003), pp. 1690–1705.
- [118] M. O'Halloran, E. Jones, and M. Glavin. "Quasi-Multistatic MIST Beamforming for the Early Detection of Breast Cancer". In: *Biomedical Engineering, IEEE Transactions on* 57.4 (2010), pp. 830–840.
- [119] B. Maklad, C. Curtis, E. Fear, and G. Messier. "Neighborhood-Based Algorithm to Facilitate the Reduction of Skin Reflections in Radar-Based Microwave". In: *Progress In Electromagnetics Research B* 39 (2012).
- [120] J. Sill and E. Fear. "Tissue Sensing Adaptive Radar for Breast Cancer Detection - Experimental Investigation of Simple Tumor Models". In: *Microwave Theory and Techniques, IEEE Transactions on* 53.11 (2005), pp. 3312–3319.
- [121] W. Zhi and F. Chin. "Entropy-Based Time Window for Artifact Removal in UWB Imaging of Breast Cancer Detection". In: *Signal Processing Letters, IEEE* 13.10 (2006), pp. 585–588.
- [122] A. Maskooki, E. Gunawan, C. B. Soh, and K. S. Low. "Frequency Domain Skin Artifact Removal Method for Ultra-Wideband Breast Cancer Detection". In: *Progress In Electromagnetics Research* 98 (2009), pp. 299–314.
- [123] M. Elahi, A. Shahzad, M. Glavin, E. Jones, and M. O'Halloran. "Hybrid Artifact Removal for Confocal Microwave Breast Imaging". In: *Antennas and Wireless Propagation Letters, IEEE* 13 (2014), pp. 149–152.
- [124] R. Nilavalan, A. Gbedemah, I. J. Craddock, X. Li, and S. Hagness. "Numerical Investigation of Breast Tumour Detection using Multi-Static Radar". In: *Electronics Letters* 39.25 (2003), pp. 1787–1789.
- [125] M. O'Halloran, M. Glavin, and E. Jones. "Channel-Ranked Beamformer for the Early Detection of Breast Cancer". In: *Progress In Electromagnetics Research* 103 (2010), pp. 153–168.
- [126] S. Davis, E. Bond, S. Hagness, and B. Van Veen. "Microwave Imaging Via Space-Time Beamforming for Early Detection of Breast Cancer: Beamformer Design in the Frequency Domain". In: *Journal of Electromagnetic Waves and Applications* 17.2 (2003), pp. 357–381.
- [127] M. O'Halloran, M. Glavin, and E. Jones. "Performance and Robustness of a Multistatic Mist Beamforming Algorithm for Breast Cancer Detection". In: *Progress In Electromagnetics Research* 105 (2010), pp. 403–424.

- [128] J. Moll and V. Krozer. "Time-Difference-of-Arrival Imaging for Ultra-Wideband Microwave Mammography". In: *Antennas and Propagation (EuCAP), 2013 7th European Conference on*. 2013, pp. 2665–2669.
- [129] J. Li, P. Stoica, and Z. Wang. "On robust Capon beamforming and diagonal loading". In: *Signal Processing, IEEE Transactions on* 51.7 (2003), pp. 1702–1715.
- [130] Y. Xie, B. Guo, L. Xu, J. Li, and P. Stoica. "Multistatic Adaptive Microwave Imaging for Early Breast Cancer Detection". In: *Biomedical Engineering, IEEE Transactions on* 53.8 (2006), pp. 1647–1657.
- [131] D. Byrne, M. O'Halloran, E. Jones, and M. Glavin. "Transmitter-Grouping Robust Capon Beamforming for Breast Cancer Detection". In: *Progress In Electromagnetics Research* 108 (2010), pp. 401–416.
- [132] L. Xu, X. Xiao, L. Wang, and T. Kikkawa. "Ultra-Wide Band Microwave Image Reconstruction for Early Breast Cancer Detection by Double Constrained Robust Capon Beamforming". In: *Electron Devices and Solid-State Circuits (EDSSC), 2011 International Conference of*. 2011, pp. 1–2.
- [133] J. Moll, C. Bauer, and V. Krozer. "Microwave-Based Tumor Localization in Moderate Heterogeneous Breast Tissue". In: *Radar Symposium (IRS), 2013 14th International*. Vol. 2. 2013, pp. 877–884.
- [134] D. Byrne, M. O'Halloran, E. Jones, and M. Glavin. "The Effects of Breast Tissue Heterogeneity on Data-adaptive Beamforming". In: *PIERS Online* 6.8 (2010), pp. 740–745.
- [135] M. O'Halloran, M. Glavin, and E. Jones. "Rotating Antenna Microwave Imaging System for Breast Cancer Detection". In: *Progress In Electromagnetics Research* 107 (2010), pp. 203–217.
- [136] M. O'Halloran, M. Glavin, and E. Jones. "Effects of Fibroglandular Tissue Distribution on Data-Independent Beamforming Algorithms". In: *Progress In Electromagnetics Research* 97 (2009), pp. 141–158.
- [137] J. Moll, C. Kexel, and V. Krozer. "A Comparison of Beamforming Methods for Microwave Breast Cancer Detection in Homogeneous and Heterogeneous Tissue". In: *Microwave Conference (EuMC), 2013 European*. IEEE. 2013, pp. 1839–1842.
- [138] D. Byrne, M. O'Halloran, M. Glavin, and E. Jones. "Contrast Enhanced Beamforming for Breast Cancer Detection". In: *Progress In Electromagnetics Research B* 28 (2011), pp. 219–234.
- [139] E. W. Weisstein. *Bean Curve*. Available from <http://mathworld.wolfram.com/BeanCurve.html> [accessed on 06/03/2014]. From MathWorld — A Wolfram Web Resource.
- [140] J.-P. Berenger. "A Perfectly Matched Layer for the Absorption of Electromagnetic Waves". In: *Journal of Computational Physics* 114.2 (1994), pp. 185–200.

- [141] D. Winters, E. J. Bond, B. Van Veen, and S. Hagness. "Estimation of the Frequency-Dependent Average Dielectric Properties of Breast Tissue Using a Time-Domain Inverse Scattering Technique". In: *Antennas and Propagation, IEEE Transactions on* 54.11 (2006), pp. 3517–3528.



LN VISUALISER's Quick Guide

This appendix contains the quick guide for LN VISUALISER, a MATLAB Graphic User Interface designed to create an energy profile of the axilla according to the microwave backscattered signals recorded in the antennas. This interface also allows to calculate performance metrics in order to evaluate each image formation algorithm.

LYMPH NODES

VISUALISER

QUICK GUIDE

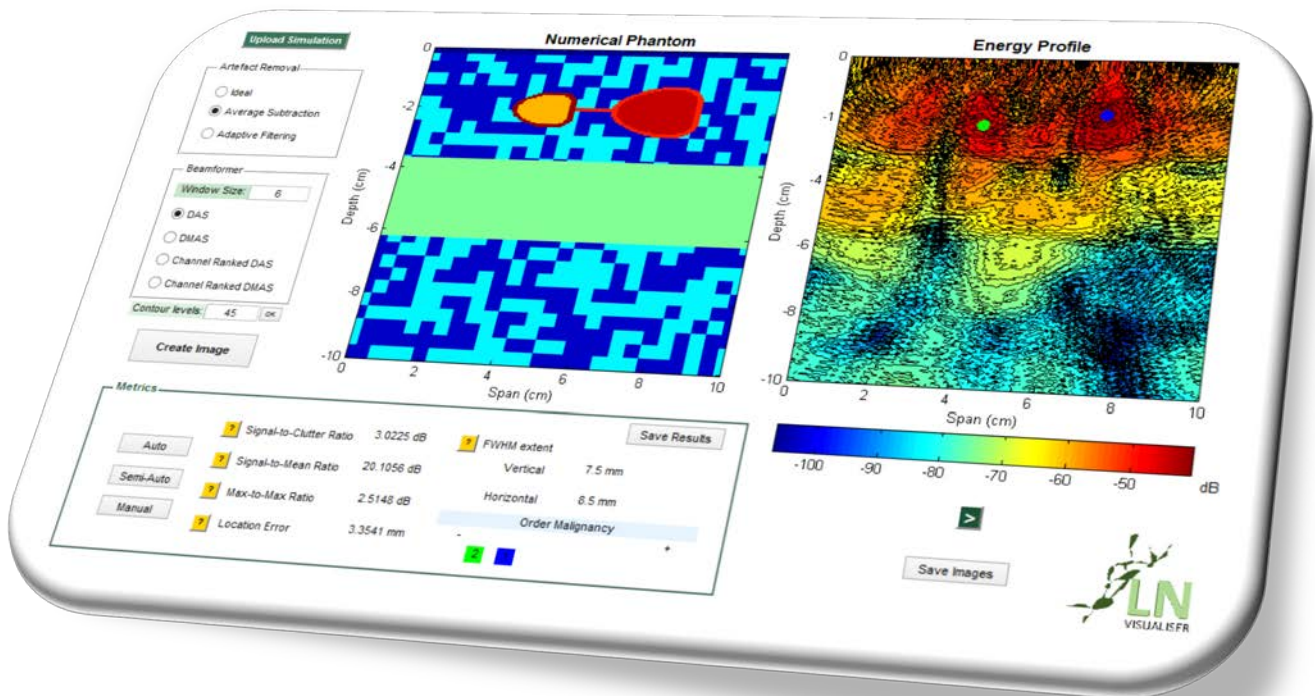
RICARDO JORGE NEVES ELEUTÉRIO



LYMPH NODES

VISUALISER

QUICK GUIDE



Developed by Ricardo Jorge Neves Eleutério under the framework of his Master Dissertation in Biomedical Engineering entitled: 'Microwave Imaging of the Axilla to Aid Breast Cancer Diagnoses'

In about 80% of detected breast cancer cases, cancer cells can metastasise to the axillary lymph nodes (LN), making their analysis an essential part of breast cancer staging. A potential non-invasive approach to early detection of metastasis in lymph nodes is **Microwave Imaging** in which healthy and diseased lymph nodes can be identified due to different dielectric properties. LN VISUALISER is a MATLAB graphic user interface designed to create an energy profile of the axilla according to the microwave signals recorded in the antennas. These images allow to check whether there are healthy or diseased lymph nodes since high energy regions in Microwave Images may indicate the presence of a tumour.

Prior to the use of LN VISUALISER, it is necessary to simulate the propagation of electromagnetic waves in the underarm (using, for instance, the FDTD method).

Numerical Phantom

In order to create an image of the axilla, first it is necessary to provide the **results** of a FDTD **simulation** performed with a numerical phantom that mimics the underarm region to the LN VISUALISER. For that, LN VISUALISER automatically searches for a '.mat' file named 'FDTDResults' in the current folder. However, if the file does not exist or the user wants to select another file, it is possible to click on [Upload Simulation](#) and choose the intended results file.

LN VISUALISER assumes that the file has information regarding the phantom that was used for the simulation and that the simulation has been completed for a numerical phantom with the following characteristics:

- 400 x 400 cells (although only 200x200 cells are displayed)
- 0.5 mm resolution

As soon as the simulation is uploaded, the numerical phantom is shown (**Fig. 1**).

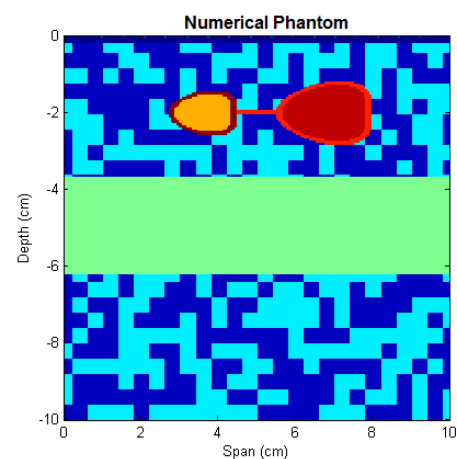


Fig. 1 | Numerical Phantom that is shown in LN VISUALISER as soon as the results of a simulation are uploaded.

Image Formation

In order to create an energy profile of the axilla, it is necessary to choose an algorithm for the **artefact removal** and another one for the **beamformer** (**Fig. 2**).

Artefact Removal

There are three options: Ideal, Average Subtraction and Adaptive Filtering.

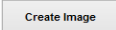
- Ideal

This algorithm removes the skin artefact from a signal by subtracting the signal without the lymph nodes. It is necessary to provide the results of a simulation with a **homogeneous numerical phantom without the lymph nodes** (or other tissue such as muscle) to the LN VISUALISER. For this, LN VISUALISER searches for a .mat file named 'FDTDResults_background_noTumour' in the current folder. If it does not exist, it asks the user to select the intended file.

- Average Subtraction¹

It removes the artefact from each monostatic channel by subtracting the **average** of the downsampled monostatic signals from all channels.

- Adaptive Filtering²

It estimates the artefact at each antenna as a filtered combination of the signals at all other antennas. If this option is selected and the user clicks on , he/she will be asked to fill the following information (**Fig. 3**):

- ✓ **Window Start and Window End** - need to be chosen to window the original signal so that it contains the artefact caused by the skin (to be removed) and no backscattered signals from tumours. *Default: 6 and 40, respectively.*
- ✓ **Number of Samples Each Side** - number of samples in each side of the n^{th} air-skin response. *Default: 3.*
- ✓ **Number of Eigenvalues** *Default: 5.*

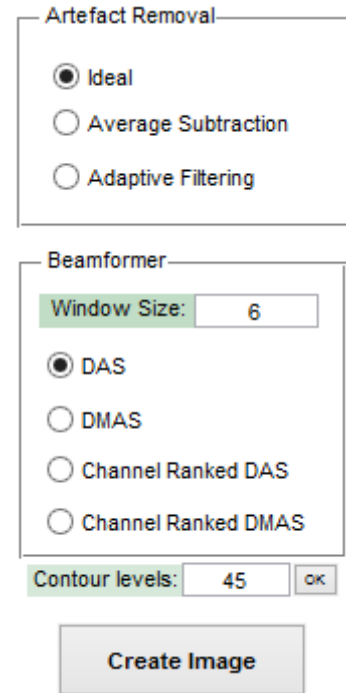


Fig. 2 | Algorithm that the user needs to choose to create an energy profile of the axilla.

¹ X. Li and S. Hagness. "A Confocal Microwave Imaging Algorithm for Breast Cancer Detection". In: Microwave and Wireless Components Letters, IEEE 11.3 (2001), pp. 130–132.

² E. J. Bond, X. Li, S. Hagness, and B. Van Veen. "Microwave Imaging Via Space-Time Beamforming for Early Detection of Breast Cancer". In: Antennas and Propagation, IEEE Transactions on 51.8 (2003), pp. 1690–1705.

Fig. 3 | Information asked to the user when they create an image using the 'Adaptive Filtering' artefact removal. This figure shows the default values.

Beamformer

There are four options: Delay and Sum (**DAS**), Delay Multiply and Sum (**DMAS**), **Channel Ranked DAS** and **Channel Ranked DMAS**. For any of these options it is necessary to firstly choose the **Window Size** for calculating energy (*Default: 6*).

- DAS³
It calculates time delays based on the distances from a focal point (each point in the grid) to the antenna, and then time-shifts the signals and adds them to calculate the energy of that focal point.
- DMAS⁴
It performs an additional pairing multiplication procedure after time shifting (as completed for the DAS).
- Channel Ranked DAS⁵
It gives extra weighting to signals with shorter propagation distances.
- Channel Ranked DMAS
It performs an additional pairing multiplication procedure to Channel Ranked DAS.

³ S. Hagness, A. Taflove, and J. Bridges. "Two-Dimensional FDTD Analysis of a Pulsed Microwave Confocal System for Breast Cancer Detection: Fixed-Focus and Antenna-Array Sensors". In: Biomedical Engineering, IEEE Transactions on 45.12 (1998), pp. 1470–1479.

⁴ H. B. Lim, N. T. T. Nhung, E.-P. Li, and N. D. Thang. "Confocal Microwave Imaging for Breast Cancer Detection: Delay-Multiply-and-Sum Image Reconstruction Algorithm". In: Biomedical Engineering, IEEE Transactions on 55.6 (2008), pp. 1697–1704.

⁵ M. O'Halloran, M. Glavin, and E. Jones. "Channel-Ranked Beamformer for the Early Detection of Breast Cancer". In: Progress In Electromagnetics Research 103 (2010), pp. 153–168.

Image Visualisation

After the algorithms are chosen, clicking on will create the ‘**Energy Profile**’ of the axilla. The image that appears in LN VISUALISER is created using the function *contourf* in MATLAB (**Fig. 4**) and using a decibel (dB) scale. The number of counter levels can be changed at any time by changing the field and clicking to apply to the current image or to create a new image with the new number of counter levels.

Sometimes it is useful to visualize the image using the function *imagesc* instead (**Fig. 5**). This can be done by pressing .

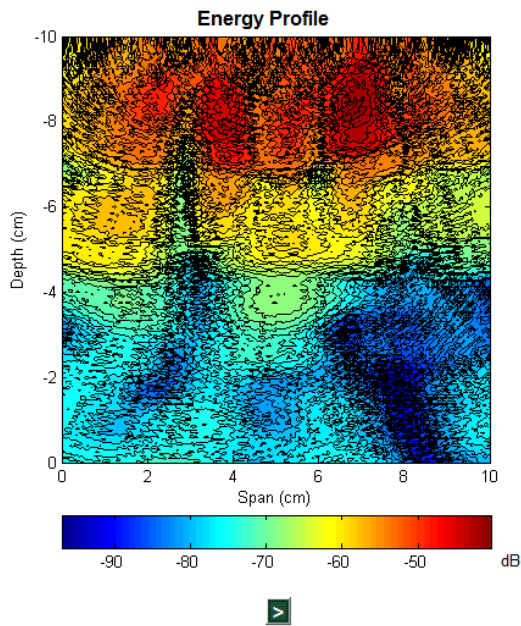


Fig. 4 | Energy profile of the axilla using the function *contourf*.

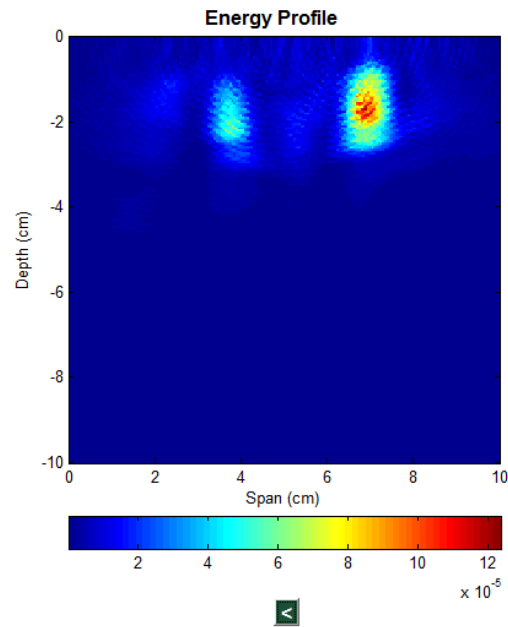


Fig. 5 | Energy profile of the axilla using the function *imagesc*.

Save Images

Pressing on will save the following images in the current folder:

- Current numerical phantom (file name: Phantom.png)
- Energy profile with *contour* (file name: Energy_X1_X2.png)
- Energy profile with *imagesc* (file name: Energy2_X1_X2.png)

In the file names, X1 and X2 refer to the algorithms used for the image formation (Artefact removal and Beamformer, respectively).

Calculate Metrics

The screenshot shows a window titled 'Metrics'. On the left, there are three buttons: 'Auto', 'Semi-Auto', and 'Manual'. To the right of these buttons are five metrics, each preceded by a yellow question mark icon: 'Signal-to-Clutter Ratio', 'Signal-to-Mean Ratio', 'Max-to-Max Ratio', 'Location Error', and 'FWHM extent'. The 'FWHM extent' metric has two sub-options, 'Vertical' and 'Horizontal', listed below it. At the bottom right, there is a 'Save Results' button. The 'Order Malignancy' label is visible at the bottom of the window.

Fig. 6 | The user can select one of three methods to calculate metrics and see the results of this calculation. It is also possible to save the results.

There are 3 options to calculate metrics, based on the energy profile created by certain algorithms (**Fig. 6**):

- **Auto:** Automatically calculates the metrics.
- **Semi-Auto:** It is necessary to introduce how many lymph nodes are present (based on the numerical phantom).
- **Manual:** Firstly, it is necessary to introduce the number of lymph nodes which are present, and then it is necessary to select the region of interest for each lymph node response in the 'Energy Profile'. This selection needs to be sufficiently large (at least twice the extent of the FWHM value, which is the point at which the energy of the peak response drops to half).

Note: Pressing  will explain what is being calculated in each metric.

After one of these methods has been chosen and the metrics calculated, the user will visualise the several lymph nodes that were found in the 'Energy Profile' (LN VISUALIZER is able to show up to seven lymph nodes) under **Order Malignancy**. They will appear in **different colours** (that are also represented in the 'Energy Profile') and in **increasing order** of probability of being a diseased lymph node (**Fig. 7**). Also, they are given a number, where 1 represents the lymph node with higher probability of being metastasised, 2 the second lymph node with higher probability of being metastasised, etc. This order is based on the fact that higher energy regions may correspond to tumours and that the higher the energy, the higher the probability of the region being a tumour.

Note: It is good practice to **always check**, by looking at the 'Energy Profile' with the different colours, if the lymph nodes that were detected automatically by 'Auto' or 'Semi-Auto' make sense. Since these are automatic methods, they might not work correctly depending on the image.

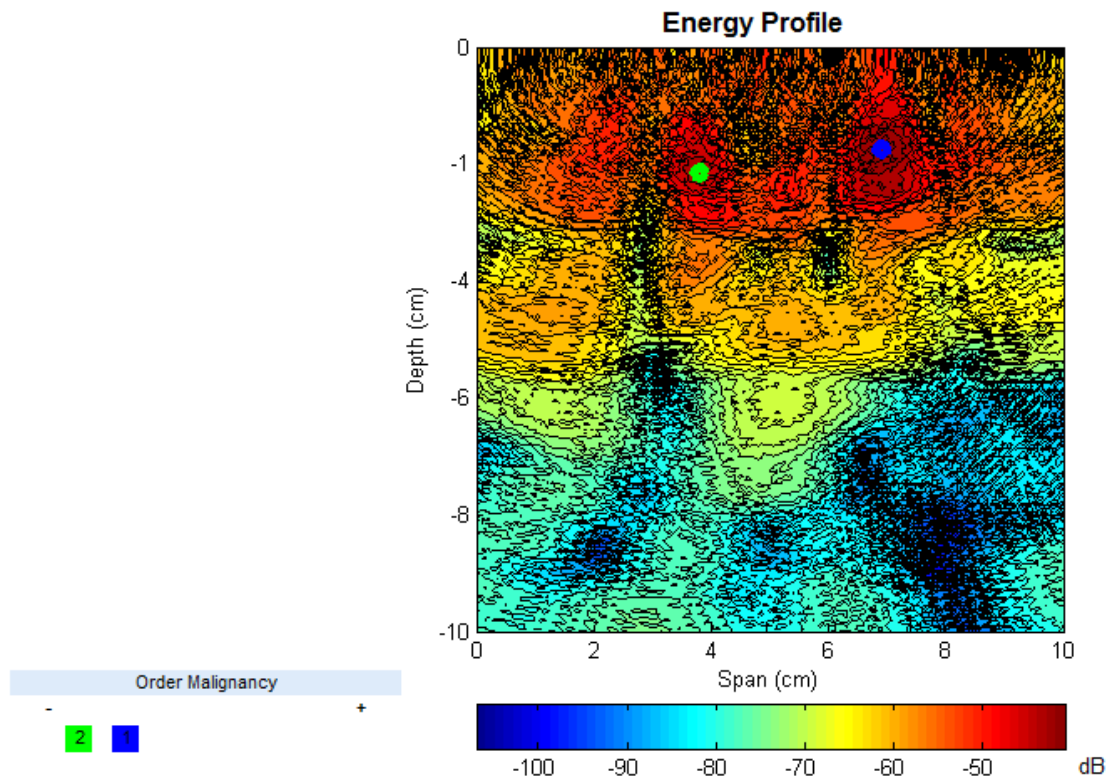


Fig. 7 | After calculating metrics, LN VISUALIZER indicates the LNs that were found in the 'Energy Profile' and orders them by likelihood of malignancy.

Save Results

Clicking on **Save Results** will save a '.txt' file with the metrics calculation under the name 'Results_Metrics' in the current folder. If the file already exists it is possible to overwrite the file or to add an extra line to the already existing file (**Fig. 8**). It is particularly useful to add results if we are comparing different algorithms for the same numerical phantom. In this file, each line has a reference to the algorithms that were used to form the 'Energy Profile' (**Fig. 9**).

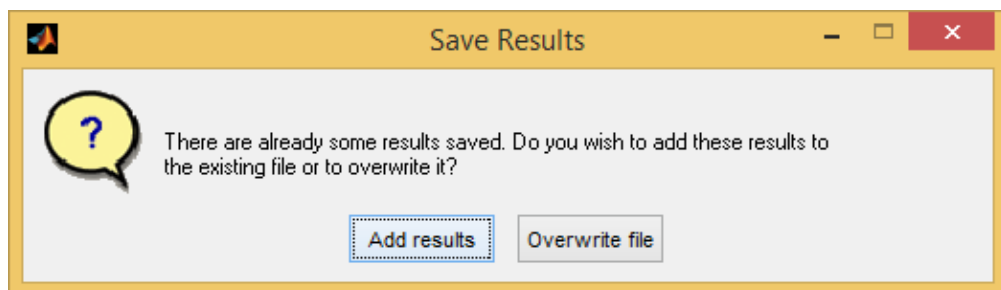


Fig. 8 | Dialog box that appears to the user when he/she clicks on **Save Results** and there is already a file named 'Results_Metrics.txt' in the current folder.

	SCR (dB)	SMR (dB)	MMR (dB)	LocError (mm)	FWHM vert (mm)	FWHM hor (mm)
Ideal + DAS	3.01213	17.83276	2.32375	3.35410	15.5	8.5
Average + DAS	3.01823	19.24076	2.63904	3.35410	12.5	8.5
Ideal + DMAS	3.01746	22.94978	4.30431	3.35410	4.0	4.0
Average + DMAS	3.01536	24.95793	4.22939	3.35410	4.0	4.0
Ideal + ChannelRankedDAS	1.71498	17.81843	2.68200	3.35410	14.5	10.5
Average + ChannelRankedDAS	2.51331	18.41055	3.41594	3.35410	15.0	9.5

Fig. 9 | Example of a file with results using the same phantom but comparing several image formation algorithms.



Poster

This appendix contains the poster presented in the 6th Workshop on Biomedical Engineering, held in Lisbon on the 5th April 2014. Here, some initial results obtained in this dissertation were shown.

Abstract

- Microwave Imaging (MWI) is one of the most promising imaging modalities for breast cancer early screening and monitoring. We propose a new imaging modality to improve breast cancer diagnosis and the detection of metastasised lymph nodes in the underarm region.
- In this initial study we test the feasibility of microwave imaging in the axillary region by means of the simulation of an Ultra Wideband radar system. The image formation algorithm is tested to assess if two close lymph nodes are distinguishable and if it is possible to detect a metastasised lymph node.

Introduction

Motivation

- In 80% of breast cancer cases, **cancer cells metastasise into axillary lymph nodes** (Figure 1).
- If tumour cells are detected in lymph nodes, metastases may have spread to other organs.
- Analysis of the lymph nodes enables **cancer staging**.

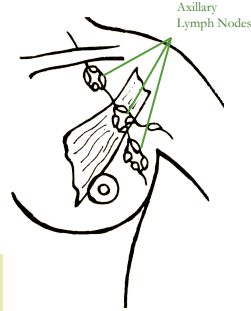


Figure 1. Representation of the location of axillary lymph nodes.

Ultra Wideband (UWB) Microwave Radar Imaging

- Promising **non-invasive** approach to diagnose lymph nodes.
- Advantages:
 - low power;
 - non-ionizing;
 - low-cost.
- Healthy and diseased lymph nodes are identified by their **different dielectric properties** (relative permittivity and conductivity) at microwave frequencies.
- MWI involves illuminating the axilla with a UWB pulse, and recording the resulting backscattered signals (Figure 2).

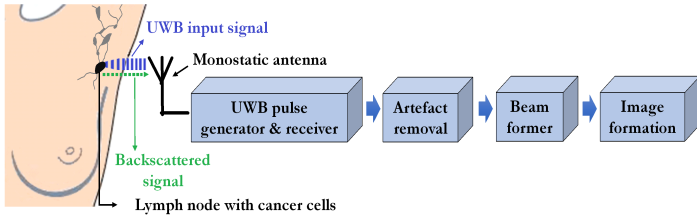


Figure 2. Diagram illustrating a monostatic microwave UWB radar imaging system.

- The processing of the backscattered signals include:
 - **Artefact removal** to remove the high skin reflection.
 - **Beamformer** to spatially focus the backscattered signals.
 - **Image formation** to image dielectric scatterers.

Methods and Materials

Finite-Difference Time-Domain (FDTD) Simulations

- The **FDTD** was used to simulate the propagation of microwaves in the axilla.

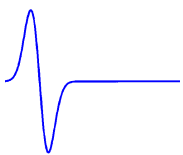


Figure 3. Differentiated Gaussian pulse.

- The input pulse (Figure 3) was a 150 ps differentiated Gaussian with a centre frequency of 7.5 GHz and a -3dB bandwidth of 9 GHz:

$$G(t) = c \times (t - d) \times e^{-\frac{(t-d)^2}{\tau^2}}$$

$$\begin{aligned} -c &= -0.25 \\ -\tau &= 35 \\ -d &= 3 \times \tau \end{aligned}$$

- The frequency-dependency of the dielectric properties is implemented with FDTD by the following **Debye formulation** (simulation parameters in Table 1):

$$\epsilon^*(\omega) = \epsilon_{\infty} + \frac{\sigma_s}{j\omega\epsilon_0} + \frac{\epsilon_s - \epsilon_{\infty}}{1 + j\omega\tau}$$

$$\begin{aligned} -\sigma_s &\text{ static conductivity} & -\epsilon_{\infty} &\text{ permittivity at } \omega = \infty \\ -\epsilon_0 &\text{ permittivity of free space} & -\tau &\text{ relaxation time constant} \\ -\epsilon_s &\text{ static permittivity} & -\omega &\text{ angular frequency} \end{aligned}$$

Acknowledgements:

This work is supported by Marie Curie Intra European Fellowship within the 7th European Community Framework Programme under REA grant agreement number 301269, by Fundação para a Ciência e Tecnologia under the strategic plan of the Instituto de Biofísica e Engenharia Biomédica PEst-OE/SAU/UI0645/2011. This work was developed under the framework of COST Action TD1301 (MiMed).

Table 1. Parameters of the Debye Formulation for the underarm region as defined by Cameron et al. and Lazebnik et al.

	Permittivity (ϵ_{∞}) [F/m]	Conductivity (σ_s) [S/m]	$\epsilon_s - \epsilon_{\infty}$ [F/m]	Relaxation Time (τ) [ps]
Skin	15,93	0,831	23,83	13
Heterogeneous Adipose Tissue ($\pm 10\%$)	3,14	0,036	23,83	14,11
Healthy Lymph Node	47	6	27	9,4
Metastasised Lymph Node	55	9	31	11,1

Signal Processing Algorithms

- **Artefact Removal** – Subtract the average of all the stored waveforms from each of the original backscattered signals to remove the skin response.
- **Beamformer and Image Formation** – Delay-And-Sum algorithm (Figure 4).

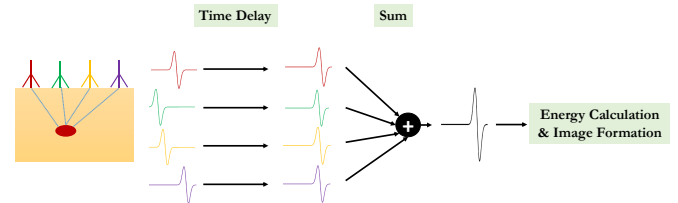


Figure 4. Diagram illustrating the Delay-And-Sum beamformer.

Results

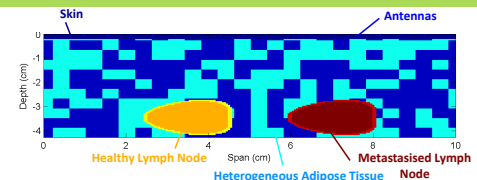


Figure 5. Numerical phantom of the axilla.

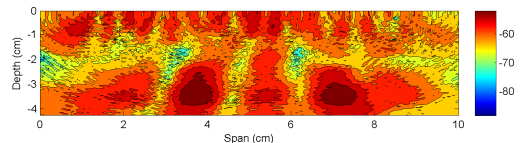


Figure 6. Energy profile of the axilla (on a dB scale). The lymph nodes location is given by the dark red region.

Discussion

- It is possible to distinguish two lymph nodes separated by 30 mm (between its centres) with an error of 1.0 mm and to detect their depth with an error of 0.5 mm.
- In these preliminary results, the algorithms used to create the energy profile could not correctly differentiate between a healthy and a metastasised lymph node.

Conclusions

- This innovative work proposes a microwave-based system for axillary lymph node examination so that metastasised lymph nodes can be detected ahead of surgery to:
 - predict breast cancer staging;
 - avoid removing healthy lymph nodes and its resulting health risks (e.g., lymphedema and paraesthesia).
- In future work, we aim to improve the algorithms to distinguish between healthy and metastasised lymph nodes and to test these algorithms in more realistic phantoms.

References

- 14, X.; Hagness, S.C., "A confocal microwave imaging algorithm for breast cancer detection," *Microwave and Wireless Components Letters, IEEE*, vol.11, no.3, 130-132, March 2001
- Cameron, T. R.; Okoniewski, M.; Fear, E.C., "A Preliminary Study of the Electrical Properties of Healthy and Diseased Lymph Nodes," in 14th International Symposium on Antenna Technology and Applied Electromagnetics (ANTEM) and the American Electromagnetics Conference (AMEREM), Ottawa, Canada, 1-3, 2010
- Lazebnik, M.; Okoniewski, M.; Booske, J. H.; Hagness, S.C., "Highly Accurate Debye Models for Normal and Malignant Breast Tissue Dielectric Properties at Microwave Frequencies", *IEEE Microwave and Wireless Components Letters*, vol. 17, no. 12, 2007



Abstract

This appendix contains the abstract submitted and accepted for an oral presentation at a special session in the 2014 IEEE International Symposium on Antennas and Propagation and USNC-URSI Radio Science Meeting, held from the 6th to 12th July 2014, in Memphis, Tennessee, USA.

Initial Study with Microwave Imaging of the Axilla to Aid Breast Cancer Diagnosis

Ricardo Eleutério^(1,2), Alexandre Medina^(1,2), and Raquel C. Conceição*⁽¹⁾

(1) Universidade de Lisboa, Faculdade de Ciências, Instituto de Biofísica e Engenharia Biomédica, Campo Grande, 1749-016 Lisboa Portugal

(2) Universidade Nova de Lisboa, Faculdade de Ciências e Tecnologia, Departamento de Física, Quinta da Torre, 2829-516 Caparica, Portugal

Microwave Imaging (MWI) is one of the most promising imaging modalities for breast cancer early screening and monitoring. An important issue that is not commonly addressed in breast microwave imaging literature is the importance of imaging the underarm region – where up to 80% of breast cancer cells can metastasise to [Cameron et al, ANTEM, 1-3, 2010; Patani, Journal of Cancer Surgery, 33, 409-419, 2007]. When performing mastectomies to remove breast cancer, the axillary lymph nodes are often removed and their histopathological analysis is performed. Thus, the evaluation of whether the cancer has spread beyond the breast is crucial to decide what follow-up exams and therapy to follow. The first nodes to receive drainage from the primary tumour in the breast are called Sentinel Node. If cancer cells are found in the Sentinel Node, there is an increased risk of metastatic breast cancer and an axillary dissection should be performed. However, the non-invasive detection of cancer cells in the Sentinel Node is often inconclusive. Because of that, often too many lymph nodes are surgically removed in a time-consuming process which is associated with a long patients' recovery, pain, risk of infection and lymphedema [Komen, Facts for Life: Axillary Lymph Node, 2009]. Therefore, non-invasive alternatives for the use in axillary staging should be considered in order to reduce the incidence of these adverse events.

We propose an initial study to test the feasibility of imaging the axilla region by means of the simulation of an Ultra Wideband radar system. We will present initial 2D axilla models consisting of skin, normal tissue and metastasised lymph nodes. Initial imaging results will be obtained by means of a beamformer that will ultimately time-align all the signals recorded at each antenna. The location of the metastasised lymph node will be analysed by visual inspections and through metrics, such as Signal-to-Clutter Ratio and/or Full Width Half Maximum metrics.